

DISSERTATION

# Interleaved Localised $^1\text{H}/^{31}\text{P}$ Nuclear Magnetic Resonance Spectroscopy of Skeletal Muscle

ausgeführt am Zentrum für Biomedizinische Technik und Physik, Institut für Medizinische Physik der Medizinischen Universität Wien zum Zwecke der Erlangung des akademischen Grades eines Doktors der technischen Wissenschaften unter der Leitung von

Ao. Prof. Dipl.-Ing. Dr. Ewald Moser

Zentrum für Biomedizinische Technik und Physik  
Medizinische Universität Wien

in Zusammenarbeit mit

Prof. Dipl.-Ing. Dr. Gerald Badurek  
Atominstitut der Österreichischen Universitäten

eingereicht an der Technischen Universität Wien  
Fakultät für Physik

von

Dipl.-Ing. Martin Meyerspeer

9325116

Matrikelnummer

A-1180 Wien, Edelhoftgasse 36 / 21

Wien, am 13. September 2005

# Kurzfassung

Die Kernspin-Magnetresonanz (Nuclear Magnetic Resonance, NMR) wird seit ihrer Entdeckung vielfältig, zunächst als spektroskopische Methode in Physik und Chemie und später vorwiegend als bildgebendes Verfahren in der Medizinischen Diagnostik genutzt. Als spektroskopisches Verfahren *in vivo* am Menschen angewandt, bietet die NMR-Spektroskopie die Möglichkeit, Stoffwechselfvorgänge in physiologischen und pathologischen Fragestellungen anhand der Metabolitenkonzentrationen und ihrer Änderungsraten nichtinvasiv, lokalisiert und zeitaufgelöst zu verfolgen, wobei abhängig vom angeregten Kern verschiedene „Beobachtungsfenster“ also das Ensemble messbarer Größen, genutzt werden können.

Mechanismen der Resynthese von Adenosintriphosphat (ATP) als direktem Energieträger für Muskelkontraktionen sind u.a. Spaltung von Kreatinphosphat (PCr), Glykolyse,  $\beta$ -Oxidation und schließlich oxidative Phosphorylierung. Während der Beitrag dieser Stoffwechselprozesse zur Deckung des Energiebedarfs der Muskulatur in bekannter Weise abhängig ist von Art und Dauer der Beanspruchung, ist die Funktionsweise ihrer Regulationsmechanismen noch Gegenstand aktueller Forschung. Ein großer Anteil des Wissens über den Metabolismus des Muskels basiert auf biochemischen Analysen von invasiv gewonnenem Gewebe (Biopsien, Mikroperfusion) oder der Bestimmung von Parametern die lediglich eine Aussage über den Stoffwechsel des Gesamtorgansmus zulassen (Blut- oder Atemgasanalyse). Mittels lokalisierter NMR-Spektroskopie können hingegen zeitaufgelöste Daten aus einem definierten Volumen *in vivo*, nichtinvasiv akquiriert werden.

Im Gegensatz zur überwiegenden Mehrheit der publizierten Studien, in denen NMR-Spektroskopie mit der Anregung nur eines Nuklids (meist  $^1\text{H}$ ,  $^{31}\text{P}$  oder  $^{13}\text{C}$ ) oder mehrere solche Experimente hintereinander durchgeführt wurden, öffnet diese Arbeit ein weiteres Fenster zur Beobachtung des Metabolismus, indem multinukleare NMR-Spektroskopie in ein einziges Experiment verschachtelt („interleaved“) während Ruhe, Belastung und Erholungsphase der Wadenmuskulatur *in vivo* durchgeführt wurde. Mit dieser Methodik sind unter anderem die Konzentrationen von Kreatinphosphat, anorganischem Phosphat, ATP, totalem Kreatin und erstmals auch Laktat im menschlichen Gastrocnemius-Muskel direkt, das heißt ohne die Anwendung physiologischer Modellannahmen einer nichtinvasiven lokalisierten zeitaufgelösten Messung zugänglich und der intrazelluläre pH-Wert kann ebenfalls anhand von  $^{31}\text{P}$ -Spektren bestimmt werden. Die Quantifikation von Laktat mittels NMR-Spektroskopie stellt dabei eine besondere Herausforderung dar, da das Laktatsignal im Muskel erstens von vielfach stärkeren Signalen des intramuskulären Fetts überlagert ist und zweitens orientierungsabhängige Modulationen aufweist, deren Verhalten von Parametern wie Muskelfaserorientierung, intra- und extrazellulärer Volumensanteil und Relaxationszeiten abhängt, die nur schwer einer Messung zugänglich sind.

Die Arbeit gliedert sich in eine Einführung zur Muskelphysiologie und der zum Studium des Metabolismus angewandten Methoden, gefolgt von einem Kapitel zur theoretischen Beschreibung der lokalisierten NMR-Spektroskopie mittels STEAM und der zur Laktat-Quantifizierung im Muskel entwickelten Doppelquantenfilter-Pulssequenz (ergänzt durch eine Zusammenfassung des Produktoperator-Formalismus zur Beschreibung des Doppelquantenexperiments für die Laktat-Quantifizierung im Anhang).

Der zweite Teil ist den am 3 Tesla Ganzkörper NMR-Scanner des „Exzellenzzentrums Hochfeld-Magnetresonanz“ an der Medizinischen Universität Wien durchgeführten Experimenten gewidmet. Er beginnt mit der Beschreibung des im Zuge des Projekts konstruierten Geräts zur Aktivierung der Wadenmuskulatur während der Messung im NMR-Gerät und einem Kapitel mit Beispielen einfacher Muskel-NMR-Spektroskopie. Weiters ist die aus der Verschachtelung zweier STEAM-Sequenzen, (eines  $^1\text{H}$ - und eines  $^{31}\text{P}$ -Experiments) bestehende multinukleare Spektroskopie-Methode beschrieben. Ein weiteres Kapitel behandelt die lokalisierte Doppelquantenfilter-Sequenz, welche zur Unterdrückung starker, die Laktat- $\text{CH}_3$ -Resonanz überlagernder Lipidsignale der Muskel-Spektren entwickelt wurde. Dabei waren erst im letzten Jahr in Publikationen beschriebene Ordnungseffekte im Muskelgewebe zu berücksichtigen, ohne deren Kenntnis eine Quantifizierung von Laktat in dieser Weise unmöglich ist. Schließlich wird das Experiment beschrieben, in dem Doppelquanten-gefilterte Laktat-Spektren,  $^1\text{H}$ - und  $^{31}\text{P}$ -STEAM Spektren in einer einzigen Messung zeitaufgelöst aufgenommen wurden, während die Versuchsperson im Magneten durch ischämische Plantarflexion und mit Hilfe der beschriebenen Konstruktion die Wadenmuskulatur aktiviert.

Der abschließende Teil besteht aus den Schlussfolgerungen, dass die mit  $^{31}\text{P}$ -NMR-Spektroskopie in vivo akquirierten Daten und gleichzeitig bestimmte Laktatkonzentration der Klärung aktueller Diskussionen über intrazelluläre  $\text{H}^+$ -Pufferkapazität dient und die Methodik geeignet ist, aus Laktatkonzentration, pH und PCr während Erholung nach ischaemischer Belastung metabolischen Fluss zu bestimmen und während aerober und anaerober Belastung angewandt werden kann, um die Kontrollmechanismen von Glykogenolyse und Koordination oxidativer und glykolytischer ATP-Produktion zu studieren. Mögliche Weiterentwicklungen der Methodik sind weitere Verbesserung der Spezifität, etwa durch multinukleare Spektroskopische Bildgebung und Steigerung der Sensitivität und damit verbunden der Zeitauflösung, durch den Einsatz noch höherer Feldstärken.

# Abstract

Nuclear magnetic resonance (NMR) has been used as a spectroscopic method in physics and chemistry before it was developed to become a diagnostic imaging tool in medicine. When NMR Spectroscopy is applied to human tissue, metabolism can be studied in normal physiological and pathological states *in vivo*. Metabolite concentrations and rates can be monitored dynamically and with localisation of a defined region of interest. The “window” which is opened for observation, i.e. which quantities are measured, depends on the nucleus used for RF excitation.

Mechanisms of adenosine tri-phosphate (ATP) resynthesis, as a direct source of energy for muscle contraction, are phosphocreatine (PCr) splitting, glycolysis,  $\beta$ -oxidation and, finally, oxidative phosphorylation. Whilst the dependency of these processes’ fractional contribution to muscular energy supply on exercise type and duration is well known, quantitative models of the regulating mechanisms involved are still subject of current research. A large fraction of the established knowledge about metabolism is based on biochemical analysis of tissue acquired invasively (e.g. microdialysis and open-flow microperfusion) or representing averaged metabolic concentrations for the whole body (via serum metabolites or gas exchange analysis). Localised NMR spectroscopy, however, is capable of non-invasively acquiring time-resolved data from a defined volume of interest, *in vivo*.

In contrast to the vast majority of MRS studies investigating metabolism, where spectra of a single nucleus (commonly  $^1\text{H}$ ,  $^{31}\text{P}$  or  $^{13}\text{C}$ ) were acquired or several MR spectra with different nuclei were measured in separate experiments, this work opens an additional “window” on muscle metabolism by interleaved localised acquisition of  $^1\text{H}$  and  $^{31}\text{P}$  NMR spectra from human calf muscle *in vivo*, during rest, exercise and recovery, in a single experiment. Using this technique, the time courses of the concentrations of phosphocreatine, inorganic phosphate ( $\text{P}_i$ ), ATP, total creatine, and lactate in human gastrocnemius muscle can be quantified directly, without using physiological model assumptions, while intracellular pH can be derived from the chemical shifts of  $\text{P}_i$  and PCr in  $^{31}\text{P}$  MR spectra. Quantifying intramuscular lactate by NMR spectroscopy is a challenging task, because the lactate signal is overlapped by strong lipid resonances and exhibits modulations which dependent on factors hard to control or measure, like muscle fibre orientation relative to the magnetic field, intra- and extracellular compartmentation and relaxation times.

The thesis is organised into an introduction to muscle physiology and methods for studying metabolism, followed by a theoretical chapter on localised NMR spectroscopy using STEAM and the localised double quantum filter (DQF) pulse sequence which was implemented for in vivo lactate detection. The theoretical sections are supplemented by an outline of the product operator formalism to describe the NMR spectroscopy experiments mathematically, in the appendix.

The second part describes the experiments which have been conducted at the 3 Tesla whole body NMR scanner installed at the “High Field MR Centre of Excellence”, Vienna Medical University: The non-magnetic exercise rig constructed for activation of human calf muscle during NMR measurements is presented. Examples of basic muscle MR spectroscopy are given and the interleaved  $^1\text{H}$  and  $^{31}\text{P}$  STEAM sequence implemented on the NMR scanner is explained in detail along with its application during calf muscle exercise, employing the exercise rig. Then the localised double quantum filter (DQF) pulse sequence is introduced which was developed for detection of the lactate  $\text{CH}_3$  resonance and suppression of overlaying lipid signals. Lactate quantification is only possible with this method due to the incorporation of knowledge about ordering effects published by other groups in the previous year. The final chapter of the experimental part comprises the time resolved interleaved localised DQF,  $^1\text{H}$  and  $^{31}\text{P}$  STEAM measurements during ischaemic calf muscle exercise using the exercise rig.

In conclusion,  $^{31}\text{P}$  MRS data and lactate concentrations measured simultaneously by  $^1\text{H}$  MRS help to confirm model assumptions about cellular proton buffering capacity. Questions on metabolic efflux can be addressed when studying lactate, pH and PCr changes during recovery from ischaemic exercise with high time resolution, as well as control of glycogenolysis and coordination of oxidative versus glycolytic ATP production in aerobic and ischaemic exercise. Perspectives are further improvement of specificity by multi nuclear spectroscopic imaging and an increase of sensitivity and time resolution by transferring the technique to an even higher field strength.

# Contents

<b>I. Rationale and Theoretical Background</b>	<b>1</b>
<b>1. Introduction</b>	<b>2</b>
1.1. Energy Sources of Muscle Contraction . . . . .	2
1.1.1. Muscle Anatomy . . . . .	4
1.2. Techniques to Study Muscle Biochemistry . . . . .	4
1.2.1. Muscle Metabolism as Viewed by $^{31}\text{P}$ MRS . . . . .	5
1.2.2. Muscle Metabolism as Viewed by $^1\text{H}$ MRS . . . . .	7
1.2.3. Current Limitations and Potential Improvements . . . . .	7
<b>2. Theory of MRS</b>	<b>9</b>
2.1. Introduction . . . . .	9
2.2. Localised NMR Spectroscopy, STEAM . . . . .	9
2.3. Product Operator Formalism and DQF Spectroscopy . . . . .	12
2.3.1. Principle of a Double Quantum Filter . . . . .	12
2.3.2. Lipid Pre-Inversion . . . . .	13
2.3.3. Orientation Dependence and Residual Dipolar Coupling of Lactate in Skeletal Muscle . . . . .	13
<b>II. Experimental</b>	<b>20</b>
<b>3. Construction of the Exercise Rig</b>	<b>21</b>
3.1. Introduction . . . . .	21
3.2. Mechanics . . . . .	21
3.3. Sensors . . . . .	23
3.3.1. Sensor Hardware . . . . .	23
3.3.2. Calibration Data . . . . .	26
3.4. Testing the Exercise Rig in Vivo . . . . .	27
<b>4. Basic <math>^1\text{H}</math> and <math>^{31}\text{P}</math> MRS in Resting Human Calf Muscle</b>	<b>30</b>
4.1. Introduction . . . . .	30
4.1.1. Non-localised Spectroscopy . . . . .	30
4.1.2. Localised (STEAM) Spectroscopy . . . . .	31
4.2. Longitudinal Relaxation and Repetition Time . . . . .	33
4.2.1. Why (Not) To Use Short Repetition Times . . . . .	33
4.2.2. A Short Repetition Time Experiment . . . . .	34

## Contents

4.2.3. Discussion . . . . .	34
<b>5. Dual Interleaved <math>^1\text{H}/^{31}\text{P}</math> STEAM MRS</b>	<b>36</b>
5.1. Introduction . . . . .	36
5.2. Methods . . . . .	37
5.2.1. Sequence Design . . . . .	37
5.2.2. Scanner Hardware . . . . .	39
5.2.3. Subjects . . . . .	40
5.3. Results . . . . .	40
5.3.1. Test Objects . . . . .	40
5.3.2. Resting Muscle . . . . .	40
5.3.3. Exercising Muscle . . . . .	41
5.4. Discussion . . . . .	41
5.5. Conclusion . . . . .	46
<b>6. Double Quantum Filter Sequence for Lactate Detection</b>	<b>47</b>
6.1. Introduction . . . . .	47
6.2. Sequence Design . . . . .	48
6.2.1. The RF Pulses . . . . .	48
6.3. Phantom Studies . . . . .	50
6.3.1. The Effect of $\tau'$ Without a Refocussing Pulse . . . . .	50
6.3.2. Calibration for Quantification of Absolute Concentration . . . . .	50
6.3.3. Test Object Containing Brain Metabolites (“Brain Soup”) . . . . .	53
6.3.4. Test Object Containing Lipid and Lactate . . . . .	53
6.4. Measurements on Meat Specimens . . . . .	54
6.4.1. Variation of Echo Time . . . . .	54
6.4.2. Variation of Angle Between Fibre Orientation and $B_0$ Field . . . . .	55
6.4.3. Conclusion . . . . .	57
<b>7. Triple Interleaved <math>^1\text{H}</math> DQF/<math>^{31}\text{P}/^1\text{H}</math> MRS</b>	<b>59</b>
7.1. Introduction . . . . .	59
7.2. Methods . . . . .	60
7.2.1. Sequence Design . . . . .	60
7.2.2. Subjects and Materials . . . . .	62
7.3. Results . . . . .	63
7.4. Discussion . . . . .	65
<b>III. Conclusion and Perspective</b>	<b>67</b>
<b>8. Conclusion</b>	<b>68</b>
<b>9. Perspective</b>	<b>70</b>

<b>IV. Appendices</b>	<b>73</b>
<b>A. Cirquits, Diagrams and Detail Drawings</b>	<b>74</b>
A.1. Circuit Diagram of the Operation Amplifier IC for Force Sensors . . . .	74
A.2. Block Diagram of the Dual Tuned Surface Coil . . . . .	76
A.3. Ergometer, Engineering Detail Drawing . . . . .	77
<b>B. Mathematical Appendix</b>	<b>78</b>
B.1. Product Operator Formalism . . . . .	78
B.1.1. Nomenclature . . . . .	78
B.1.2. Evolution of Product Operators . . . . .	79
B.1.3. Effect of a $90^\circ$ - $180^\circ$ - $90^\circ$ Pulse Train on an $IS$ Spin System . .	80
B.2. $J$ Evolution of an $IS_3$ System . . . . .	80
<b>Bibliography</b>	<b>82</b>
<b>Nomenclature</b>	<b>92</b>
<b>List of Figures</b>	<b>93</b>
<b>List of Tables</b>	<b>95</b>
<b>Danksagung</b>	<b>96</b>
<b>Curriculum Vitae</b>	<b>97</b>

**Part I.**

**Rationale and Theoretical  
Background**

# 1

## Introduction

An overview about the rationale and biochemical questions related to this PhD thesis and the underlying research project. What was measured, observed and why is this relevant?

### 1.1. Energy Sources of Muscle Contraction

The metabolism of contracting muscle is described in textbooks on physiology (e.g. “Taschenatlas der Physiologie” by S. Silbernagl et al. [1] or “Review of Medical Physiology” by W. F. Ganong [2]).

Adenosine tri-phosphate (ATP) is the direct source of energy for muscle contractions. But as the ATP pool in muscle cells is restricted, it would be depleted after e.g. 10 – 20 metres of running, if it was not continuously resynthesised, resulting in a largely constant intracellular ATP concentration even during increased ATP use.

ATP can be regenerated by:

- phosphocreatine (PCr) splitting
- anaerobic glycolysis
- aerobic oxidation of glucose and fatty acids.

As the latter two processes need some start-up time, the chemical energy of PCr is used to meet a temporary ATP shortfall immediately after the onset of exercise: Adenosine di-phosphate (ADP) which is produced during ATP splitting is transformed to ATP and Creatine (Cr) by cytosolic creatine kinase (CK). This process allows high-power exercise of short duration, i.e. 10 – 20 s, until the PCr pool (ca. 25  $\mu\text{mol/g}$  muscle) is depleted.

## 1. Introduction

Anaerobic glycolysis follows PCr splitting and reaches its peak after ca. 0.5 min. Glycogen stored in the muscle is metabolised to lactic acid via glucose-6-phosphate (G6P) which yields 3 ATP per glucose rest. During moderate exercise, the lactate generated in this reaction is further broken down in the heart and liver under consumption of  $H^+$ . After approximately 1 min, the much more efficient aerobic decomposition of glucose and fatty acids supersedes glycolytic ATP production. If this is yet insufficient under strenuous exercise, glycolysis continues, now decomposing mainly glucose delivered via the blood (from glycogenolysis and glyconeogenesis in the liver), with a net yield of only 2 ATP/glucose, as blood glucose has to be phosphorylated to G6P using 1 ATP.

Long-term exercise requires aerobic ATP resynthesis from glucose (which yields 2 + 34 ATP/glucose) and lipids. Pulse- and respiratory frequency are increased until the requirements of muscle metabolism are met, finally arriving at an equilibrium. Reaching this steady state takes several minutes during which anaerobic ATP synthesis, increased  $O_2$  uptake from blood and an activation of intramuscular  $O_2$  storage (myoglobin) bridge the gap until oxidative ATP production sets in.

When exercise intensity is further increased and the steady state becomes unsustainable – at approximately 370 W for athletes, dependent on the rate of maximal  $O_2$  uptake ( $VO_{2\max}$ ) and aerobic glucose and lipid decomposition – the energy gap can be matched temporarily by anaerobic ATP regeneration. But as  $H^+$  consumption during lactate decomposition cannot keep pace with a high rate of glycolytic lactate production,  $H^+$  accumulate. At 60 – 65% of  $VO_{2\max}$ , plasma concentration of lactate increases rapidly and reaches the “anaerobic threshold” at 4 mmol/l above which power output cannot be increased. Finally, the concomitant pH drop (acidosis) inhibits the chemical reactions necessary for muscle contraction, causes a shortfall in ATP and results in rapid fatigue and, ultimately, failure to continue exercise.

For a short period (ca. 40 s), a threefold power output compared to aerobic exercise can be achieved with PCr splitting and glycolysis. This high level exercise is associated with an  $O_2$  deficiency which has to be overcome during a subsequent recovery period mainly serving the regeneration of storages and decomposition of lactate in the liver and heart.

**Motivation of this work:** While the various mechanisms of ATP resynthesis (i.e. PCr splitting, glycolysis, oxidative phosphorylation) and the respective regimes they act in (short- or long term, high- or low power exercise) appear to be well established textbook knowledge, the question which processes exactly trigger their invocation remain subject of debate. Here, this work seeks to contribute by investigating muscle metabolism by means of localised multi-nuclear NMR spectroscopy ([N]MRS) during exercise.

Most of the knowledge on muscle metabolism is gathered from biochemical methods – often invasively and/or yielding whole body averages (see section 1.2). NMR spectroscopy is a non-invasive technique that can yield time resolved data from a specifically selected volume. In contrast to the vast majority of previously published

## 1. Introduction

NMR studies, this work opens two windows on metabolism by employing interleaved, i.e. multi-nuclear MRS. With this approach it is possible to monitor the time courses of phosphocreatine (PCr), inorganic phosphate ( $P_i$ ) and ATP by  $^{31}\text{P}$  MRS and, simultaneously, quantify the intramuscular concentration of lactate, total creatine (and other metabolites) by  $^1\text{H}$  MRS.

This work therefore helps in verifying and improving quantitative models of energy metabolism in human muscle.

### 1.1.1. Muscle Anatomy

In this study, subjects performed plantar flexion exercise with a straight knee, in supine position. This type of exercise activates primarily the gastrocnemius muscle [3, 4]. Therefore, spectra were acquired from this muscle with a focus on the medial head of gastrocnemius, as it was positioned in the centre of the magnet.

## 1.2. Techniques to Study Muscle Biochemistry

This chapter closely follows the biochemical rationale and motivation for the application to FWF grant P15202-B02 to E. Moser.

All techniques applied to measure dynamic metabolic events involved in muscular contraction and recovery are indirect methods. Methods established so far are

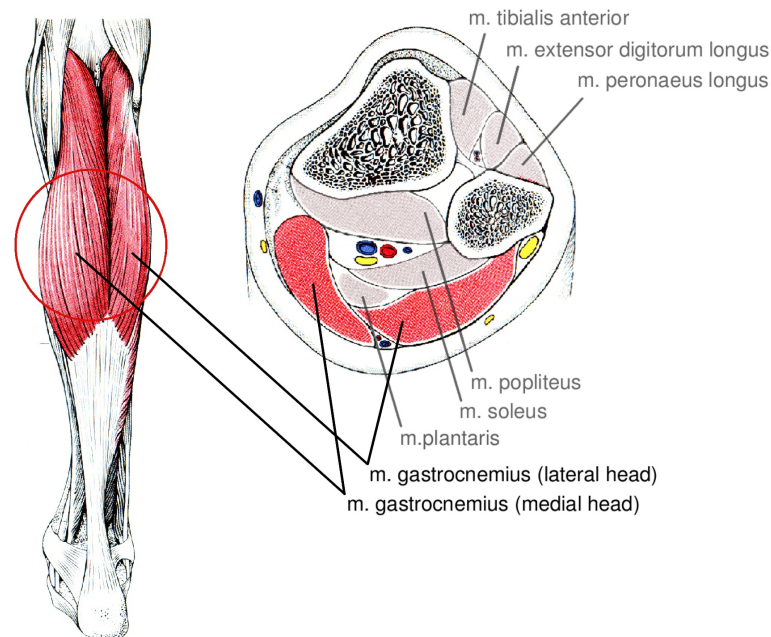


**Figure 1.1:** Muscles of the human lower leg. Figure reproduced from [5] (modified).

## 1. Introduction

measurements of serum metabolites and gas exchange analysis, representing averaged metabolic changes for the whole body. More direct and localised methods are muscle biopsies, microdialysis or open-flow microperfusion [6], the latter also enables the sampling of macromolecules from muscle interstitial fluid (ICF) in humans, however, both techniques show significant limitations, in particular their invasiveness.

Magnetic Resonance Spectroscopy (MRS) has evolved from Nuclear Magnetic Resonance (NMR) methods developed in physics and chemistry and applied with humans *in vivo* after the development of RF-surface coils [7] and the broader availability of (very) high-field whole-body magnets. First, phosphorus ( $^{31}\text{P}$ ) MRS has been developed to follow non-invasively and repeatedly metabolic changes in human muscle *in vivo* during rest, exercise and recovery. Volumes-of-interest (VOI) were selected via the size of the RF-coil and the excitation flip-angle applied, thus being taken as representative of the muscle as a whole (e.g. [8]).

Several research facilities have developed large scale research programs over the last 2 decades to study metabolic events in the human muscle using  $^{31}\text{P}$  MRS. Later on,  $^{13}\text{C}$  MRS and  $^1\text{H}$  MRS have been used to study lactate, glucose and lipid metabolism in the human *in vivo*, respectively. In addition, several localisation techniques have been developed to gain flexibility in choosing the size and location of the VOI (e.g. ISIS, STEAM, PRESS). The different nuclei used to study particular aspects of the complex metabolic pattern, however, have different sensitivity (in the order  $^1\text{H} > ^{31}\text{P} > ^{13}\text{C}$ ) and various problems concerning background signals (i.e. water, fat, unresolved macromolecules), and allow only a glimpse through a "metabolic window". How metabolism looks depends partly on the window used.

In this work, the focus is on a combination of *in vivo*  $^1\text{H}$  and  $^{31}\text{P}$  MRS in human skeletal muscle. First a short summary of the strength and weakness of the two methods for studying muscle metabolism is given and how the combination of both methods, together with improved models, should enhance the quantitative understanding of energy metabolism in human muscle.

### 1.2.1. Muscle Metabolism as Viewed by $^{31}\text{P}$ MRS

An important window on muscle metabolism *in vivo* is via  $^{31}\text{P}$  MRS, a non-invasive technique that despite measuring all-fibre average concentrations of relative few metabolites, can yield time-resolved metabolic data hard to obtain in any other way. In muscle, the creatine kinase equilibrium (see Fig. 1.2) ensures that a temporary shortfall in ATP production is met by a fall in phosphocreatine (PCr) concentration, with a corresponding rise in inorganic phosphate ( $\text{P}_i$ ) and free creatine (Cr). Figure 1.2 shows metabolism divided into an ATP-consuming block (in exercising muscle dominated by the myosin ATPase responsible for generating mechanical force, but also containing e.g.  $\text{Na}^+$ ,  $\text{K}^+$ -ATPase) and an ATP-producing block comprising two components, glycolytic and 'oxidative' (i.e. TCA cycle and oxidative phosphorylation). Glycolysis of glucose to lactate generates 2 ATP molecules (3 ATP per glycosyl unit of glycogen) while full oxidation generates a further 34 ATP. The creatine kinase equilibrium buffers ATP, so any any shortfall in ATP synthesis tends to decrease

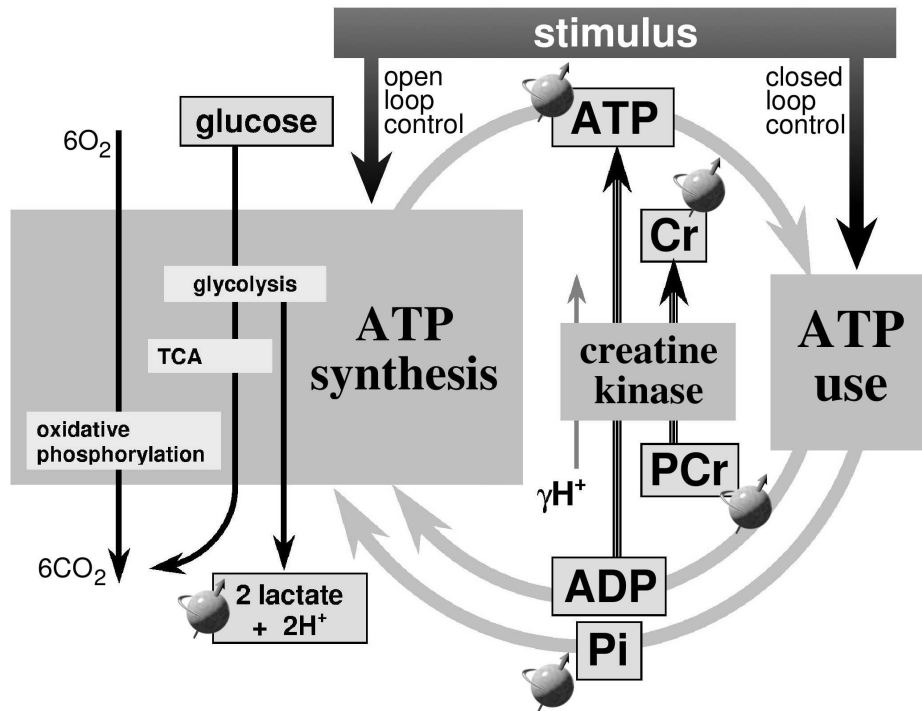


**Figure 1.2:** Muscle energy metabolism as viewed by  $^{31}\text{P}$  and  $^1\text{H}$  MRS. ATP passes from the ATP synthesis block to the ATPase, ADP and  $\text{P}_i$  in the reverse direction. Creatine kinase equilibrates PCr, creatine, ADP, ATP and  $\text{H}^+$ . The metabolites denoted with a sketched spin ( $\bullet$ ) can be detected either by  $^{31}\text{P}$  or  $^1\text{H}$  MRS. In pure closed-loop control a stimulus activates the ATPase, and consequent changes in some signal related to the creatine kinase equilibrium increase ATP synthesis accordingly. In pure open-loop control the stimulus activates ATP synthesis directly (adapted from [9,10]).

phosphocreatine and increase free creatine and inorganic phosphate [11, 12]. Free adenosine di-phosphate (ADP) may increase manifold, but remains lower than adenosine tri-phosphate (ATP), which changes little [11, 12]. If oxidative or glycolytic ATP production can increase, a new steady state may be reached.  $^{31}\text{P}$  MRS can detect PCr,  $\text{P}_i$  and ATP directly, and cell pH, free ADP and the free energy of ATP hydrolysis ( $\Delta G_{\text{ATP}}$ ) can be calculated indirectly [13]. PCr splitting is accompanied by pH-dependent net "consumption" of protons [14], and the algebraic sum of this and the generation of protons accompanying lactate production determines the direction of pH change during exercise: usually acidification follows an initial brief alkalisation phase when proton consumption dominates. The size of the pH change is determined by the ratio of the net proton load to the cytosolic buffer capacity [15, 16].  $^{31}\text{P}$  MRS measurements can be used in various ways to study glycolytic rate [17, 18, 19], contraction cost [13, 20], acid efflux [21, 18] and oxidative (mitochondrial) ATP synthesis [9, 22]. There is a measure of agreement on the fundamental principles of this

## 1. Introduction

kind of analysis, but still considerable controversy about first, many technical aspects of the calculations, and second the correct interpretation of the results in terms of metabolic regulation and (in disease states) metabolic pathophysiology.

### 1.2.2. Muscle Metabolism as Viewed by $^1\text{H}$ MRS

Another window on muscle metabolism *in vivo* is  $^1\text{H}$  MRS, a technique with somewhat higher sensitivity compared to  $^{31}\text{P}$  MRS, however, hampered by the strong signals from water and lipids. Again, all-fibre average concentrations of relatively few metabolites are measured and the strong anisotropy of muscle fibres may cause problems with interpretation/quantification. Also  $^1\text{H}$  MRS requires efficient volume localisation and water- and fat suppression for quantification of total creatine (Cr, i.e. PCr plus free Cr), choline-containing compounds (Cho) and lactate (Lac). So far,  $^1\text{H}$  MRS of muscle *in vivo* has been used to identify Cr changes in response to dietary Cr supplementation [23] and – more controversially – turnover during exercise [24], it has also been used to study extra- and intracellular lipids [25, 26, 27, 28, 29, 30]. Other metabolites (e.g. taurine, carnosine) may be identified using short  $T_E$  and, preferentially, high field  $^1\text{H}$  MRS techniques, although quantification is difficult due to line splitting, spectral overlap and relaxation time effects. For analysis of muscle energetics, the two most relevant measurements are of total creatine and lactate. Total creatine, which is known to vary in relation to dietary creatine intake (and also other factors such as training state, insulin status, etc.), will be important in the accurate quantification of free ADP concentration. As will be explained below, lactate measurements will be of importance in confirming the assumptions of analysis of  $^{31}\text{P}$  MRS studies, and in the assessment of cytosolic buffer capacity. There has so far been only one study of this kind, in isolated frog muscle using interleaved, non-localised  $^1\text{H}/^{31}\text{P}$  MRS at  $40^\circ\text{C}$  and 7 Tesla which suggested that calculations of lactate anion ( $\text{Lac}^-$ ) concentration in exercising muscle estimated via  $^{31}\text{P}$  MRS may overestimate  $\text{Lac}^-$  production [31]. Therefore, an appropriate combination of  $^1\text{H}$  and  $^{31}\text{P}$  MRS techniques and exercise protocols *in vivo* should help to improve quantitative interpretation of muscle bioenergetics [15].

In summary,  $^{31}\text{P}$  MRS provides information about metabolism hard to obtain in any other way in human muscle. Despite a certain degree of agreement about techniques and interpretation, there are a number of areas where assumptions need to be assessed critically, and competing hypotheses tested. This work seeks to contribute to this discussion by combining  $^{31}\text{P}$  with  $^1\text{H}$  MRS, complemented by specific information on the fibre type and gross structures in the muscle under study.

### 1.2.3. Current Limitations and Potential Improvements

The main limitations of  $^{31}\text{P}$  MRS are the inherently low sensitivity and the fact that lactate must be calculated indirectly using several model assumptions not yet fully validated *in vivo* [9, 31]. On the other hand,  $^1\text{H}$  MRS allows direct measurements of lactate but also has potential problems, including relaxation effects, modulated visibility due to residual dipolar coupling of creatine [32, 33] and carnosine [34] and

## 1. Introduction

particularly overlapping strong lipid resonances (at 0.5 – 1.5 ppm) and dipolar coupling effects resulting in reduced lactate visibility [35, 36, 37, 38, 39, 40, 41, 42, 43, 44]. Misinterpretation of any of these effects could result in inaccurate lactate quantification. Early attempts were made to combine the information available from MRS of various nuclei (i.e.  $^1\text{H}$ ,  $^{19}\text{F}$ ,  $^{23}\text{Na}$ ,  $^{31}\text{P}$ ) [45, 46]. However, it turned out that too much may be less, i.e. coil optimisation is less effective if too many frequencies are used and large chemical shift differences do not allow to actually measure spectra from the same VOI. Improved MRS techniques optimised for a particular scientific question in combination with higher field strength, i.e. higher sensitivity and better spectral resolution [47, 48, 49], should allow to overcome or reduce several complications discussed above.

The general hypothesis for the interleaved  $^1\text{H}/^{31}\text{P}$  MRS methodology is that increased sensitivity and spectral resolution at 3 Tesla as well as complementary information on both free and total creatine levels, pH and lactate, allow to study the complex pattern of muscle metabolism in human skeletal muscle in vivo from a broader perspective; the view is improved by looking through more than one window. There have been attempts to measure  $^1\text{H}$  and  $^{31}\text{P}$  MRS simultaneously from the same sample (e.g. in isolated mitochondria [50], in brain [45, 51, 52] or in isolated frog muscle [31, 19]). A study by Brillault-Salvat et al. [53, 54] focussing on interleaved NMR imaging and NMR spectroscopic deoxy-myoglobin and lactate detection and non-localised  $^{31}\text{P}$  MRS using a surface coil was carried out on human calf muscle, yet only in relative units for lactate concentrations due to unresolved NMR visibility questions [55] at that time. Vanderthommen [56] recently studied voluntary and electrically induced contractions by interleaved  $^1\text{H}$  and  $^{31}\text{P}$  MRS in humans, albeit without lactate quantification.

# 2

## Theory of MRS

Relevant theory of NMR basics, especially localised spectroscopy (focussing on STEAM), relaxation, motivation for interleaved measurements and quotation of the product operator formalism to derive an analytical expression of  $S(\tau_1, \tau_2)$  for the DQF lactate signal.

### 2.1. Introduction

The fundamentals of nuclear magnetic resonance can be looked up in various excellent text books, e.g. [57, 58] or lecture notes [59] and have also been reproduced manifold in diploma theses. Here, only selected details which are of particular relevance to this work are outlined, complemented by the basics of the product operator formalism for the description of an NMR experiment in appendix B.1.

### 2.2. Localised NMR Spectroscopy, STEAM

STEAM (STimulated Echo Acquisition Mode) [60, 61, 62] is a single shot technique which is capable to acquire  $B_0$  gradient localised NMR spectra from a cuboid volume of interest (VOI or “voxel”). The signal which is detected is the stimulated echo formed by three consecutive  $90^\circ$  pulses.

In the basic pulse sequence which does not comprise any  $B_0$  gradients, three free induction decays (FIDs), four spin echoes and one stimulated echo are generated, as shown in Fig. 2.1. This phenomenon was described as early as 1950 by Erwin L. Hahn [63] and he stated that “The stimulated echo at  $T + \tau$  is particularly interesting and useful in view of the fact that if  $\tau$  is sufficiently small [...], the signal survives as long as  $T_1$  permits”.

## 2. Theory of MRS

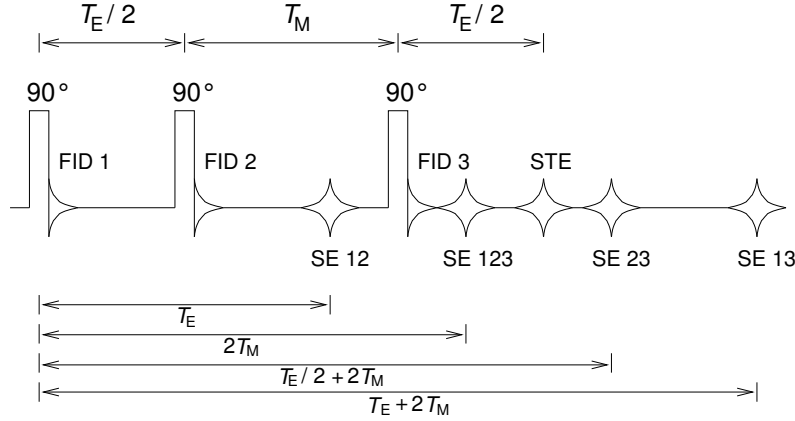


**Figure 2.1:** RF signals occurring during a sequence comprising three RF pulses: Three FIDs, four spin echoes (SE) and one stimulated echo (STE) are generated. The stimulated echo is formed at  $t = T_E + T_M$ .

To observe only the stimulated echo, however, all other echoes and FIDs have to be eliminated. In principle, this could be achieved by phase cycling of the RF pulses, but since this approach, when used alone, is prone to motion artifacts and degrades the sequence's single scan character, the use of crusher gradients in the middle period  $T_M$  is preferred. However, when signal is averaged, as is usually the case during in vivo measurements, both methods are applied. The ' $T_M$ -crusher' removes all unwanted coherences except the FID after the last pulse of the sequence which can be dephased by applying a further  $B_0$  spoiler gradient in the first  $T_E/2$  delay and an identical spoiler in the last  $T_E/2$  period [57].

Besides excellent localisation accuracy, the advantage of the sequence is that the echo time can be extremely short while the  $T_M$  period can be used for additional water suppression in  $^1\text{H}$ -NMR spectroscopy. The main disadvantage is that the stimulated echo represents only 50% of the available signal from the VOI. The sequence is shown with localisation gradients in Fig. 2.2.

The phase modulation of  $J$ -coupled spins is far more complicated with STEAM than for e.g. a PRESS sequence (basically consisting of  $90^\circ - 180^\circ - 180^\circ$  pulses) since the multiple  $90^\circ$  pulses can create multiple quantum coherences. A product operator formalism using raising and lowering operators (as introduced in section 2.3) can be applied to derive analytical expressions for an  $IS$  spin system or for  $I_2S$  and  $I_3S$  spin systems [57, 64]. After the first  $90_x^\circ$  pulse, the density operator for the  $I$  spin,  $\sigma_I(0+)$  is given by

$$\sigma_I(0+) = \frac{i}{2} (I^+ - I^-). \quad (2.1)$$

In the first  $T_E/2$  period, the coherences evolve under chemical shift,  $J$ -coupling and the  $T_E$  crusher gradient  $G_1$ . Immediately prior to the second  $90^\circ$  pulse, the density

## 2. Theory of MRS

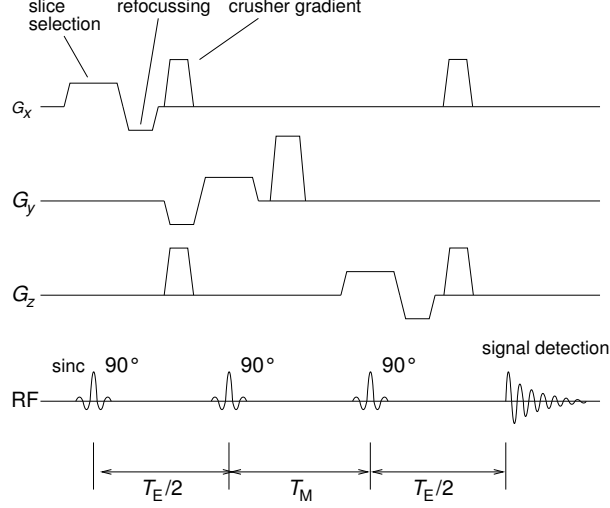


**Figure 2.2:** Schematic of the STEAM sequence. Three  $90^\circ$  pulse are applied in the presence of balanced slice selection gradients ( $G_x, G_y, G_z$ ). Crusher gradients dephase unwanted magnetisation.

operator is, therefore, given by

$$\begin{aligned} \sigma_I\left(\frac{T_E}{2}-\right) &= \frac{i}{2} (I^+ e^{-i\theta} - I^- e^{+i\theta}) \cos\left(\frac{\pi J T_E}{2}\right) \\ &\quad + (I^+ e^{-i\theta} - I^- e^{+i\theta}) S_0 \sin\left(\frac{\pi J T_E}{2}\right) \end{aligned} \quad (2.2)$$

with

$$\theta = \frac{\omega_I T_E}{2} + \gamma \vec{r} \int_0^T G_1(t) dt, \quad (2.3)$$

i.e. the sum of chemical shift evolution and  $B_0$  gradient dephasing, where  $T$  is the length of the first gradient pulse.

After the second  $90_x^\circ$  pulse the density operator  $\sigma_I(T_E/2+)$  consists of longitudinal magnetisation, single-, double-, and zero-quantum-coherences. All transverse components are dephased by the  $T_M$  crusher gradient, except zero-quantum-coherences.

Continuing the computations [57,64] with the reduced density operators and taking into account polarisation transfer between the spins  $I$  and  $S$  finally yields the net doublet signal  $S(T_E + T_M)$  for the real part of the doublet signal of spin  $I$  in an  $I_n S$

## 2. Theory of MRS

spin system

$$\begin{aligned}
 S(T_E + T_M) &= \frac{1}{2} \left( \cos^2 \left( \frac{\pi J T_E}{2} \right) - \frac{1}{2} \sin^2 \left( \frac{\pi J T_E}{2} \right) \right. \\
 &\quad \times \left[ 1 - \cos^{n-1} \left( \frac{\pi J T_E}{2} \right) \cos \left( \frac{\Delta\omega T_E}{2} \right) \right] \\
 &\quad \left. \times \cos^{n-1} (\pi J T_M) \cos (\Delta\omega J T_M) \right) \quad (2.4)
 \end{aligned}$$

where  $\Delta\omega = \omega_I - \omega_S$ . The first term originates from the  $I$  single quantum coherence which was along the longitudinal axis during  $T_M$ . The second term includes contributions from the  $I$  and  $S$  spins, it originates from zero quantum coherences during  $T_M$ . The latter term causes rapid fluctuations in signal for varied  $T_M$  but is small for echo times short compared to  $2/(J\pi)$ . The fact that in the stimulated echo only 50 % of the available magnetisation is refocused, can clearly be seen from the first factor in eq. 2.4.

### 2.3. Product Operator Formalism and DQF Spectroscopy

The product operator formalism for the description of NMR pulse experiments has been introduced by Sørensen in 1983 [65] and is described in text books on NMR [58] and various review articles [66]. The formalism is applicable to weakly coupled spin systems and represents a middle course between classical vector model (intuitive but incapable to describe e.g. the evolution of multi quantum coherences) and the more precise density operator theory which rapidly becomes cumbersome for the description of pulse sequences comprising more than just a few pulses.

#### 2.3.1. Principle of a Double Quantum Filter

A double quantum filter exploits the property of double quantum coherences (DQC, see Appendix B.1) of being twice as sensitive to  $B_0$  gradients as single quantum coherences (SQC) (eq. B.8). Zero quantum coherences (ZQC) are not sensitive to  $B_0$  gradients at all. When a spin system is prepared in such a way that it is in double quantum state while a  $B_0$  field gradient  $G_1$  is applied, and brought to single quantum state before a gradient  $G_2$  with half the amplitude (and same duration) is applied, only magnetisation for which this particular condition (see section B.1.3) holds true can be detected at a later stage in the sequence.

This property can be exploited for filtering out overlaying lipid resonances from  $^1\text{H}$  spectra by selectively irradiating the coupling partner of the lactate  $\text{CH}_3$  resonance and thus creating exclusively lactate DQC. The double quantum filter, however, never works perfectly, i.e. it does not destroy lipid resonances by 100 %. Spurious magnetisation is only defocussed deterministically by the spoiler gradients according to

## 2. Theory of MRS

sin/cos functions. Additional phase cycling can improve the suppression of unwanted magnetisation.

A double quantum filter can be rendered volume selective [67] (i.e. transformed into a single voxel spectroscopy sequence) by applying slice selection gradients during non-frequency-selective RF pulses, as shown in Fig. 2.3.

### 2.3.2. Lipid Pre-Inversion

A pre-inversion module can further reduce unwanted lipid magnetisation by taking advantage of the short  $T_1$  of lipid resonances ( $T_1 = 300$  ms). Due to the signal's inversion recovery function  $S(T_{IR}) = S_0(1 - 2e^{-T_{IR}/T_1})$ , the magnetisation may be prepared to cross the zero  $z$ -magnetisation when the DQF sequence is applied after the inversion recovery time of  $T_{IR} = 208$  ms. The lactate resonance ( $T_1 \approx 1$  s) is also inverted and reduced in amplitude by 37%, but lipid contamination of spectra can be reduced significantly, so that this SNR loss is rewarded by a gain in specificity.

### 2.3.3. Orientation Dependence and Residual Dipolar Coupling of Lactate in Skeletal Muscle

Lactic acid is a carboxylic acid, its chemical formula is  $C_3H_6O_3$ . The systematic name, 2-hydroxypropanoic acid, reflects its structure. In solution, lactic acid can lose a proton from the COOH carboxy group, turning into the lactate anion  $CH_3CHOHCOO^-$ . Decoupling experiments on the triple quantum coherence of the lactate  $IS_3$  spin system done by Asllani et al. [35] showed that the observed frequency splitting was mainly due to the dipolar interactions between the methine (CH) and methyl ( $CH_3$ ) protons of the lactate molecule. The authors therefore conclude that all the proton resonances of the lactate molecules in muscle behave anisotropically in the magnetic field.

Two pools of lactate can be observed in postmortem muscle, one which exhibits anisotropic dipolar coupling interactions and the other without any detectable dipolar coupling effects [35]. Transverse relaxation rates of these pools differ.

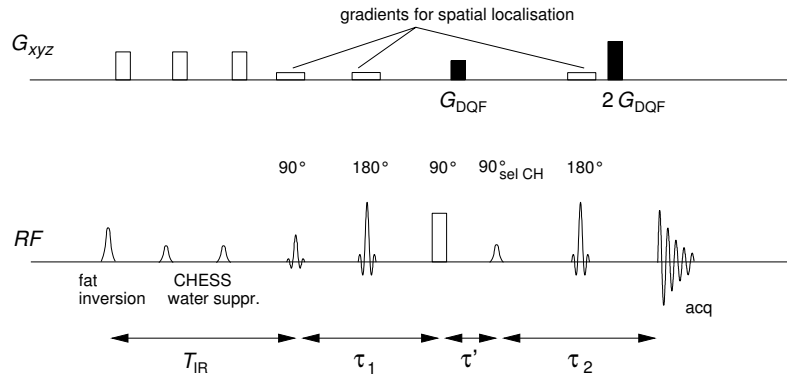


**Figure 2.3:** Schematic diagram of the double quantum filter (DQF) pulse sequence for lactate detection in muscle.

## 2. Theory of MRS

The observed splitting [35] for a spin system with both dipolar ( $\Delta_{\text{dc}}$ ) and scalar ( $J = \Delta_{\text{HH}}$ ) coupling (i.e. the pool exhibiting dipolar coupling effects) corresponds to the algebraic sum  $\Delta = \Delta_{\text{HH}} + \Delta_{\text{dc}}$  [68].

The signal received after application of the DQF sequence for selective lactate detection and suppression of overlaying strong lipid resonances at the spectral position of the lactate  $\text{CH}_3$  group at 1.3 ppm (see Fig. 2.3) can be calculated using the product operator formalism for an  $IS_3$  spin system (see appendix B.1 and Asllani et al. [36]) and is given by

$$A = A_0 \left\{ a \sin(\pi J \tau_1) \sin(\pi J \tau_2) (1 + \cos^2(\pi J \tau_1)) e^{-\tau_1/T_{21}} e^{-\tau_2/T_{21}} \times \right. \\ \left. b \sin(\pi \Delta \tau_1) \sin(\pi \Delta \tau_2) (1 + \cos^2(\pi \Delta \tau_1)) e^{-\tau_1/T_{2s}} e^{-\tau_2/T_{2s}} \right\}. \quad (2.5)$$

Here, the symbols denote:

- $A$  ..... the measured NMR methyl lactate signal
- $A_0$  ..... theoretical maximum methyl signal at  $\tau_1 = 0$  and  $\tau_2 = 0$  in the absence of modulation
- $\tau_1, \tau_2$  .... echo time delays in the DQF sequence (see Fig. 2.3)
- $J$  ..... scalar coupling constant;  $J = \Delta_{\text{HH}} = 7 \text{ Hz}$
- $\Delta$  ..... observed coupling constant,  $\Delta = \Delta_{\text{dc}} + J$ , where  $\Delta_{\text{dc}}$  is the orientation dependent dipolar coupling constant, governed by a term  $(3 \cos^2 \varphi - 1)$  (neglecting a transformation between the laboratory- and the molecular frame of reference, as detailed below).
- $a, b$  ..... fraction of lactate in each pool;  $a = 19 \pm 3 \%$ ,  $b = 82 \pm 2 \%$
- $T_{21}, T_{2s}$  .. transverse relaxation times of the lactate pools;  $T_{21} = 142 \pm 8 \text{ ms}$ ,  $T_{2s} = 37 \pm 6 \text{ ms}$

The dipolar coupling contribution  $\Delta_{\text{dc}}$  can be calculated according to [35, 32], with the Euler angles  $\theta$  and  $\phi$  defining the transformation between the laboratory frame and the molecular frame of reference which indicate the orientation of the methine-methyl vector in lactate molecules:

$$\Delta_{\text{dc}} = 1.5 D_0 [1 - 3(\cos \theta \cos \alpha - \sin \theta \sin \phi \sin \alpha)^2]. \quad (2.6)$$

The angle  $\alpha$  is defined to be zero when the fibres are oriented parallel to  $B_0$ . The dipolar coupling constant  $D_0$ ,  $\theta$  and  $\phi$  were found by Asllani et al. [35] via fitting data acquired from bovine ex vivo muscle specimens:  $D_0 = -5.9 \text{ Hz}$ ,  $\theta = 10^\circ$ ,  $\phi = 26^\circ$ .

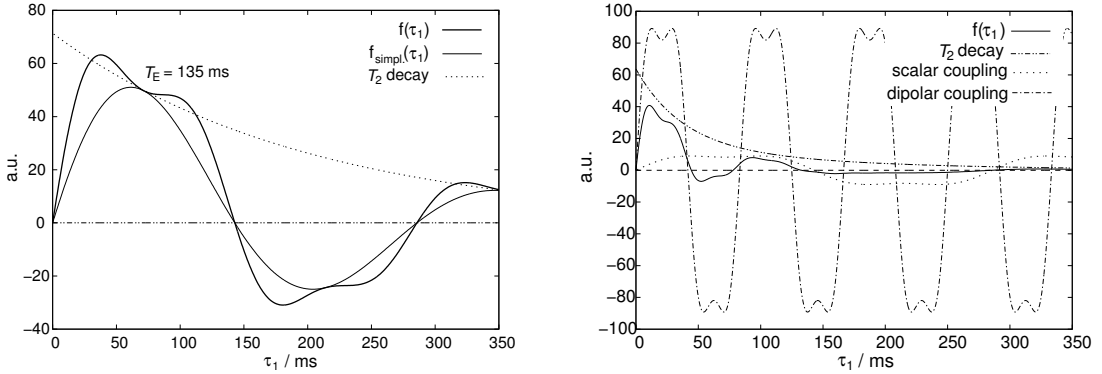
### 2.3.3.1. Numerical Simulations of the DQF Signal

As has been pointed out in the previous section and is implicitly comprised in eq. 2.5, the lactate methyl NMR resonances behave differently with respect to echo time of the

## 2. Theory of MRS

NMR pulse sequence used for acquisition (see Fig. 2.3), when dissolved in an isotropic medium (e.g. in aqueous solution) or in an anisotropic structure (e.g. muscle tissue). Fig. 2.4 shows the dependence of the lactate methyl signal over echo time for a solution and for muscle tissue which is oriented parallel to the magnetic field. In the latter case, dipolar components oscillating with the frequency  $\Delta$  appear as multiplicative factors. Note that optimum signal is obtained for  $T_E \approx 135$  ms (with an additional  $T_2$  dependence) in an isotropic medium only, while in muscle tissue the maximum is found at a shorter echo time. In muscle tissue the signal  $S(\tau_1, \tau_2)$  may even cross zero at  $T_E = \tau_1 + \tau_2 = 135$  ms. In the example in Fig. 2.4,  $S(67 \text{ ms}, 67 \text{ ms})$  is negative, with a very low magnitude. This behaviour has previously been described as “low lactate visibility” in muscle [55, 40].

The DQF signal’s echo time dependence has been simulated and is shown in Fig. 2.5, varying  $\tau_1$  (with constant  $\tau_2$ ) and varying  $\tau_2$  (with constant  $\tau_1$ ). The fibre orientation chosen for this simulation is parallel to the  $B_0$  field ( $\varphi = 0^\circ$ ). Fig. 2.6 shows simulations of the same methyl lactate signal measured with the same DQF sequence (Fig. 2.3) as surface- and contour plots, i.e. with  $\tau_1$  and  $\tau_2$  on the two abscissae. Four fibre orientations, which are very likely to occur in muscle tissue when the limb is placed parallel to the magnet, are shown:  $\varphi = \{0^\circ, 24^\circ, 30^\circ, 40^\circ\}$ , with parallel orientation ( $\varphi = 0^\circ$ ) being the least realistic. The maximum signal yield is expected when all muscle fibres are oriented parallel and the echo time is chosen accordingly, i.e.  $(\tau_1, \tau_2) \approx (10 \text{ ms}, 20 \text{ ms})$  and  $T_E = 30 \text{ ms}$ .



(a) In an isotropic medium, (aqueous solution or brain), maximum signal is obtained at an echo times close to  $T_E = 135$  ms, depending on  $T_2$ . ( $T_E = \tau_1 + \tau_2$ ,  $\tau_2 = 67.0$  ms)

(b) Components of the lactate signal simulated for anisotropic tissue, e.g. muscle fibres oriented parallel to the magnetic field  $B_0$ . The maximum is shifted towards a shorter echo time. ( $\tau_1 = 20.4$  ms)

**Figure 2.4:** Simulation of the methyl lactate signal (eq. 2.5) measured with the sequence shown in Fig. 2.3, in an isotropic medium (a) and in muscle (b), dissected into its components.

## 2. Theory of MRS

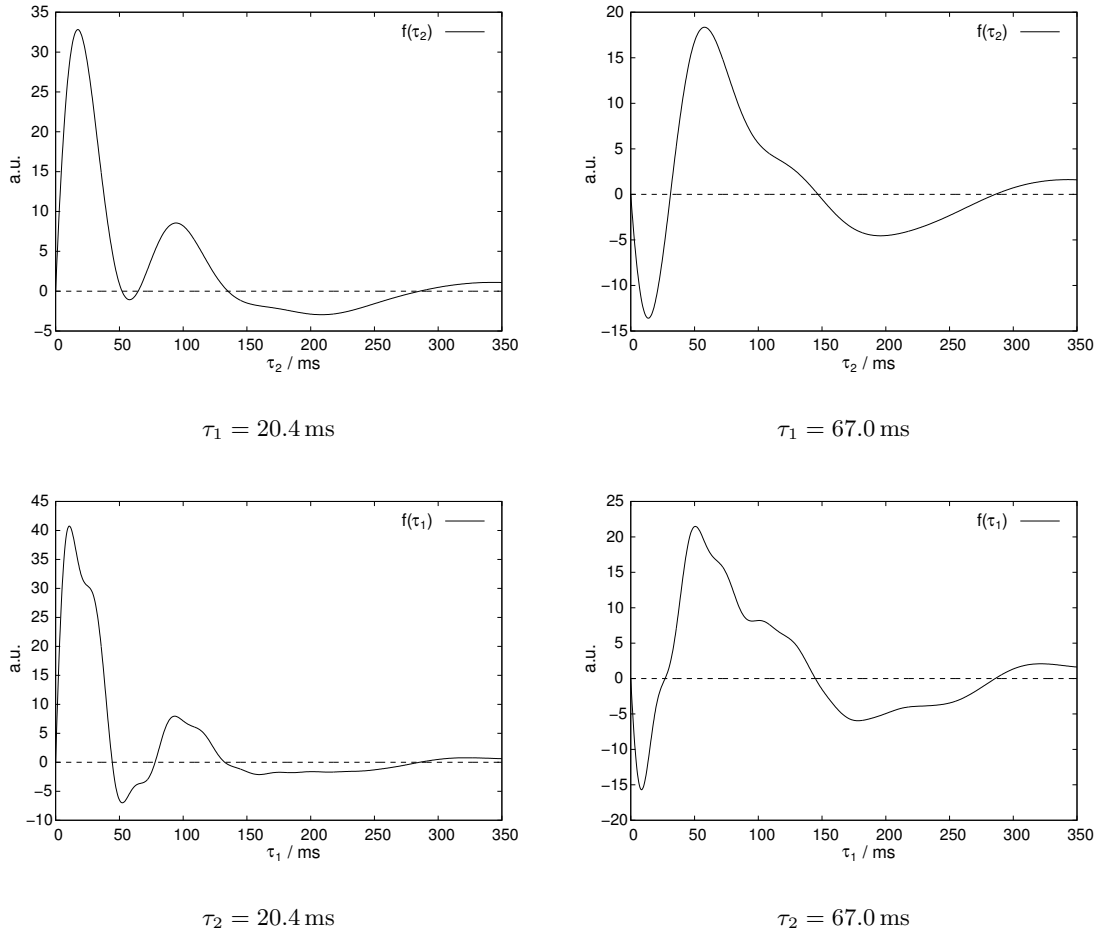


**Figure 2.5:** Simulation of the methyl lactate signal measured with the DQF sequence (see Fig. 2.3) as given in eq. 2.5 against  $\tau_{1,2}$ , with  $\tau_{2,1}$  fixed. Muscle fibres are oriented parallel to the magnetic field  $B_0$ .

This set of parameters may cause the NMR system to hit a technical limit, given a specific sequence design, as e.g. spoiling gradients require some minimum delay ( $d \gtrsim 3 \text{ ms}$ ) to take effect without causing noticeable eddy current artifacts and the pulse sequence needs to meet some symmetry requirements. But this technical limitation, which could eventually be overcome quite easily, is not the only reason why not to employ such short echo times, as is detailed below.

### 2.3.3.2. Choosing the Best Possible Compromise for the Echo Time

The question which echo time – or pair of  $\tau_1$  and  $\tau_2$  – is an optimal choice for quantifying lactate in skeletal muscle has to be considered carefully: The orientation of

## 2. Theory of MRS

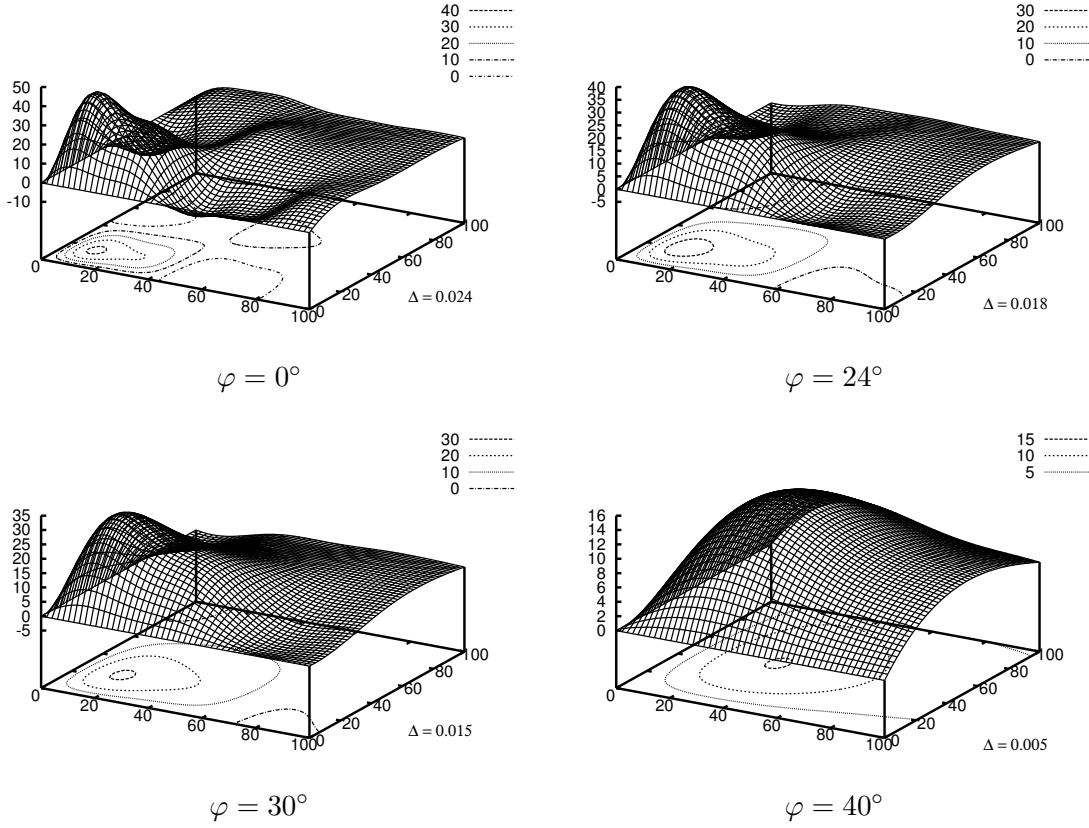


**Figure 2.6:** Simulation of the methyl lactate signal measured with the DQF sequence (see Fig. 2.3) as given in eq. 2.5 against  $\tau_1, \tau_2$  with the orientation  $\varphi$  relative to  $B_0$  as parameter. Note that the peak signal amplitude decreases and the peak moves towards longer echo times ( $\tau_1, \tau_2$ ) as the angle  $\varphi$  between muscle fibre orientation and the orientation of the main magnetic field  $B_0$  increases. Please also note that each graph is scaled differently.

fibres varies between muscles and, to a lesser extent, also across a single muscle itself (imagine the calf muscles being pressed against other muscles or even a hard object, e.g. the surface coil). In gastrocnemius muscle, the fibres are oriented at ca.  $24^\circ - 35^\circ$  relative to  $B_0$ , when the leg (femur) is placed parallel to the magnet bore [69].

**In the ideal case** a fibre orientation of  $\varphi = 24^\circ$  is assumed. The optimum pulse sequence parameters ( $\tau_1, \tau_2$ ) to yield maximum signal for this orientation can be read from Fig. 2.6 to be approximately (15 ms, 22 ms). Deviations from the assumed fibre orientation of  $24^\circ$  by factors like non-parallel orientation of the limb relative to the magnet, deformation of the muscle caused by positioning and strapping to the experimental apparatus or biological variations may introduce severe quantification errors, as signal inevitably drops when the optimum can no more be sustained. This can be seen in Fig. 2.7 which visualises the angle dependence of  $S(\tau_1, \tau_2, \varphi)$ . Fig. 2.7 (b)

## 2. Theory of MRS

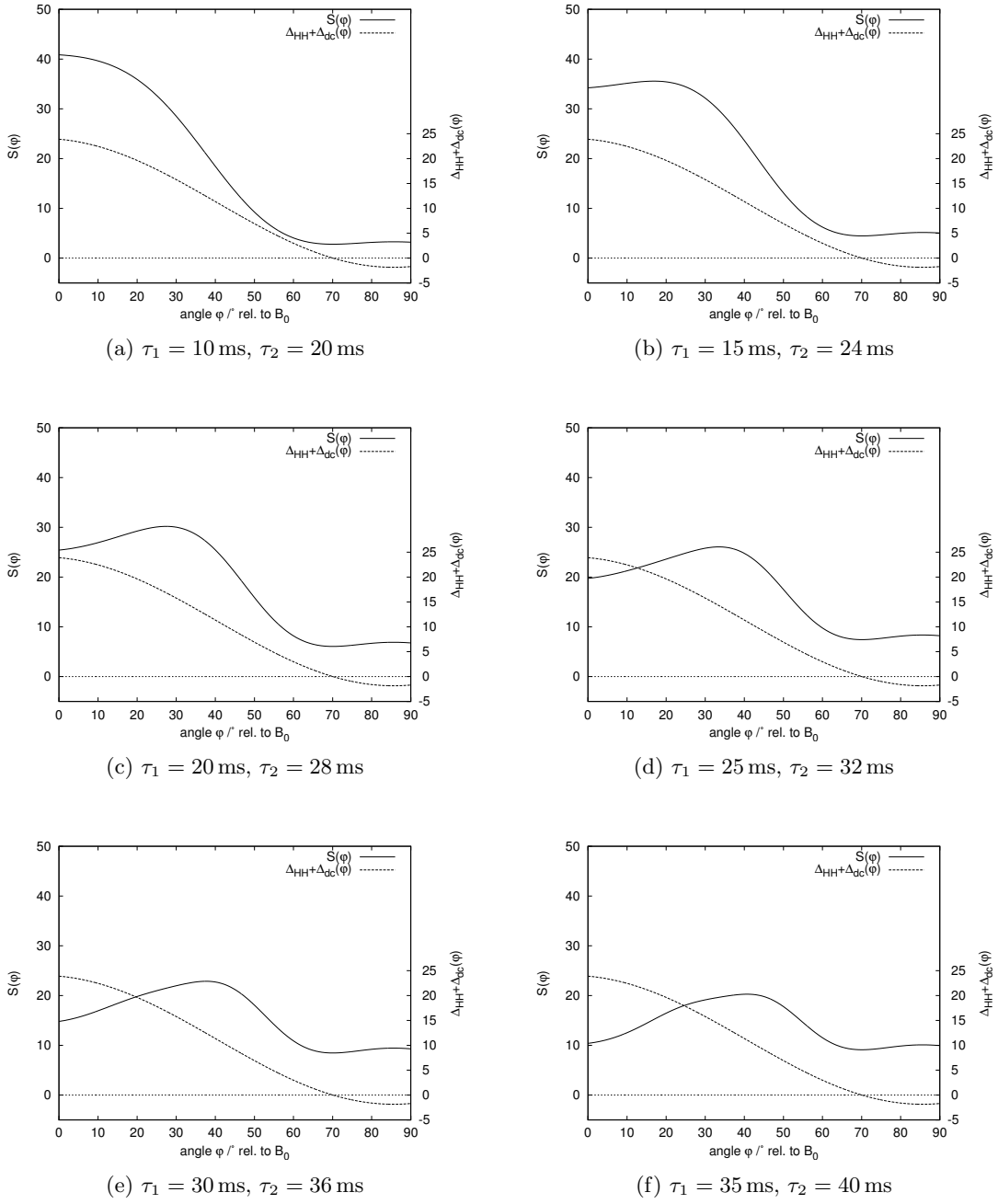


**Figure 2.7:** Simulation of the methyl lactate signal measured with the DQF sequence (see Fig. 2.3) as given in eq. 2.5, varying orientation  $\varphi$ , with fixed  $\tau_{1,2}$ . The effective splitting  $J + \Delta_{dc}$  is calculated according to eq. 2.6. The parameters  $\tau_{1,2}$  are chosen to follow the trace of the global maximum of  $S(\tau_1, \tau_2)$ , that can be seen in the surface- and contour plots in Fig. 2.6.

## 2. Theory of MRS

corresponds most closely to the situation assumed here,  $(\tau_1, \tau_2) = (15 \text{ ms}, 22 \text{ ms})$ . The signal is maximal if fibres are oriented at  $24^\circ$ , which is as close to parallel to  $B_0$ , as ever possible for gastrocnemius fibres. If the orientation changes by only  $+10^\circ$  to  $35^\circ$ , the region of the steepest slope of the curve in Fig. 2.7 (b) is reached, which means severe signal drop of  $\sim 25\%$  from approximately 35 to 25 in arbitrary units of  $S(\tau_1, \tau_2, \varphi)$ , dependent on the hard to control parameter of fibre orientation.

It seems, therefore, advisable not to aspire an optimum signal which is achievable when all parameters are tuned to their (theoretically) ideal values (i.e. the muscle being oriented with the smallest angle relative to  $\vec{B}_0$  and  $\tau_1, \tau_2$  adjusted to the maximum signal for this orientation), as detailed above, but to choose a *robust compromise* where the signal yield is still acceptable but deviations result in smaller quantification errors.

**A more realistic example** is a fibre orientation of  $\sim 30^\circ$  in human gastrocnemius. (Orientations between  $24^\circ$  and  $35^\circ$  have been found by Vermathen et al. [69].) The simulated lactate methyl signal has a flat maximum in the particularly interesting regime of  $25^\circ < \varphi < 35^\circ$  using the parameters  $20 \text{ ms} < \tau_1 < 25 \text{ ms}$  and  $28 \text{ ms} < \tau_2 < 32 \text{ ms}$ , as can be seen Fig. 2.7 (c) and (d). Around this maximum, the orientation angle dependence of  $S(\varphi)$  is reduced compared to the situation of  $(\tau_1, \tau_2) = (15 \text{ ms}, 22 \text{ ms})$  described above, where the slope of  $S(15 \text{ ms}, 22 \text{ ms}, \varphi)$  is steep around  $\varphi = 30^\circ$ .

Considering that the calf muscle may move to a slightly tilted position at the onset of exercise, the parameters  $(\tau_1, \tau_2) = (25 \text{ ms}, 32 \text{ ms})$  were chosen for the final experiments.

$S(25 \text{ ms}, 32 \text{ ms}, \varphi)$  has its maximum of ca. 26 a.u. at  $\varphi \approx 33^\circ$  (see Fig. 2.7 (d)) and drops to  $\sim 24$  or  $\sim 22$  a.u. when the orientation changes by  $\pm 10^\circ$ , corresponding to a signal variation of only 7% and 15%, respectively.

Even if fibre orientation is more parallel than  $33^\circ$  which was the assumption for the previous consideration,  $(\tau_1, \tau_2) = (25 \text{ ms}, 32 \text{ ms})$  is a better choice than a shorter echo time with respect to robustness, because the slope of  $S(\tau_1, \tau_2, \varphi)$  is flatter towards lower angles than towards larger angles, and possible error as well as SNR loss is small. A source of error on the order of 10% - 15% (or even less) seems acceptable, given the inaccuracy of the other parameters of influence, last but not least the fitting error of NMR spectra with low SNR. An inaccuracy of 25% however, as would be the case for a very short echo time tuned to an assumed angle of  $24^\circ$  may easily become the dominating factor of total measurement error.

**Part II.**

**Experimental**

# 3

## Construction of the Exercise Rig

Features of the MR compatible ergometer, calibration of its sensors and tests of the MR compatibility and of the effectiveness with respect to calf muscle activation.

### 3.1. Introduction

Several ergometer designs, useful in an MR magnet, have been published (e.g. [70,71]), however, none of them is fully convincing or commercially available. Therefore, an ergometer, optimised for application in our 3 Tesla magnet (Fig. 3.1) was developed.

### 3.2. Mechanics

The geometry of the ergometer's pedal is shown schematically in Fig. 3.2. The pedal's pivot point has to be coaxial with the ankle, otherwise the foot will inevitably slip on the pedal during exercise. The maximum and minimum pedal angle is restricted to  $-12^\circ$  and  $+56^\circ$  relative to the leg's longitudinal axis, which corresponds to the angular range a normal subject can easily bend the foot during plantar flexion. During construction of the pneumatic system, care has been taken that the angle of the pneumatic piston itself (displacement volume: 1,7l) covers a range which ensures that an angular increment on the pedal is transformed into as approximately constant displacement increment of the piston, in other words: that there is no change of leverage or even a dead centre over the pedal's operative range. An important boundary condition was to fit the whole system into the relatively small magnet bore of  $\varnothing = 55$  cm, also not to use ferromagnetic materials, and only few conducting materials, e.g. aluminium bolts (not moving during exercise) for fixation on the patient bed.

### 3. Construction of the Exercise Rig



**Figure 3.1:** The 3 T Bruker Medspec S 300 DBX whole-body scanner (Bruker Biospin, Ettlingen, Germany), installed at the MR Centre of Excellence, Vienna Medical University. The inner diameter of the magnet bore including the whole-body gradient system is 55 cm. A background light is shining through a glass sphere.

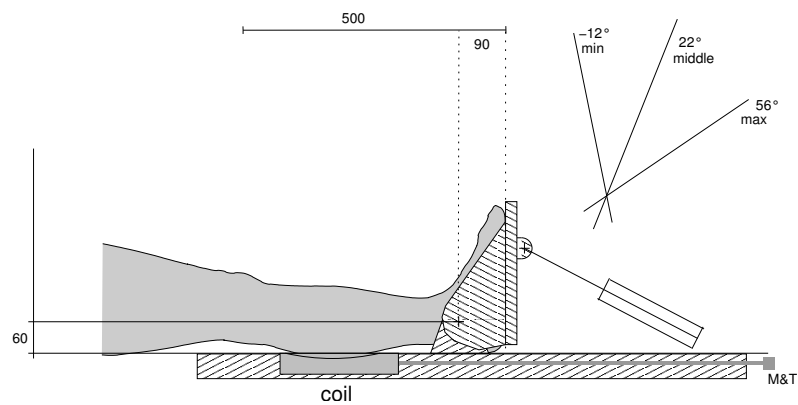


**Figure 3.2:** Geometry of the ergometer's pedal, schematically. The maximum and minimum pedal angle is restricted to the angular range, a normal subject can easily bend the foot during plantar flexion. "M&T" denotes the adjustment rods for matching and tuning the RF coil. Length units are given in mm.

### 3. Construction of the Exercise Rig

The surface coil is also shown schematically, in Fig. 3.2. It is positioned in a groove in the exercise rig's plywood frame, directly below the subject's calf and can be shifted lengthwise for adjusting the position to the subject's size. Figs. 3.3 and 3.4 show the individual parts of the exercise rig's pneumatic system and pedal and the complete rig, half inserted into the magnet bore.

The lower leg and foot can be strapped to the rig and pedal with three belts (white straps in Fig. 3.5) to minimise motion of the calf muscle. By varying the pneumatic pressure the pedal force can be adjusted remotely and even during the NMR measurement, e.g. to match the subject's maximum voluntary contraction force (MVC) – which is useful for multi-power (e.g. ramp) exercise protocols. Exercise is recorded continuously by the force and angle sensors on the pedal described below (see Fig. 3.5 and Results section), an LED bar has been constructed to indicate the pedal angle for subject feedback.

## 3.3. Sensors

### 3.3.1. Sensor Hardware

**Two force sensitive resistors** (IEE FSR™, type FSR-154 AS, Conrad Electronic GmbH & Co.KG, Wels, Austria) with a square active area of 14.2 cm<sup>2</sup> were attached to the pedal of the exercise rig. The FSRs are arranged side by side near the pedal's tip at the position of the ball of the foot when exercising. Their position is shifted by 2.5 cm in A-P direction to match the shape of a right foot (see Fig. 3.6). For reproducible activation, the sensors are activated via a perspex plate ( $\varnothing = 14$  mm) and bevelled butyl rubber pads. This is necessary because the FSR reacts very sensible to the exact distribution and angle of the force exerted (hence the fixed perspex plate) but needs to be activated by a ductile medium.

A force sensitive resistor has a strongly non-linear characteristic curve  $R(F)$  and



**Figure 3.3:** Individual parts of the ergometer's pneumatic system and pedal: cylinder (a) and its axis (b), piston (c), pedal (d) and its axis (e), flexible pneumatic tube (f), throttle valve (g) connecting tube and reservoir (not shown).

### 3. Construction of the Exercise Rig

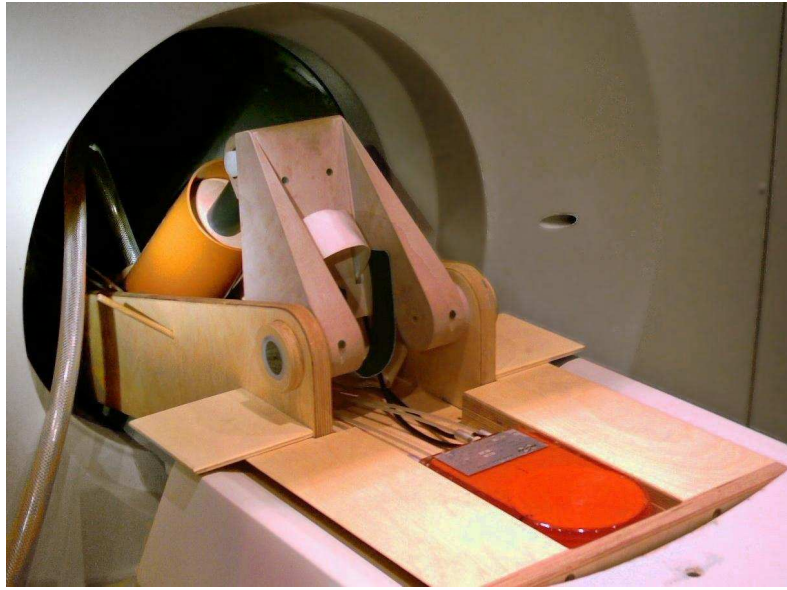


**Figure 3.4:** Ergometer (exercise rig) installed on the patient bed, half inserted in the magnet bore. Note: Force sensors not yet attached.

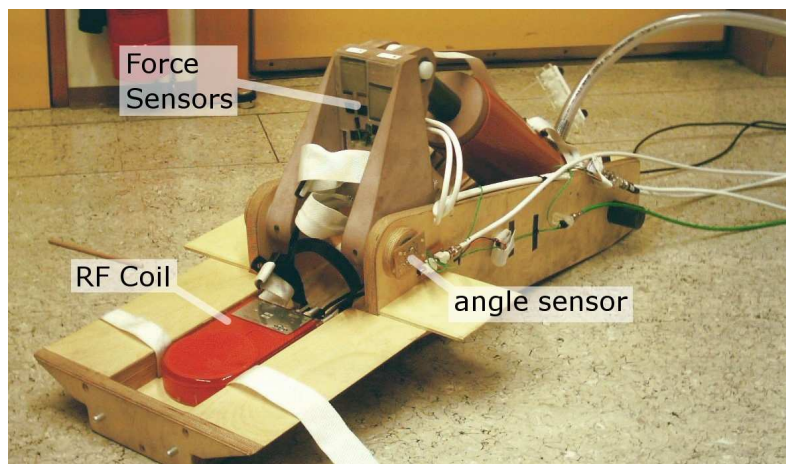


**Figure 3.5:** Non-magnetic ergometer with pneumatic piston, RF coil and sensors for monitoring pedal force and angle. Photograph taken outside the magnet for better visibility.

### 3. Construction of the Exercise Rig

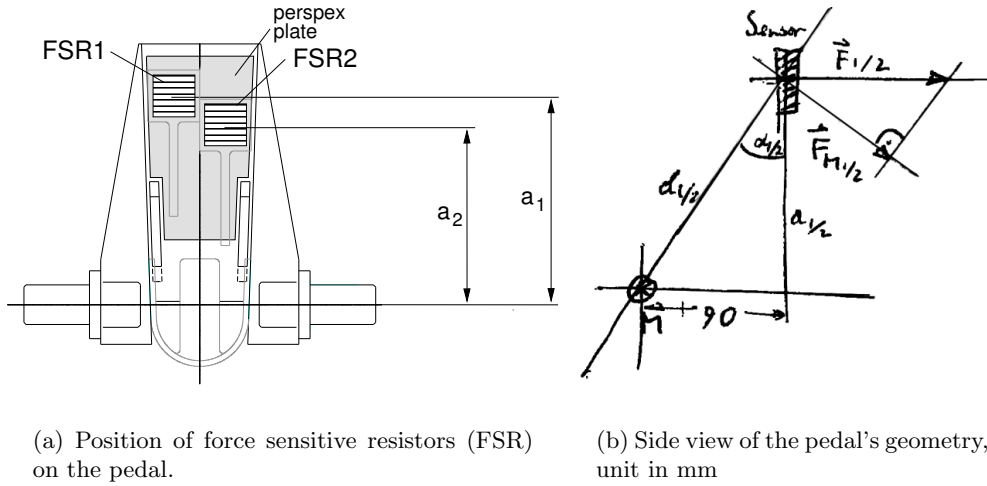


**Figure 3.6:** Position of force sensitive resistors (FSR) on the pedal (a). The sensors are located under the ball of the right foot of an average male subject. Forces  $\vec{F}_{1/2}$  can be converted to torque  $\vec{M}$  using the geometric relation shown in the side view (b).

is commonly used together with an operation amplifier to compensate for this non-linearity, as described in the FSR-154AS's data sheet. (For circuit diagram see appendix A.1.) The sensors are driven by  $U = 12\text{ V DC}$  fed to the circuit via the filter plate (located in the wall of the RF shielded magnet room).

**A pedal angle sensor** was constructed by attaching a potentiometer and a series resistor to the pedal's axis and measuring the voltage drop across the potentiometer. The angle sensor is also powered by  $12\text{ V DC}$  and connected to the voltage source and measurement device via shielded cables, connected across the magnet room's filter plate.

**A data acquisition card** (Meilhaus Electronics, Puchheim, Germany) was installed in a PC running Linux (SuSE 7, Kernel 2.4, later Debian SID, Kernel 2.6). Kernel modules provided by the manufacturer were tailored and a command line tool for data acquisition and storage in ASCII format were programmed in C++ (acknowledgements to DI Michael Kilzer).

Data were recorded in differential mode with 100 samples per second and per channel, sweeping three channels. The angle sensor is connected to channel 1, the two force sensors on the pedal (for their positions see Fig. 3.6) are connected to channels 3 (FSR1) and channel 5 (FSR2). Switching time between the channels was 1 ms. Trigger signals from the NMR scanner were also recorded (on channel 0). All channels were set to a dynamic range of  $-5\text{ V}$  to  $+5\text{ V}$ .

### 3.3.2. Calibration Data

For calibration data – i.e. voltage over angle and voltage over force – of the sensors, see Figs. 3.7 and 3.8. The pedal was moved or loaded in steps of  $5^\circ$  or 100 N, respectively.

For the measurement series with dual STEAM acquisition (chapter 5), the subject’s maximum test force was estimated using a Biodex Multi-Joint-System 3 Pro (Biodex Medical Systems, Inc., NY, USA) dynamometer (acknowledgements to Dr. Carina Zöch and Dr. Richard Crevenna, Department for Physical Medicine and Rehabilitation, Vienna Medical University, Austria). Measurements were done with a straight knee, during dynamic plantar flexion at constant angular velocity (2 seconds for one plantar flexion, imposed by the dynamometer), individually for each subject one week before the NMR measurement. The Biodex system’s output is a torque, given in Nm.

Torque and force on the pedal can be converted using the geometric relations shown in Fig. 3.6 (b), with  $a_1 = 167$  mm,  $a_2 = 132$  mm, and the cathetus in Fig. 3.6 (b) 90 mm, which is the distance between the pedal’s fulcrum and the point where the heel touches the pedal, as given in Figs. 3.2 and 3.6 (b). The result of this consideration is that the forces correspond to torques as follows:  $M_1 = F_1 \cdot 0.176$  Nm/m and  $M_2 = F_2 \cdot 0.132$  Nm/m, with total torque  $M = M_1 + M_2$ .

Later, for triple interleaved measurements and lactate quantification (chapter 7), the maximum force was estimated using the non-magnetic ergometer itself, by increasing the pressure in the cylinder until subjects could do isometric contractions for determination of MVC. This reduces total measurement overhead and simplifies handling of the volunteers. Using the same custom-built ergometer for estimation of MVC and exercise at 50 % MVC may reduce accuracy in terms of absolute MVC, while increasing precision, as systematic errors in force measurement will cancel out.

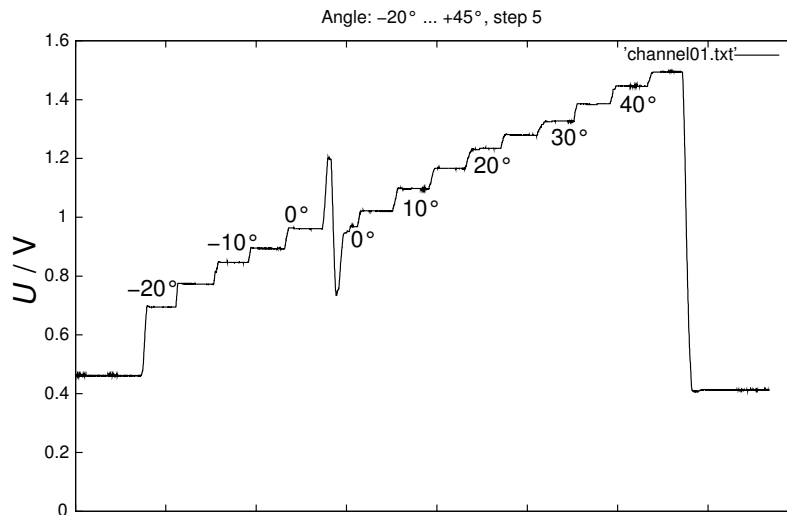


**Figure 3.7:** Calibration of the pedal’s angle sensor.

### 3. Construction of the Exercise Rig

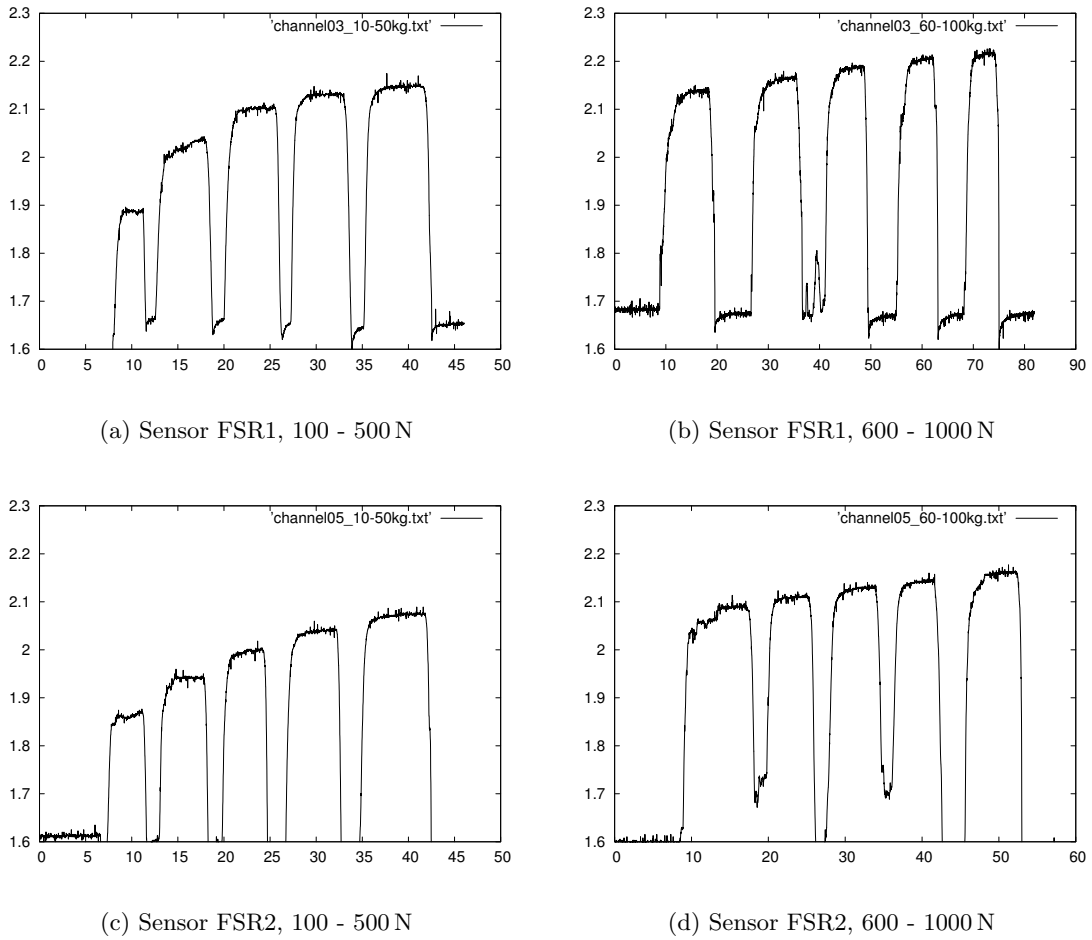


**Figure 3.8:** Calibration of the pedal's force sensors, in steps of 100 N. Sensor output signal is given in Volts.

### 3.4. Testing the Exercise Rig in Vivo

Spectra from human calf muscle were acquired with the dual interleaved  $^1\text{H}/^{31}\text{P}$  STEAM sequence described in chapter 5, to test whether the custom built ergometer can be used for calf muscle exercise (aerobic, at this stage of development) causing PCr depletion and accumulation of  $\text{P}_i$  in the NMR magnet during acquisition, without producing disturbing artifacts in  $^1\text{H}$  or  $^{31}\text{P}$  spectra, as shown in Fig. 3.9.

The spectral quality is indeed sufficient to clearly identify  $\text{P}_i$  and PCr in  $^{31}\text{P}$  spectra and creatine (Cr), choline (TMA) and EMCL/IMCL in  $^1\text{H}$  spectra at rest and during exercise. No visible artifacts caused by the pneumatic exercise rig, its moving parts, sensors or cabling deteriorate the signals. In  $^{31}\text{P}$  spectra substantial PCr/ $\text{P}_i$  changes, as expected during exercise, can be observed (Fig. 3.9) which demonstrates that the

### 3. Construction of the Exercise Rig

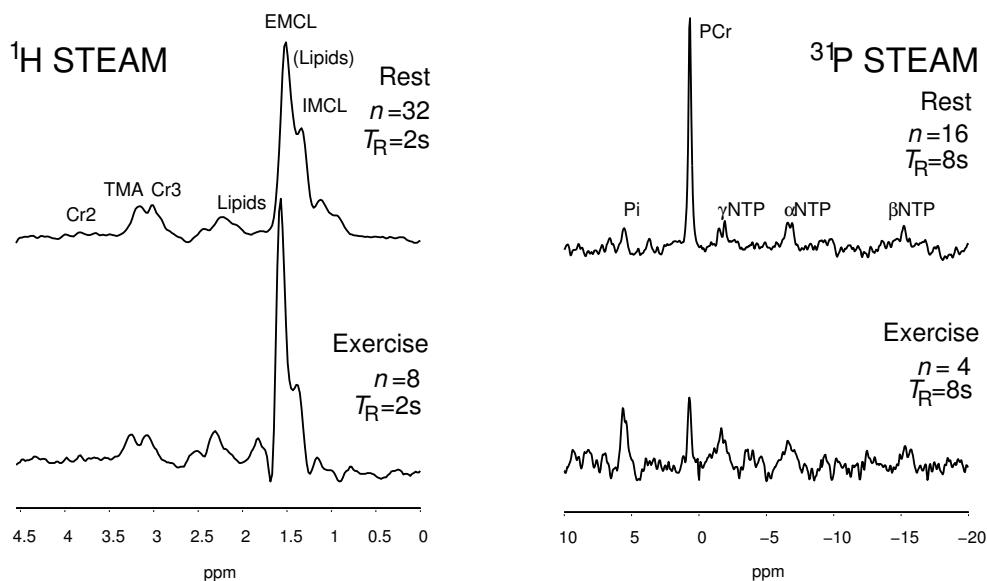


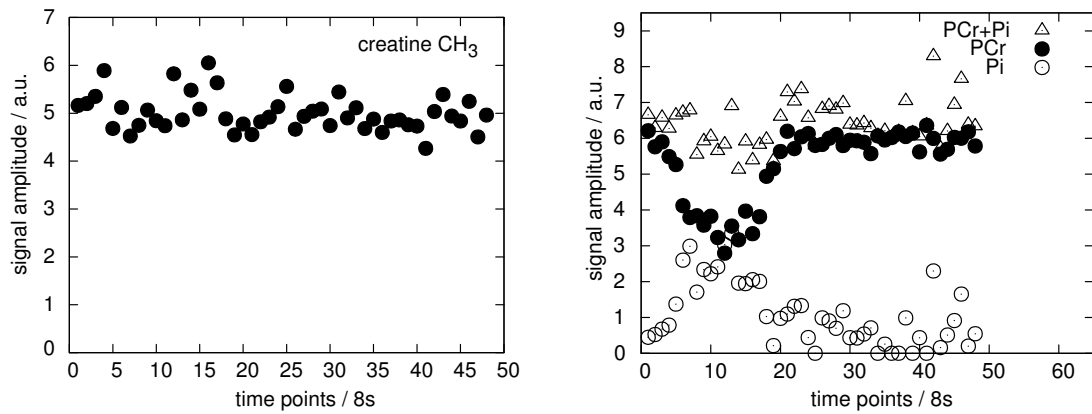
**Figure 3.9:** Localised  $^1\text{H}$  and  $^{31}\text{P}$  spectra of human m. gastrocnemius acquired at rest and after plantar flexion exercise using the custom built ergometer.  $T_R = 2\text{ s}$  for  $^1\text{H}$  spectra (left) and  $T_R = 8\text{ s}$  for  $^{31}\text{P}$  spectra (right). Both  $T_E = 8\text{ ms}$ ,  $T_M = 30\text{ ms}$ ,  $BW = 2500\text{ Hz}$ , 1024 data points (zero filled to 8k). The  $^1\text{H}$  VOI was  $1.7\text{ cm}^2$  and the  $^{31}\text{P}$  VOI was  $34\text{ cm}^2$  to partly compensate for the 15 times lower sensitivity of  $^{31}\text{P}$  vs.  $^1\text{H}$ .

apparatus is suitable as an ergometer for calf muscle exercise in a 3 Tesla magnet.

Fig. 3.10 shows an example of a dynamic exercise time series. In  $^1\text{H}$  spectra (a), the Cr3 peak and in  $^{31}\text{P}$  spectra (b) the sum of PCr and  $\text{P}_i$  was used as a reference to check for motion during rest, exercise and recovery. Peak areas showed variations as low as  $1.7 \pm 0.6\%$  for Cr3 and  $2 \pm 0.6\%$  for PCr+ $\text{P}_i$  (given as standard errors) during the measurements. These numbers are the average over the subjects ( $n = 4$ ) studied.

The next chapter is dedicated to basic MR spectroscopy of skeletal muscle in vivo, with and without localisation techniques, the question of temporal resolution versus SNR and specificity versus sensitivity.

### 3. Construction of the Exercise Rig



(a) Creatine signal in  $^1\text{H}$  STEAM spectra vs. time

(b) PCr,  $\text{P}_i$  and their sum in  $^{31}\text{P}$  STEAM spectra vs. time

**Figure 3.10:** CH<sub>3</sub> peak of Cr in  $^1\text{H}$  spectra (a) and the sum of PCr and  $\text{P}_i$  in  $^{31}\text{P}$  spectra (b) during rest, exercise and recovery. Peaks were quantified using AMARES. Average variation of these parameters was 2% and 1.7%, (SEM) respectively. Each time point corresponds to 8 s, i.e. total measurement time was 6.4 min.

# 4

## Basic $^1\text{H}$ and $^{31}\text{P}$ MRS in Resting Human Calf Muscle

Basic concepts of MRS (non-localised and localised spectroscopy) are illustrated with example spectra measured in human skeletal muscle in vivo. The influence of repetition time on spectral appearance is discussed.

### 4.1. Introduction

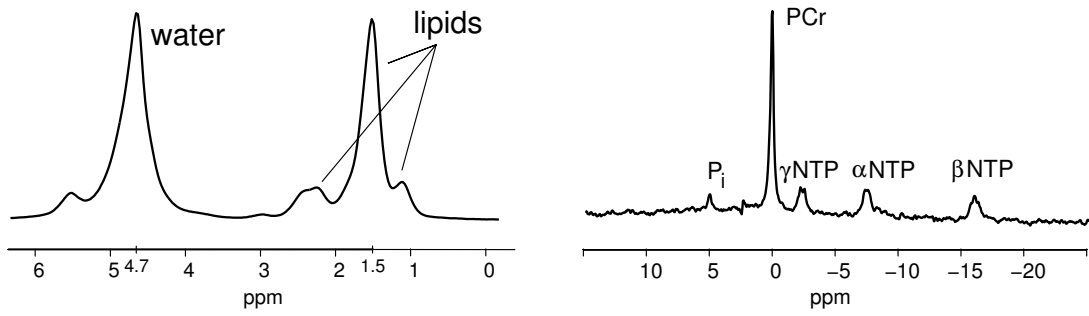
#### 4.1.1. Non-localised Spectroscopy

##### 4.1.1.1. Proton Spectroscopy

Nuclear magnetic resonance spectra acquired in a pulse-acquire scheme (often called a “one pulse” experiment) without applying any localisation technique except the spatial distribution of the coil used for RF transmission and/or reception usually benefit from a higher signal to noise ratio (SNR) than localised spectra, of course provided that relevant acquisition parameters are equal, for example repetition time ( $T_R$ ), echo time ( $T_E$ ) if applicable, pulse angle and number of averages.

Proton spectra acquired in vivo without localisation are only usable in very few cases, because water suppression is almost impossible to achieve and lipid signals, mainly from subcutaneous bulk fat dominate the spectrum, apart from the resonance of water. In the non-localised  $^1\text{H}$  spectrum in Fig. 4.1 (a), acquired from human forearm, only resonances of water and the  $\text{CH}_n$  groups of lipids can be distinguished and the peaks are very broad, with FWHM  $\sim 30$  Hz. Such spectra may be used for quantifying total water and fat content of tissue, but if a surface coil is used for excitation, the spatial distribution of pulse angles introduces a spatial weighting and e.g. fat content may be overestimated manifold by the dominant contribution of subcutaneous fat.

#### 4. Basic $^1\text{H}$ and $^{31}\text{P}$ MRS in Resting Human Calf Muscle



(a)  $^1\text{H}$  pulse-acquire spectrum,  $T_R = 1$  s, 2 averages. FWHM is ca. 30 Hz, no line broadening was applied in post processing.

(b)  $^{31}\text{P}$  pulse-acquire spectrum,  $T_R = 6$  s, 32 averages. FWHM of PCr is 17 Hz after 8 Hz exponential line broadening.

**Figure 4.1:**  $^1\text{H}$  pulse-acquire spectrum of human forearm (a). Due to the lack of water suppression and strong lipid signals, mainly from subcutaneous fat, only water and fat are visible.  $^{31}\text{P}$  pulse-acquire spectrum of human forearm (b). Note that the base line in the non-localised  $^{31}\text{P}$  spectrum is not as well-defined (i.e. flat) as in localised spectra, for example as shown in Fig.4.3.

##### 4.1.1.2. Phosphorus Spectroscopy

The situation is obviously better for non-localised  $^{31}\text{P}$  spectroscopy and it has become a clinical tool for monitoring metabolism long before  $^1\text{H}$  spectroscopy was established for in vivo use.

In the  $^{31}\text{P}$  spectrum shown in Fig. 4.1 (b), also acquired in human forearm, metabolites which are subject to change under exercise and in pathology (PCr,  $\text{P}_i$ , ATP and also PME and PDE when the number of excitations is increased) are quantifiable and have a high signal to noise ratio with relatively few averaged signal accumulations (32 in this case), compared to single voxel spectra shown in section 4.1.2.

The spectrum in Fig. 4.1 (b) still represents an accumulation of signal from a large volume, defined by the RF profile of the coil. Typically, several muscles and subcutaneous tissue contribute to the spectrum. Note that the base line is not as flat and well-defined as in the localised spectrum in section 4.1.2, but exhibits a hump which has to be subtracted or modelled as a separate spectral contribution when quantifying non-localised  $^{31}\text{P}$  spectra.

##### 4.1.2. Localised (STEAM) Spectroscopy

The main advantages of localised spectroscopy are the increased specificity in terms of definition of a volume of interest (VOI) and, in  $^1\text{H}$  MRS, the feasibility of water suppression.

The price to be paid for increased specificity is lower signal to noise. On the one hand, peak area is proportional to the number of contributing spins and, therefore,

#### 4. Basic $^1\text{H}$ and $^{31}\text{P}$ MRS in Resting Human Calf Muscle

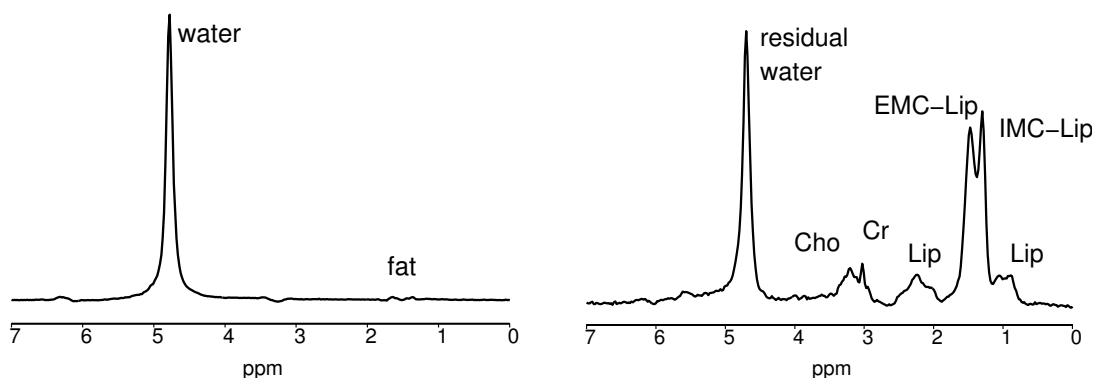
the volume of interest. On the other hand, a localisation sequence may destroy a fraction of the available magnetisation due to its intrinsic properties (see chapter 2, particularly eq. 2.4 which shows that in STEAM only half of the magnetisation is available for generating the stimulated echo signal).

Due to the smaller volume contributing to the signal, the shim, i.e. the homogeneity of  $B_0$  in a voxel, is improved, line width is reduced and the loss in SNR (which can be defined as peak height over standard deviation of spectral noise) is not necessarily indirectly proportional to the reduction of VOI [72].

Lower SNR can be compensated by accumulating signal. This in turn reduces temporal resolution by a factor of  $\Delta\text{SNR}^2$ , as in-phase signals accumulate linearly, while incoherent noise accumulates proportional to the square root of the number of averages.

##### 4.1.2.1. Single Voxel Proton Spectroscopy

As a consequence of the definition of a VOI, the contamination by dominating lipid resonances is reduced to the fraction which corresponds to the lipid content of the tissue under investigation, see Fig. 4.2 (a). In localised spectra with water suppression, metabolites like IMCL, EMCL, creatine, choline (TMA) and others can be quantified – depending on spectral resolution, orientation effects caused by residual dipolar coupling and signal to noise ratio. With dedicated NMR pulse sequences for lipid suppression, steps can be taken towards lactate detection and quantification.



(a) STEAM localised  $^1\text{H}$  muscle spectrum, without water suppression.  $T_E = 7.5$  ms,  $T_R = 2$  s, voxel size =  $2 \times 2 \times 2$  cm $^3$ , 4 averages.

(b) STEAM localised  $^1\text{H}$  muscle spectrum, with water suppression.  $T_E = 7.5$  ms,  $T_R = 2$  s, voxel size =  $1.5 \times 1.2 \times 1.5$  cm $^3$ , 36 averages.

**Figure 4.2:** Localised  $^1\text{H}$  STEAM single voxel spectra of human gastrocnemius muscle without (a) and with (b) water suppression.  $T_E = 7.5$  ms. The ordinates' scales differ by a factor of several thousands.

#### 4.1.2.2. Single Voxel Phosphorus Spectroscopy

Applying single voxel spectroscopy sequences like STEAM to the  $^{31}\text{P}$  nucleus also results in smaller line width (see Fig. 4.3) and better base line definition (compare to Fig. 4.1 (b)). The increased specificity is at the cost of reduced SNR which can be compensated by signal accumulation. This in turn reduces time resolution, and a compromise has to be found for the particular application. If only PCr and  $\text{P}_i$  have to be measured with high time resolution in an exercise study, SNR of ATP, PME and PDE is of minor interest and can be increased by accumulating sub-samples of spectra during post processing, i.e. by averaging temporal blocks.

### 4.2. Longitudinal Relaxation and Repetition Time

#### 4.2.1. Why (Not) To Use Short Repetition Times

The intrinsic signal to noise ratio of a pulse-acquire (or “one pulse”) experiment without localisation is far higher than for localised spectroscopy, e.g. using STEAM. This intrinsically high SNR allows to sacrifice signal-to-noise for the benefit of higher temporal resolution by shortening repetition times or even the acquisition of spectra in a single acquisition step without averaging.

Decreased SNR per unit time ( $\text{SNR}/t$ ) is not the only effect of shortening  $T_R$  to values comparable or even lower than  $T_1$  of the metabolites.  $\text{SNR}/t$  is optimum at  $1.27 T_1$  if  $90^\circ$  pulses are applied. This is the case for STEAM (in the volume of interest, at least) but not necessarily for pulse-acquire experiments using a surface coil where pulses are preferably adjusted to the Ernst-angle within the VOI. Short repetition times do also introduce the need to correct for saturation effects in absolute quantification and even relative quantification using peak ratios because the metabolites'  $T_1$ s differ significantly [73].

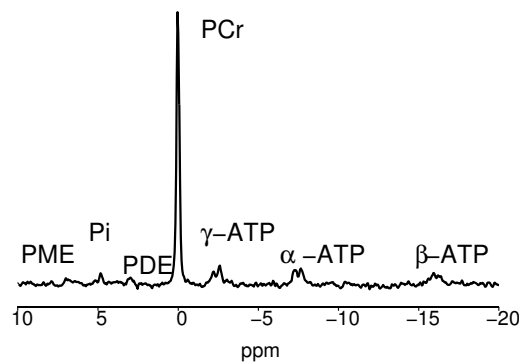


**Figure 4.3:**  $^{31}\text{P}$  STEAM spectrum of human calf muscle.  $T_E = 7.5$  ms,  $T_R = 8$  s, voxel size =  $4.3 \times 2 \times 5$  cm $^3$ , 96 averages.

### 4.2.2. A Short Repetition Time Experiment

The effect of altered spectral appearance by varying  $T_R$  can be clearly seen in the appearance of the “one pulse” spectra, acquired in human calf muscle with varying  $T_R$  as shown in Fig. 4.4.

The peak areas of  $\text{P}_i$  and  $\text{NTP}^*$  in the data of Fig. 4.4 are shown as a function of  $T_R$  in Fig 4.5, normalised to the  $\text{PCr}$  signal. The spectra were quantified using AMARES [74] in the jMRUI [75] spectral data processing package. Most strikingly, the  $\text{NTP}$  resonances become more prominent, the shorter  $T_R$  is chosen.

### 4.2.3. Discussion

Choosing  $T_R$  below the optimum value of  $1.27 T_1$  of the metabolite of main interest can make sense in terms of SNR per unit time if either SNR is not critical for this particular metabolite anyway (which may be the case for  $\text{PCr}$ , a metabolite with long  $T_1$  and high abundance in skeletal muscle) or if a high temporal resolution is vitally important for the experiment so that SNR per unit time may be sacrificed.

---

\* Nucleoside tri-phosphates ( $\text{NTP}$ ) is a more accurate denotation of the “ATP” peaks in a  $^{31}\text{P}$  spectrum, as other nucleoside phosphates give rise to resonances at the same spectral position, however, adenosine triphosphate prevails

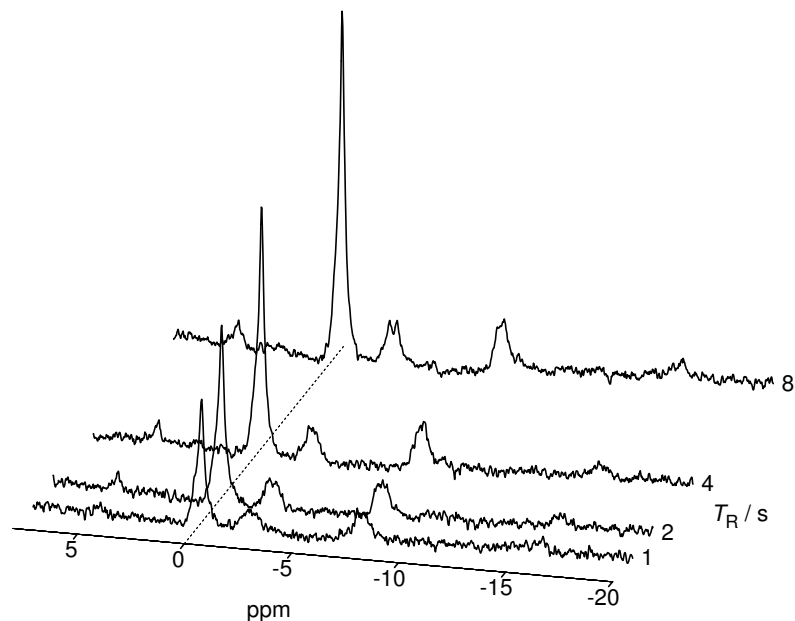


**Figure 4.4:** A series of simple “one pulse” experiments with varying repetition times illustrates the effect of  $T_R$  on spectral appearance. Note the strong increase of the  $\text{PCr}$  peak with increasing  $T_R$ , whereas  $\text{ATP}$  is much less affected due to its faster  $T_1$  relaxation.

#### 4. Basic $^1\text{H}$ and $^{31}\text{P}$ MRS in Resting Human Calf Muscle

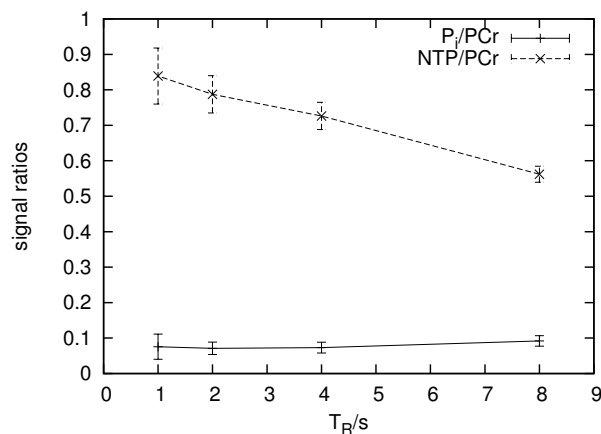


**Figure 4.5:** Relative peak areas of  $P_i$  and  $NTP$  as fraction of  $PCr$  and scaled to their values at  $T_R = 8$  s.

Moreover, the parameter  $T_1$  of  $PCr$  and  $\gamma$ - $ATP$  obtained from a progressive saturation experiment, is not the "true" or intrinsic longitudinal relaxation time  $T_1$ , as these metabolites undergo chemical exchange. It rather represents an "apparent"  $T_1$  relaxation time [76, 77, 78], and there has been discussion whether this fact impedes the use of monoexponential functions to correct for saturation or whether chemical exchange effects can be neglected [79, 79].

# 5 Dual Interleaved $^1\text{H}/^{31}\text{P}$ STEAM MRS

Before the double quantum filter NMR sequence for lactate detection was developed and later incorporated into a triple multi-nuclear interleaved acquisition scheme, a dual interleaved STEAM sequence was implemented for acquisition of localised  $^1\text{H}$  and  $^{31}\text{P}$  spectra.

## 5.1. Introduction

As the name implies, “NMR” is a resonance phenomenon, and nuclei with distinct resonance frequencies can be excited simultaneously without mutual interference. The resonance frequencies of  $^1\text{H}$  and  $^{31}\text{P}$  differ by a factor of 2.47 (125.63 MHz vs. 50.58 MHz when  $B_0 = 3\text{ T}$ ),  $^1\text{H}$  and  $^{31}\text{P}$  spectra can, in principle, be acquired simultaneously (disregarding hetero-nuclear coupling effects) and spectra may be acquired synchronously, if hardware permits. Interleaving multi-nuclear acquisitions is a more versatile approach than simultaneous acquisition of NMR spectra or images, because  $B_0$  gradients used in a sequence always act on both nuclei synchronously and simultaneous experiments are no longer strictly independent as soon as  $B_0$  gradients are employed. Moreover, acquiring multi-nuclear NMR spectra or images simultaneously, requires the scanner’s hard- and software to be capable to use two receive and transmit channels simultaneously, while for interleaved acquisition, rapid switching of the channels is sufficient if exact synchronisation and time keeping is warranted. The Bruker Medspec whole body system, as installed at the MR Centre of Excellence, Vienna Medical University, is equipped with two RF transmit channels and one RF receive channel which can be switched between reference frequencies.

The term “interleaved”, as it is used here, means nesting  $^1\text{H}$  and  $^{31}\text{P}$  MRS experiments in such a way that excitation and acquisition of one nucleus’ spectra is accomplished during the recovery period,  $T_R$ , of the other.

## 5. Dual Interleaved $^1\text{H}/^{31}\text{P}$ STEAM MRS

In contrast to previous studies [80, 56, 81, 19] which mainly used surface coils and no further localisation techniques, an interleaved STEAM sequence was developed to acquire  $^1\text{H}$  and  $^{31}\text{P}$  gradient-localised spectra in one experiment. In vivo experiments showed, that this has the further benefit of NOE enhancement of the  $^{31}\text{P}$  spectra [82]. The main advantage of localised versus non-localised spectroscopy is its increased specificity: the signal originates from a distinct region of interest only, e.g. an exercising muscle, excluding surrounding tissue which may be activated to a lesser extent or even not at all. In addition, the feasibility of dynamic interleaved localised  $^1\text{H}$  and  $^{31}\text{P}$  spectroscopy during plantar flexion exercise is demonstrated using the custom built pneumatic system for muscle activation described in chapter 3.

### 5.2. Methods

#### 5.2.1. Sequence Design

##### 5.2.1.1. Implementation of the Interleaved STEAM Experiment

The MultiScanControl (MSC) Tool (Bruker Biospin, Ettlingen, Germany) was used as framework to develop a pulse sequence for interleaved acquisition of  $^1\text{H}$ - and  $^{31}\text{P}$  spectra with STEAM localisation for both nuclei. The MSC-Tool (its base window is shown in Fig. 5.1) handles initialisation, setup and deriving of parameters for multiple experiments, starts the experiment and directs the data flow to separate scan directories. The scripts which define the exact operations necessary to merge two or more experiments, which are then executed by MSC, have to be written by the developer

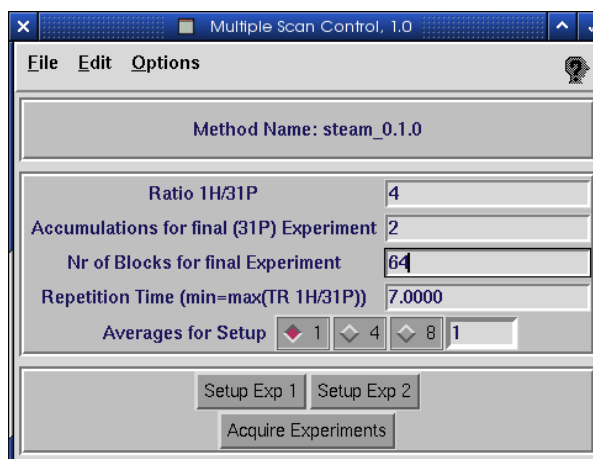


**Figure 5.1:** Base window of the Multiple Scan Control Tool tailored for a dual interleaved  $^1\text{H}$  and  $^{31}\text{P}$  STEAM experiment with a configurable ratio of acquisitions on the two respective RF channels (which is useful due to the differing  $T_1$  relaxation times). Parameters chosen here would result in 64  $^{31}\text{P}$  STEAM spectra with 2 accumulations per spectrum and a repetition time of 7 s and 64  $^1\text{H}$  spectra with 8 averages and  $T_R = 1.75$  s.

## 5. Dual Interleaved $^1\text{H}/^{31}\text{P}$ STEAM MRS

who also needs to write a new pulse program containing both (or more) experiments. The STEAM VOIs can be chosen individually (with independent size, shape and position of the voxels) in the standard geometry editor, all sequence parameters can be set individually in the standard editors of the acquisition software, except the ratio of  $T_{\text{R}}\text{s}$  which is determined by the factor supplied by the operator via the field “Ratio 1H/31P” in the MSC base window (see Fig. 5.1).

The freedom to select different VOIs does not pose any restrictions (as voxels may also be set to be identical if required) and follows inherently from the necessity to rescale gradients by gyromagnetic ratios  $\gamma_{^1\text{H}}/\gamma_{^{31}\text{P}}$  in the merged pulse sequence program. This is due to the fact that the effect of  $B_0$  gradients for slice selection scales linearly with  $\gamma$ .

### 5.2.1.2. Relaxation, Repetition Times and Interleaved Experiments

In any Fourier spectroscopy experiment the signal to noise ratio per unit time ( $\text{SNR}/t$ ) can be calculated as a function of RF pulse rotation angle ( $\alpha$ ) and repetition time ( $T_{\text{R}}$ ) between consecutive acquisitions [83]. When the excitation flip angle is large, optimum SNR is obtained for  $T_{\text{R}}$  that does not allow complete  $T_1$  relaxation: Choosing  $\alpha = 90^\circ$ , as is the case in a STEAM experiment, optimum  $T_{\text{R}}$  is  $1.27 \cdot T_1$  [84]. This also applies for surface coil excitation, as the pulse angle is adjusted to  $90^\circ$  within the VOI (which is small compared to the coil’s dimensions) by seeking the maximum signal achieved with a STEAM acquisition, individually for each subject and voxel position.

Since longitudinal relaxation times of  $^{31}\text{P}$  and  $^1\text{H}$  metabolites differ significantly, the repetition time should preferably be chosen individually for each nucleus.  $T_1\text{s}$  of  $^{31}\text{P}$  metabolites are relatively long, ranging between 3 s ( $\alpha\text{-NTP}$ ) and 6 s (PCr) at 3 Tesla [73] compared to the  $T_1$  of  $^1\text{H}$  metabolites which are typically of the order of 1 s, although they can be as short as 300 ms for lipids [85]. To account for this fact, the sequence design allows the acquisition of an arbitrary number of  $^1\text{H}$  spectra between excitations on the  $^{31}\text{P}$  channel, as illustrated in Fig. 5.2.

The volumes of interest were placed in the medial head of the gastrocnemius muscle, because plantar flexion exercise with the leg extended activates primarily the gastrocnemius muscles [3, 4] and its medial head is in the centre of the magnet bore in  $y$  (patient’s left-right) direction when the calf is strapped to the exercise rig. The  $^1\text{H}$  voxel’s volume was  $2.7\text{ cm}^3$  and the  $^{31}\text{P}$  VOI was  $31.4\text{ cm}^3$  to partly compensate for the lower  $^{31}\text{P}$  sensitivity ( $^1\text{H} : ^{31}\text{P} = 1 : 6.63 \cdot 10^{-2}$ ). The  $^1\text{H}$  voxel was not chosen to be the same size as the  $^{31}\text{P}$  VOI to avoid broad  $^1\text{H}$  line widths which would render spectra unusable, but both VOIs were positioned in the same muscle, about concentrically (see Fig. 5.3) and avoiding subcutaneous fat, especially for the  $^1\text{H}$  voxel. A short echo time  $T_{\text{E}} = 7.5\text{ ms}$ ,  $T_{\text{M}} = 30\text{ ms}$ , receiver bandwidth  $BW = 2500\text{ Hz}$  and 1024 data points were chosen for both nuclei. A CHESS scheme was used for water suppression [86]. Volume selective shimming was achieved with Bruker’s implementation of FASTMAP [87], selecting a  $5 \times 5 \times 5\text{ cm}^3$  volume of interest (VOI). The time domain fit routine AMARES [74] in the jMRUI software package [75] was used to quantify phosphocreatine (PCr), inorganic phosphate ( $\text{P}_i$ ), total creatine (Cr) and pH changes.

## 5. Dual Interleaved $^1\text{H}/^{31}\text{P}$ STEAM MRS

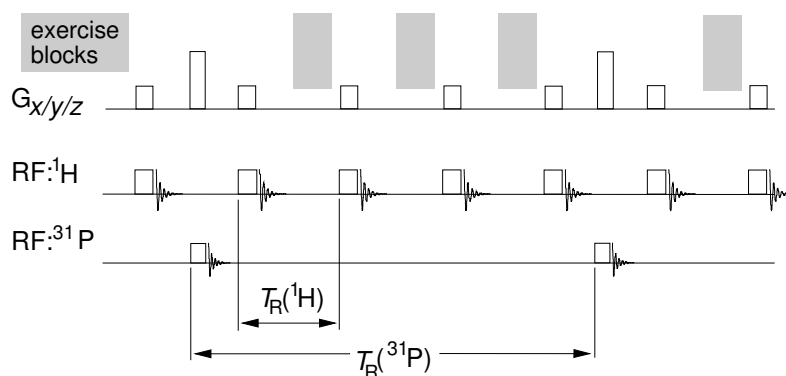


**Figure 5.2:** Schematic representation of the interleaved  $^1\text{H}$  and  $^{31}\text{P}$  STEAM sequence. An arbitrary number of  $^1\text{H}$  spectra (four in this example) can be acquired during each  $^{31}\text{P}$  acquisition  $T_R$  to optimise SNR of each spectrum despite the large differences in  $T_1$ . Outlined rectangles schematically represent RF and  $B_0$  gradient pulses, grey boxes indicate NMR inactive periods suitable for plantar flexion exercise.

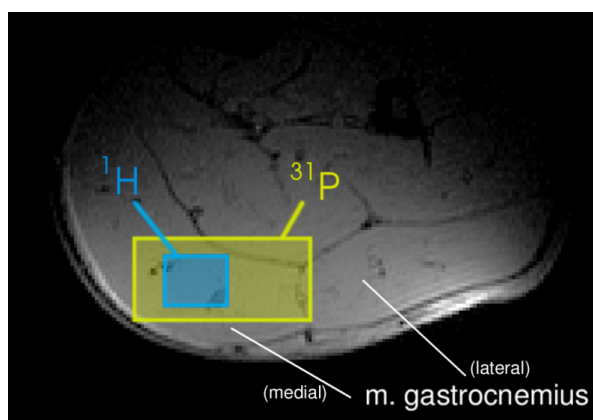


**Figure 5.3:** Typical position of the volumes of interest for interleaved STEAM spectroscopy in human medial gastrocnemius muscle.  $^1\text{H}$ :  $V = 2.7 \text{ cm}^3$ , due to the lower sensitivity of phosphorus in NMR, the  $^{31}\text{P}$  VOI's size is  $V = 43.1 \text{ cm}^3$ .

### 5.2.2. Scanner Hardware

The NMR scanner hardware used in all experiments was a 3 T Bruker Medspec S 300 DBX whole-body scanner (Bruker Biospin, Ettlingen, Germany) equipped with a whole body gradient system BG-A55) and a double-tuned surface coil ( $d = 10 \text{ cm}$ ) for RF transmission and reception, see Appendix A.2, also manufactured by Bruker.

### 5.2.3. Subjects

Seven healthy subjects (6 male, 1 female), with a mean ( $\pm$  SD) age of  $31.5 \pm 9.2$  years and a body mass index (BMI) of  $23.6 \pm 2.5$  kg/m<sup>2</sup> (mean  $\pm$  SD) were examined. Each subject's maximum test force was estimated using a Biodex Multi-Joint-System 3 Pro (Biodex Medical Systems, Inc., NY, USA) dynamometer, one week before the NMR examination. Written informed consent to the protocol, which was approved by the local ethics committee, was obtained from all subjects.

#### 5.2.3.1. Sequence Timing During Exercise

To reduce calf motion (a potential source of artifacts) during acquisition subjects were instructed to exercise only during periods without NMR signal excitation, i.e. not to push the pedal during and shortly after gradient noise. Before starting the experiment they were trained in a test run with the gradients turned on for acoustic triggering but without signal acquisition. The optimum  $T_R$  for  $^{31}\text{P}$  is 8 s. Although optimum SNR for  $^1\text{H}$  would, in principle, allow shorter repetition times,  $T_R = 2$  s leaves 1.2 s between data acquisition (taking  $t_{\text{acq}} = 409$  ms) and subsequent  $^1\text{H}$  excitation; long enough to allow plantar flexion. The most suitable number of  $^1\text{H}$  acquisitions between consecutive  $^{31}\text{P}$  acquisitions is therefore four. After 3 consecutive plantar flexions and  $^1\text{H}$  acquisitions, subjects paused once, allowing  $^{31}\text{P}$  acquisition without motion. Verbal support was given during the experiment whenever necessary.

## 5.3. Results

### 5.3.1. Test Objects

The performance of the STEAM sequence had been evaluated using a two-compartment test object [73]. Contamination of the spectra by signals originating from outside the nominal VOI was  $C = 0 \pm 2\%$  under fully relaxed conditions and  $C = 3 \pm 2\%$  for short  $T_R$ , i.e.  $T_R = 1$  s  $\ll T_1$ .

The interleaved  $^1\text{H}/^{31}\text{P}$  STEAM sequence had been tested extensively on phantom solutions to ensure that spectra acquired in interleaved experiments are equivalent to spectra acquired separately.

### 5.3.2. Resting Muscle

Proton spectra of resting human calf muscle acquired in a subgroup of  $n = 4$  subjects for in vivo evaluation of the interleaved sequence were equivalent to standard STEAM experiments, whilst SNR from  $^{31}\text{P}$  spectra was higher by a factor of  $1.34 \pm 0.06$  for PCr and  $1.06 \pm 0.13$  for  $\text{P}_i$  due to NOE (see Fig. 5.4).

**Voxel sizes for  $^1\text{H}$  and  $^{31}\text{P}$  spectroscopy:** The proposition that  $^1\text{H}$  spectra should be acquired with smaller voxel sizes than  $^{31}\text{P}$  spectra due to line width- vs.-SNR considerations was tested in one subject.

## 5. Dual Interleaved $^1\text{H}/^{31}\text{P}$ STEAM MRS

Spectra from a small  $^1\text{H}$  voxel with  $14 \times 12 \times 15 \text{ mm}^3 = 2.52 \text{ cm}^3$  and a large  $^{31}\text{P}$  voxel with  $40 \times 14 \times 50 \text{ mm}^3 = 45 \text{ cm}^3$  were compared to spectra from equal VOIs for both nuclei with an intermediate VOI of  $18 \times 14 \times 20 \text{ mm}^3 = 5.04 \text{ cm}^3$ .

The line width, measured as full width at half maximum (FWHM) of the Cr  $\text{CH}_3$  peak in the  $^1\text{H}$  spectrum was decreased from 13 Hz to 9 Hz when shrinking the  $^1\text{H}$  voxel from  $5.04 \text{ cm}^3$  to  $2.52 \text{ cm}^3$ . The FWHM of PCr in  $^{31}\text{P}$  spectra increased only from 8.5 Hz to 10 Hz when increasing the  $^{31}\text{P}$  voxel to the larger VOI size, but SNR increased from 7.6 to 51 with 8 averages for both acquisitions.

### 5.3.3. Exercising Muscle

Typical  $^1\text{H}$  and  $^{31}\text{P}$  in vivo spectra of exercising muscle are shown in Fig. 5.5. After a baseline period of 2 minutes at rest, plantar flexion was executed for 6.5 min at 50% MVC (adjusted individually for each subject via air pressure in the reservoir tank) followed by 15 min of recovery. The repetition time was 2 s for  $^1\text{H}$  spectra (Fig. 5.5 (a)) and  $T_R = 8 \text{ s}$  for  $^{31}\text{P}$  spectra (Fig. 5.5 (b)).

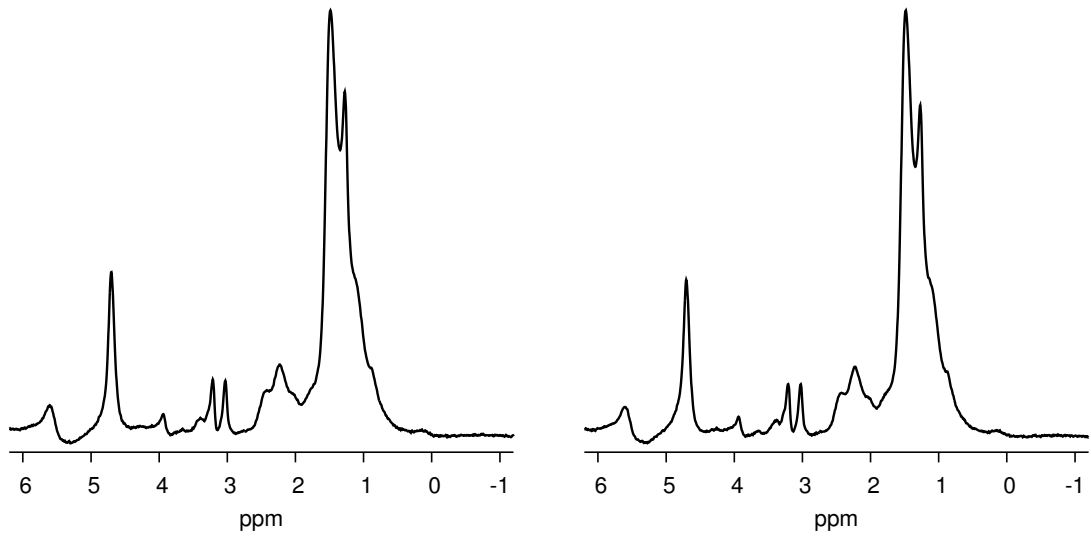
Spectral quality is sufficient to clearly identify peaks of creatine (Cr), choline (TMA) and EMCL/IMCL from  $^1\text{H}$  spectra and  $\text{P}_i$  and PCr from  $^{31}\text{P}$  spectra. Changes in the EMCL signal in some subjects can be attributed to motion, as tissue with higher EMCL concentration may contaminate the VOI at the onset of exercise despite fixation of the calf and foot and confinement of acquisition to periods without motion. The variation of the Cr  $\text{CH}_3$  peak area during rest, exercise and recovery, given as standard error, was low as 1.7%. In  $^{31}\text{P}$  spectra substantial PCr/ $\text{P}_i$  changes, as expected during exercise, can be observed without perceptible deterioration of signals, e.g. by motion or artifacts caused by the pneumatic exercise rig (Figs. 5.5 and 5.6). Similar to the total creatine signal in  $^1\text{H}$  spectra, the variation of the sum of PCr and  $\text{P}_i$  signals was only 2% during the measurement, which indicates that motion did not affect spectral quality. This exercise setup produced a mean ( $\pm$ SD) pH decrease from  $7.12 \pm 0.11$  to  $6.94 \pm 0.19$  and a mean relative PCr depletion of  $63 \pm 18\%$  after 6.5 min of exercise at 50% MVC ( $n = 4$ ).

Whilst 6.5 min of moderate exercise is not expected to deplete IMCL or alter total creatine concentration, the insert in Fig. 5.5 shows a drop in peak amplitude of the  $\text{CH}_2$  signal of Cr alone during exercise and its recovery post exercise, which can not be fully explained by variations in line width.

## 5.4. Discussion

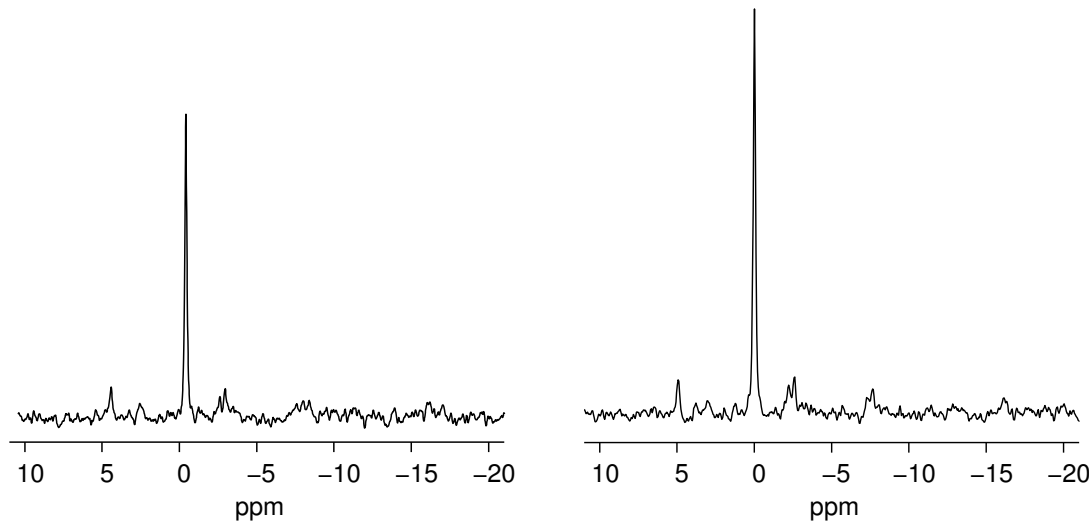
Interleaved MRS experiments have been used to investigate metabolism in muscle tissue [80, 56, 81] with surface coils and have been demonstrated with a combination of TEM and surface coils for  $^1\text{H}$ ,  $^1\text{H}\text{-}\{^{13}\text{C}\}$ ,  $^{31}\text{P}$  STEAM and ISIS NMR spectroscopy in the human brain [51, 52]. In this chapter, a method for interleaved acquisition of  $^1\text{H}$  and  $^{31}\text{P}$  NMR spectra with STEAM localisation for both nuclei using a dual tuned surface coil is presented along with its application to human calf muscle during plantar flexion exercise in a 3 Tesla whole-body MR system. STEAM was chosen because it

## 5. Dual Interleaved $^1\text{H}/^{31}\text{P}$ STEAM MRS



(a)  $^1\text{H}$  spectrum, single acquisition. VOI =  $6.7\text{ cm}^3$ ,  $T_R = 2\text{ s}$ , 64 averages

(b)  $^1\text{H}$  spectrum, interleaved acquisition. VOI =  $6.7\text{ cm}^3$ ,  $T_R = 2\text{ s}$ , 64 averages



(c)  $^{31}\text{P}$  spectrum, single acquisition PCr SNR = 53. VOI =  $62\text{ cm}^3$ ,  $T_R = 8\text{ s}$ , 16 averages

(d)  $^{31}\text{P}$  spectrum, interleaved acquisition, PCr SNR = 71. VOI =  $62\text{ cm}^3$ ,  $T_R = 8\text{ s}$ , 16 averages

**Figure 5.4:** Comparison of single and dual acquisition of  $^1\text{H}$  and  $^{31}\text{P}$  STEAM spectra in resting human gastrocnemius muscle. The measurement time per spectrum was 2 min 8 s for each spectrum. (Both interleaved spectra were acquired within the same 2 min 8 s measurement time). Note the increased signal-to-noise ratio in  $^{31}\text{P}$  spectra in interleaved acquisition of SNR = 71 for PCr (d), compared to standard (single) acquisition of SNR = 53 (c).  $^1\text{H}$  spectra are virtually identical.

## 5. Dual Interleaved $^1\text{H}/^{31}\text{P}$ STEAM MRS

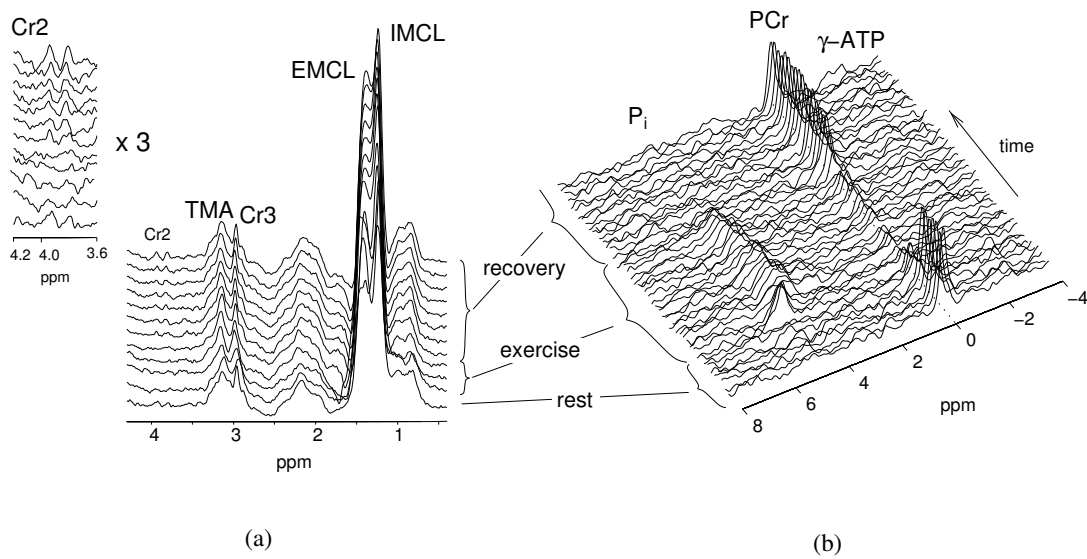


**Figure 5.5:**  $^1\text{H}$  (left) and  $^{31}\text{P}$  (right) STEAM spectra from human gastrocnemius muscle acquired in interleaved mode during rest, exercise and recovery.  $^1\text{H}$  spectra (a) were acquired with  $T_E = 7.5$  ms,  $T_R = 2$  s,  $\text{VOI} = 2.7$  ml, and averaged to blocks of 64 for display ( $2'08''$  per spectrum). The insert shows a magnification ( $\times 3$ ) of the Cr2 resonance around 4.0 ppm.  $^{31}\text{P}$  spectra (b) were acquired with  $T_E = 7.5$  ms,  $T_R = 8$  s,  $\text{VOI} = 31.4$  ml, 2 avgs, yielding a time resolution of 16 s. The relative PCr change was 74 %,  $\text{pH}_{\text{rest}} = 7.1$ ,  $\text{pH}_{\text{ex}} = 6.7$ . (Only the first 50 of 96  $^{31}\text{P}$  spectra are shown, for clarity).

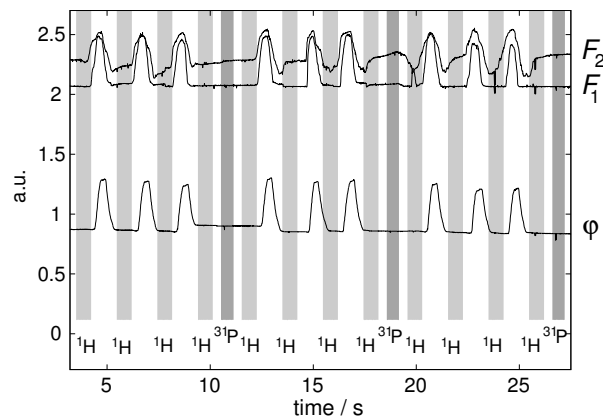


**Figure 5.6:** Pedal angle and force ( $F_1$ ,  $F_2$ : output of two strain sensors located on the pedal, next to the subject's ball of the foot) recorded during an interleaved  $^1\text{H}/^{31}\text{P}$  spectroscopy experiment. Grey bars indicate periods between the first RF pulse and the end of acquisition of the STEAM sequence, as recorded via the NMR scanner's trigger output. (Dark grey:  $^{31}\text{P}$ , light grey:  $^1\text{H}$ ) Note that there is no motion during acquisitions in this example.

## 5. Dual Interleaved $^1\text{H}/^{31}\text{P}$ STEAM MRS

is a robust single shot sequence that performs better with the surface coil than e.g. PRESS, especially when large voxels are used for  $^{31}\text{P}$  spectroscopy (which has also been verified on test objects [88]).

Localised spectroscopy has the advantage of increased specificity compared to non-localised measurements. The signal originates only from the region of interest, i.e. one can focus on the muscle which exercises most and exclude surrounding tissue which may be activated to a lesser degree (adjacent muscles) or not at all (skin, fat- or connective tissue). SNR is lower as a consequence of smaller tissue volume contributing to the signal. STEAM localised  $^{31}\text{P}$  VOIs were typically  $30 - 40 \text{ cm}^3$ , while the sensitive volume of a 10 cm surface coil is a hemisphere with a volume of ca.  $260 \text{ cm}^3$ , significantly larger than the STEAM VOI. On the other hand, line width and shape, baseline and spectral resolution of multiplets is clearly better in localised spectroscopy.

Note that  $^{31}\text{P}$  spectra were acquired with long  $T_R = 8 \text{ s}$  here, to achieve optimum SNR for PCr and  $\text{P}_i$  the metabolites of major interest during exercise. The intensity of metabolite signals with shorter  $T_1$ s (NTP) is therefore reduced compared to short  $T_R$  measurements, where in fact PCr and  $\text{P}_i$  are partially saturated and need strong corrections for  $T_1$  relaxation.

**Voxel sizes for  $^1\text{H}$  and  $^{31}\text{P}$  spectroscopy:** Small VOIs are favourable in MRS because line width can generally be reduced by decreasing voxel sizes [72]. This is particularly important for  $^1\text{H}$  spectra of muscle tissue [89], which are characterised by orientation-dependent splitting of resonances [33].

A line width of 13 Hz in  $^1\text{H}$  spectra may prevent quantification of spectra, as peaks (e.g. EMCL/IMCL) can not be distinguished clearly, which have been separated with  $\text{FWHM} = 9 \text{ Hz}$ . The increase of SNR in  $^{31}\text{P}$  spectra by a factor of 6.4 corresponds to a gain in measurement time of a factor of 40, if compensated by averaging. Therefore, a large  $^{31}\text{P}$  VOI, that may still be well within the muscle or muscle group of interest is obviously desirable, if not a prerequisite in time resolved localised  $^{31}\text{P}$  spectroscopy.

Characteristic line splitting may become less clear in the accumulation of signal from regions with locally different fibre orientation in a large voxel, as fibre orientation is mostly, but not completely uniform across a muscle. See e.g. Fig. 7b in [69], the distribution of spectral patterns for m. gastrocnemius medialis. Water suppression is also less efficient for large VOIs, due to the inhomogeneous  $B_1$ -field of surface coils.

In  $^{31}\text{P}$  MR spectroscopy SNR is inherently lower, and a big voxel ( $\gtrsim 30 \text{ cm}^3$ ), covering a large fraction of the exercising muscle under investigation seems more appropriate. Studies mapping  $T_2$  of exercising muscle revealed that recruitment does not differ significantly across a single muscle [90]. We can therefore justifiably assume that our interleaved measurements of  $^1\text{H}$  and  $^{31}\text{P}$  metabolites are representative of the whole medial gastrocnemius muscle. Contributions from adjacent muscles, known to be recruited to a highly different extent during exercise [90, 3, 4] can still be largely excluded from the VOI due to the efficient suppression of contamination [73] of the  $^{31}\text{P}$  STEAM sequence.

## 5. Dual Interleaved $^1\text{H}/^{31}\text{P}$ STEAM MRS

If improved time resolution is desired, repetition times may be reduced, with the proviso that exercise be confined to periods without NMR signal excitation or acquisition to minimise motion. Moreover, for metabolites with long  $T_1$  at 3 T, such as PCr [73], this decreases SNR per unit time and may introduce complications in quantification due to  $T_1$  weighting and chemical exchange [77] for other metabolites.

**NOE Enhancement of  $^{31}\text{P}$  Spectra in Interleaved Experiments:** The quality of  $^1\text{H}$  spectra acquired in interleaved mode here is equivalent to single mode experiments, while the corresponding  $^{31}\text{P}$  spectra benefit from higher SNR compared to standard acquisition due to Nuclear Overhauser effect (NOE).

The extent of NOE enhancement depends on RF power irradiation and is usually accomplished by saturating the water resonance using CW or WALTZ [91,92]. In the experiment described here, the NOE is induced by the RF pulses of the  $^1\text{H}$  STEAM sequence which is interleaved with  $^{31}\text{P}$  STEAM acquisitions. Since neither  $^1\text{H}$  pulse amplitude nor duty cycle were maximised to achieve  $^1\text{H}$  saturation, but  $^1\text{H}$  RF pulse power was optimised for  $^1\text{H}$  STEAM signal amplitude and water suppression, the observed NOE is not the maximum achievable. NOE enhancements between 43% (NTP) and 64% (PCr) in calf muscle have been reported in a 1.5 T study [91]. In brain, 25-30% enhancement was achieved for PCr at 1.5 and 7 T [93,92],  $\text{P}_i$  signal was increased by 15.7% in this 7 T study. These results match our non-optimised NOE enhancement factors. Including e.g. a WALTZ scheme for increasing NOE would be feasible, albeit at the cost of  $^1\text{H}$  SNR due to saturation of water and adjacent resonances, depending on saturation bandwidth, but is beyond the scope of this work.

Longitudinal relaxation times of PCr and  $\text{P}_i$ , in human calf muscle are  $6.4 \pm 0.2$  s and  $5.2 \pm 1.0$  s [73], resulting in saturation factors of 0.71 and 0.78, respectively, for  $T_R = 8$  s. This partly compensates the different NOE factors from 1.34 and 1.06 to correction factors of 0.96 and 0.83, neglecting any chemical exchange effects.

**$^1\text{H}$  STEAM spectra during exercise:** Whilst substantial changes in PCr/ $\text{P}_i$  are observed in  $^{31}\text{P}$  spectra, the concentration of metabolites in  $^1\text{H}$  spectra (creatine methyl resonance (Cr3), TMA, IMCL) are not expected to change significantly during 6.5 minutes of exercise with 50% MVC. Intramyocellular lipid depletion in muscle becomes measurable with  $^1\text{H}$  MRS after prolonged sub-maximal exercise, e.g. running for several hours [27,28]. Similar to findings in isometric exercise of tibialis anterior muscle under ischemia [41], a drop in peak amplitude of the methylene group of creatine (Cr2) during exercise and its recovery post exercise can be observed in  $^1\text{H}$  spectra in this work (see insert in Fig. 5.5), which can not be fully explained by increased line width during exercise.

During strenuous exercise protocols – and also sporadically at lower exercise intensities in some subjects – a resonance attributed to acetyl carnitine (AcCt) [94] was described in  $^1\text{H}$  spectra of human muscle. Interleaved acquisition of  $^1\text{H}$  and  $^{31}\text{P}$  spectra can, in principle, be used to simultaneously acquire time courses of AcCt and high energy phosphates during a high workload exercise protocol.

## 5.5. Conclusion

In summary, in this chapter the feasibility and quality of time-resolved localised  $^1\text{H}$  and  $^{31}\text{P}$  spectroscopy of exercising skeletal muscle in a single interleaved experiment at 3 T was demonstrated. The benefits of this approach are reduced total measurement time and NOE enhancement of  $^{31}\text{P}$  spectra. Most significantly it opens the possibility of studying the dynamics of metabolism with multi nuclear MRS in a single run, e.g. examining PCr depletion and resynthesis with  $^{31}\text{P}$  MRS and the concomitant time course of the Cr2 resonance in  $^1\text{H}$  spectra. The method has been tested to be feasible and reproducible when applied to human calf muscle during exercise on a custom-built pneumatic ergometer and shown to be effective.

# 6

## Double Quantum Filter Sequence for Lactate Detection

The DQF NMR protocol was tested on phantom solutions and meat specimens during sequence development, to obtain optimum lactate signal amplitude and lipid suppression while minimising contamination and artifacts.

Although he did not believe that lactate would be quantifiable during exercise, he paved the way. Thank you, Vlado!

### 6.1. Introduction

The principle of a double quantum filter (DQF) for selectively detecting lactate in skeletal muscle [57, 35, 36, 67] is described in section 2.3. In muscle tissue, strong lipid signals (between 1 and 2% of the water signal's amplitude, which corresponds to several hundred to thousand millimoles per litre) overlap the resonance of lactate which is expected to vary in concentration between zero in resting muscle and approximately 20 mmol/l after ischaemic exercise. It is therefore vitally important to take care that the lactate signal is free from lipid contamination to enable proper quantification of lactate. The lactate doublet is moreover subject to orientation dependent intensity modulations due to residual dipolar coupling in an anisotropic tissue, e.g. muscle fibres, which was previously described as “reduced lactate visibility” in muscle tissue [55].

## 6.2. Sequence Design

### 6.2.1. The RF Pulses

The full pulse sequence diagram is given in Fig. 6.1. The pulse shapes used are sinc3 pulses, defined by the function  $\sin(x)/x$  for the non-frequency-selective  $90^\circ$ - and  $180^\circ$ -pulses used for spatial slice selection. The  $90^\circ$ -pulse creating the double quantum coherences is a non-frequency-selective block pulse (i.e. rectangular shape), followed by a frequency-selective  $90^\circ$  Gaussian pulse on the frequency of the lactate CH resonance at 4.11 ppm which converts DQC back into SQC.

The last pulse does not cause modulations of the DQF signal if its frequency has an offset relative to the frequency of reference and was therefore chosen to be slice selective in  $y$  (vertical, A-P) direction, because patients can be easily moved along the  $x$  and  $z$  axis by either shifting left/right on the patient bed or moving the bed itself into or out of the magnet bore. Pulse powers were adjusted without volume selection, using a birdcage coil and a spherical test object ( $V \sim 2$  l) and rescaled to the surface coil and in vivo situation using the known relations for the RF gain attenuators (logarithmic scale,  $-6$  dB  $\hat{=}$   $+100\%$  pulse power).

#### 6.2.1.1. Water Suppression and Fat Inversion

The DQF sequence is preceded either by a CHESS water suppression module comprising three Gaussian pulses [86], as shown here, or the first CHESS pulse can be replaced by an adiabatic inversion pulse with an inversion recovery time of  $T_{1R} = 208$  ms which further reduces lipid resonances to support the double quantum filter's fat suppression. The principle of lipid suppression by pre-inversion is based on the fact that  $T_1$  of lipids is far shorter ( $T_1 = 300$  ms) than other resonances'  $T_1$  and the lipid's magnetisation crosses zero 208 ms after inversion (see section 2.3).

#### 6.2.1.2. The $\tau'$ Delay

The DQF sequence which is suggested e.g. in de Graaf's textbook on in vivo NMR spectroscopy [57] and by Asllani et al. [35, 36] comprises a  $180^\circ$  pulse in the  $\tau'$  delay. The use of  $180^\circ$  pulses introduces a source of error by imperfect pulse power calibration in any real world experimental setup and especially when using surface coils with inhomogeneous  $B_1$  fields in vivo. Refocussing magnetisation by a  $180^\circ$  pulse in the delay  $\tau'$  between two  $90^\circ$  pulses of different duration (as is the case here) also requires to increase  $\tau'$ .

The DQF sequence was therefore implemented without a  $180^\circ$  pulse in the  $\tau'$  delay, as suggested by Jouvencal et al. [67] and Asllani et al. [35]. A schematic representation of the pulse sequence was given in Fig. 2.3, for the full sequence diagram, see in Fig. 6.1. The delay  $\tau'$  was varied in a phantom experiment to verify experimentally whether the effect of omitting this  $180^\circ$  pulse is restricted to a frequency dependent phase modulation, as implied in [36] or eventually results in a modulation of signal amplitude by the term  $\cos(\omega_I + \omega_S)$  with the frequencies  $\omega_I$  and  $\omega_S$  relative to the frame of reference.

## 6. Double Quantum Filter Sequence for Lactate Detection

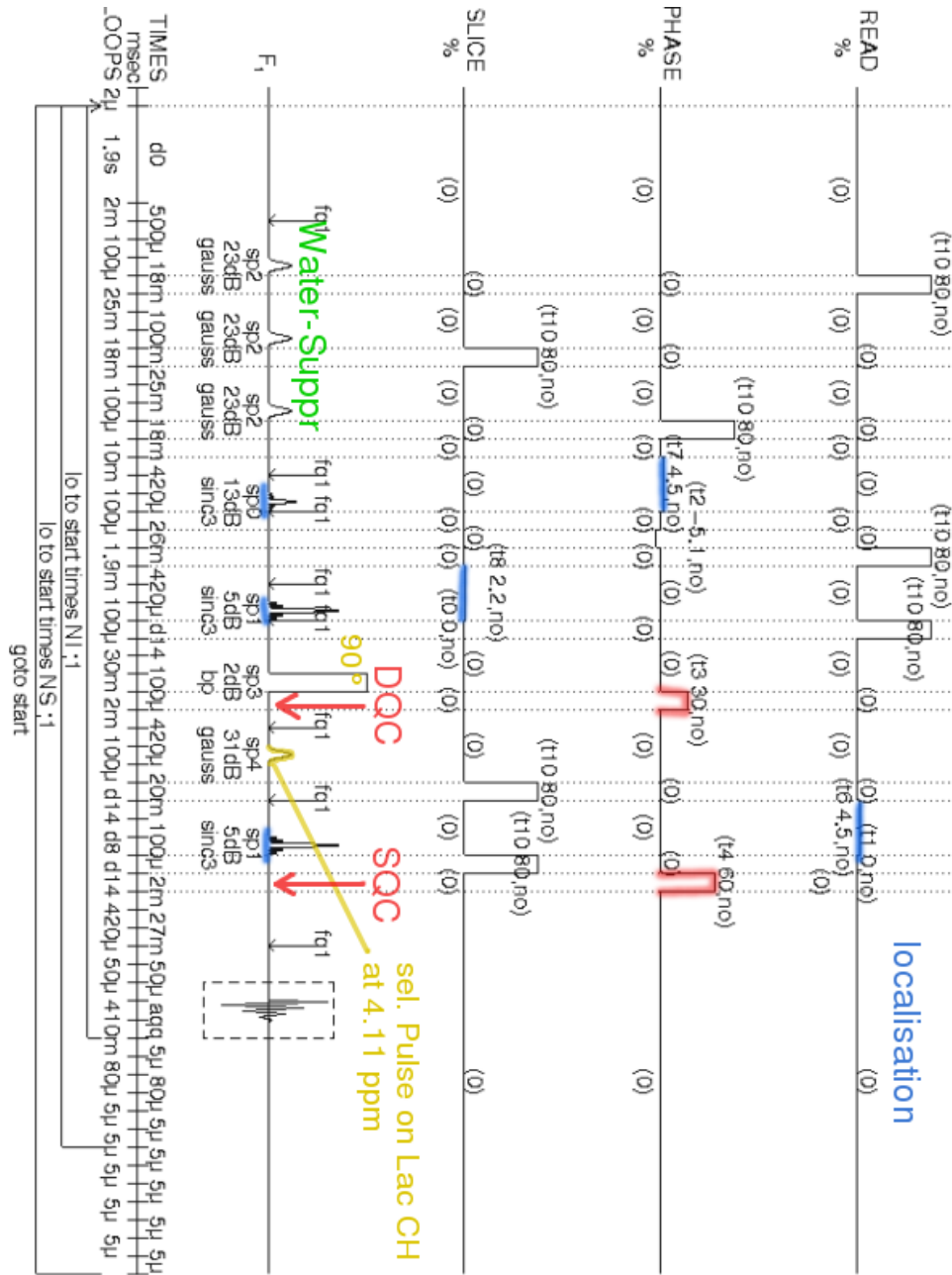


**Figure 6.1:** Double quantum filter (DQF) pulse sequence for lactate detection in muscle. “READ”, “PHASE” and “SLICE” denote the spatial directions (a convention originating from  $k$ -space sampling concepts in NMR imaging) along which the  $B_0$  field gradients take effect. “ $F_1$ ” denotes RF channel 1. At the time points marked “SQC” and “DQC” (arrows), the magnetisation of the lactate  $IS_3$  system is in single- or double quantum state, respectively, and is “filtered” by the gradients “t3” and “t4”. The DQF sequence, as shown here, is preceded by a CHES water suppression module comprising three Gaussian pulses. An additional adiabatic inversion for further lipid suppression can be switched on.

### 6.3. Phantom Studies

In order to test the DQF performance on isotropic solutions, several experiments were conducted with phantoms filled with lactate solution, “brain soup” and a mixture of lactate and lipid emulsion.

The DQF signal intensity is theoretically 50 % compared to the signal of a PRESS sequence with the same echo time (135 ms in a solution), because only the fraction of magnetisation which is in double quantum state (i.e. 50 %) during the first DQF gradient contributes to the signal. Initial measurements on a spherical test object containing 2l of 20 mmol/l lactate solution showed that the effective signal yield using localised DQF with a voxel size of  $2 \times 1.2 \times 2 \text{ cm}^3$  in combination with the surface coil was  $43.4 \pm 0.7 \%$  compared to PRESS with  $T_E = 135 \text{ ms}$ . This result shows that the DQF experiment is feasible using the surface coil for RF excitation and reception.

#### 6.3.1. The Effect of $\tau'$ Without a Refocussing Pulse

##### 6.3.1.1. Experimental Setup

A spherical phantom ( $V = 300 \text{ ml}$ ) was filled with 100 mmol/l lithium lactate ( $T_1 = 1.22 \pm 0.08 \text{ s}$ ,  $T_2 = 660 \pm 110 \text{ ms}$ , measured via saturation recovery by varying  $T_R$  and  $T_E$  in a STEAM experiment, respectively) placed on the double tuned surface coil ( $\varnothing = 10 \text{ cm}$ ) which was also used in all ex vivo and in vivo experiments.

##### 6.3.1.2. Fitting Spectra

Spectra were processed using the AMARES [74] time domain fit routine, as incorporated in the jMRUI software package [75], (<http://www.mrui.uab.es/mrui/>). Only “soft constraints” (i.e. defining extremal values for the parameter to be fitted) were applied to the frequencies of the two lactate peaks, and the “first order overall phase” was fixed to zero. The “zero order phase” was estimated by AMARES.

##### 6.3.1.3. Results

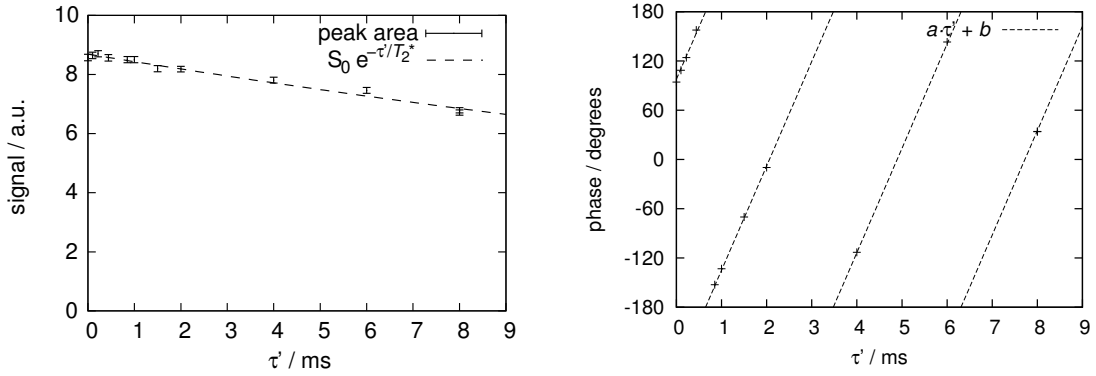
Here it is shown that no intensity modulation occurs when  $\tau'$  is varied (Fig. 6.2), the signal amplitude only decays with  $T_2^*$  relaxation, i.e.  $T_2^* = 33.6 \pm 1.5 \text{ ms}$  (fitted using the implementation of the nonlinear least-squares (NLLS) Marquardt-Levenberg algorithm of the free software gnuplot [95]).

#### 6.3.2. Calibration for Quantification of Absolute Concentration

##### 6.3.2.1. Preparation of Lactate Solution

For preparing the lactate solutions, lithium lactate, ( $\text{C}_3\text{H}_5\text{LiO}_3$ ,  $m_r = 96,01 \text{ g/mol}$ ,  $\geq 97 \%$  pure, by Sigma Aldrich GmbH, Steinheim, Germany) was dissolved in water, and successively diluted from highest to lowest concentration.

## 6. Double Quantum Filter Sequence for Lactate Detection



(a) DQF lactate CH<sub>3</sub> signal amplitude.  $S_0 = 8.69 \pm 0.04$  (a.u.),  $T_2 = 33.6 \pm 1.5$  ms,  $\sqrt{\chi^2} = 0.1$ .

(b) Phase of the DQF lactate CH<sub>3</sub> signal.  $a = 127.2 \pm 0.2$ ,  $b = 87.9 \pm 0.9$ ,  $\sqrt{\chi^2} = 2.3$ .

**Figure 6.2:** Lactate signal intensity (a) and phase (b) in spectra acquired with the DQF sequence as function of  $\tau'$ . (100 mmol/l lactate solution.) Peak intensities and phases were fitted using AMARES. No periodic modulation of peak amplitude is visible (a) while the phase depends linearly on  $\tau'$  (b). Acquisition parameters: 8 averages,  $T_R = 10$  s,  $T_E = 135$  ms, voxel size =  $18 \times 12 \times 20$  mm<sup>3</sup>.

### 6.3.2.2. Results

The calibration curve for the signal of the DQF sequence as function of lactate concentration between 10 and 50 mmol/l in solution is shown in Fig. 6.3. For each concentration,  $T_2$  was estimated by varying  $T_E$  of a STEAM sequence and selecting the echo times where  $J$  evolution refocusses the signal ( $T_E = 7.48, 270, 545$  and  $830$  ms), see Tab. 6.1. For  $C = 50$  mmol/l,  $T_E$  was varied in small steps to follow the signal modulation of the lactate  $IS_3$  spin system for STEAM with varying  $T_E$ , (see Fig. 6.4). The sin/cos modulation of  $S(T_E)$  is not modelled in the fit function, as spectral quantification was done by peak area integration, dropping phase information (i.e. Fig. 6.4 does not show any negative data points).  $T_1$  of the solutions was measured

**Table 6.1:**  $T_1$  and  $T_2$  relaxation times of lactate solutions of different concentrations.

[Lac] / mmol/l	$T_1$ / s	$T_2$ / ms
100	$1.22 \pm 0.08$	$660 \pm 110$
50	n. m.	$609 \pm 10$
25	n. m.	$496 \pm 21$
15	$1.22 \pm 0.09$	$438 \pm 20$
10	n. m.	$330 \pm 18$

## 6. Double Quantum Filter Sequence for Lactate Detection

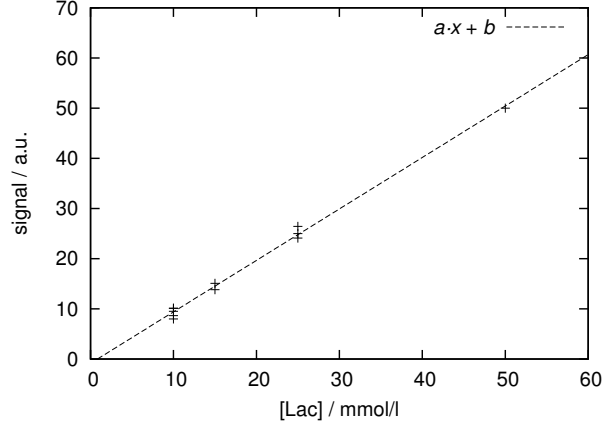


**Figure 6.3:** Signal of the DQF sequence as function of lactate concentration in solution.  $a = 1.025 \pm 0.024$ ,  $b = -0.8 \pm 0.5$ ,  $\sqrt{\chi^2} = 0.933$ .

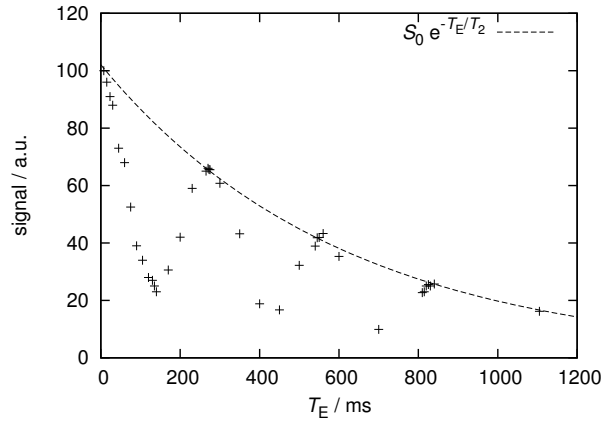


**Figure 6.4:**  $T_2$  fit curve for lactate in solution ( $C = 50$  mmol/l)

for  $[\text{Lac}] = 100$  mmol/l and 15 mmol/l and showed no concentration dependent variation:  $T_1 = 1.22 \pm 0.09$  s (see Tab. 6.1). The regression curve in Fig. 6.3 was fitted using gnuplot [95]. The fit yielded the parameters  $a = 1.025 \pm 0.024$ ,  $b = -0.8 \pm 0.5$ ,  $\sqrt{\chi^2} = 0.933$ . ( $\chi^2$  is the sum of the squared differences or 'residuals' (SSR)).

### 6.3.2.3. Conclusion

The excellent match between lactate concentration in solution in the range of 10 – 50 mmol/l and of the relaxation-corrected data points indicates that lactate solution can be used as a quantification reference and concentrations can be interpolated between zero and 50 mmol/l, when lactate concentrations are measured with the localised DQF MRS sequence in vivo and in meat specimens ex vivo, after application of back-calculation factors discussed later.

### 6.3.3. Test Object Containing Brain Metabolites (“Brain Soup”)

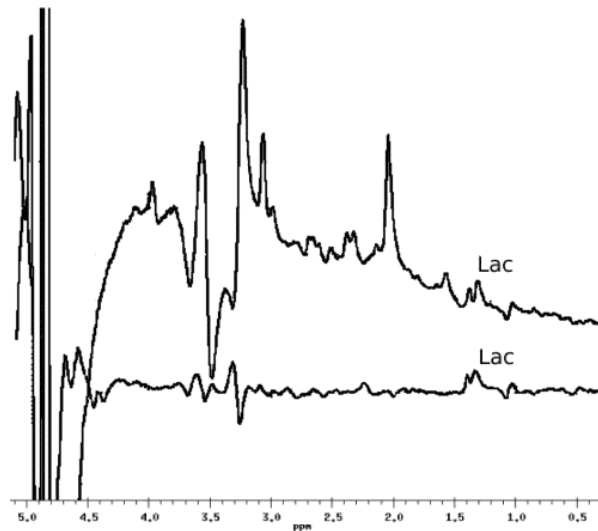
A spherical test object ( $V \approx 21$ ) containing an aqueous solution of metabolites typically measured in human brain (i.e. creatine, choline, N-acetyl-aspartate, glutamine, glutamate and others) and lactate was used to test the performance of the double quantum filter sequence with respect to suppression of resonances at frequencies other than the lactate  $\text{CH}_3$ 's 1.3 ppm. (Such a phantom is colloquially called “brain soup”.)

Fig. 6.5 shows two spectra acquired with and without the double quantum filter, with otherwise comparable pulse sequence parameters. The upper spectrum, acquired with a PRESS sequence with  $T_E = 135$  ms shows the typical pattern of brain metabolites in solution, similar to in vivo brain. In the lower spectrum, acquired with the DQF sequence (also  $\tau_1 + \tau_2 = T_E = 135$  ms), only lactate is visible. For RF excitation and reception, the dual tuned 10 cm surface coil was used.

### 6.3.4. Test Object Containing Lipid and Lactate

Another test object was made of lipid emulsion, 5 % (Intralipid, Fresenius Kabi, Graz, Austria), lithium lactate, 20 mmol/l (Sigma-Aldrich, Steinheim, Germany) and potassium phosphate, 20 mmol/l (Sigma-Aldrich, Vienna, Austria) to verify the suppression of lipids and detection of lactate by the DQF sequence.

In Fig. 6.6, the spectra acquired with  $^{31}\text{P}$  STEAM ( $12\text{ cm}^3$ ),  $^1\text{H}$  STEAM ( $8\text{ cm}^3$ ) and localised DQF ( $8\text{ cm}^3$ ) are shown. STEAM spectra were acquired with short echo times (7.4 ms), the DQF spectrum with  $T_E = 135$  ms. For all spectra,  $T_R$  was 4 s with 16 averages.



**Figure 6.5:** PRESS spectrum (top) and localised DQF spectrum (bottom), both acquired with  $T_E = 135$  ms. Resonances other than lactate are suppressed by the double quantum filter. Note also the improved base line in the in the DQF spectrum.

## 6. Double Quantum Filter Sequence for Lactate Detection

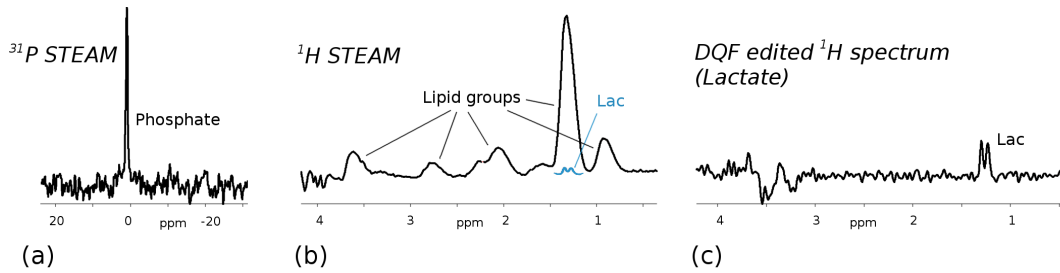


**Figure 6.6:**  $^{31}\text{P}$  STEAM (a),  $^1\text{H}$  STEAM (b) and DQF (c) Spectra from a solution of lipid, lactate and phosphate. For sequence parameters, see text. The lactate doublet is only visible in the double quantum filtered spectra, where lipid signals are virtually perfectly suppressed (c). The artifact between 3 and 4 ppm in the DQF spectrum is caused by the RF pulse that selectively inverts the coupling partner of the lactate  $\text{CH}_3$  resonance. Spectra were acquired in a single interleaved experiment, see chapter 7.

### 6.4. Measurements on Meat Specimens

In order to validate the double quantum filter NMR sequence for detecting lactate in muscle tissue, test measurements have been performed on several specimens of porcine and bovine meat. The aim was to verify the echo time- and orientation dependence of the DQF signal as simulated in section 2.3.3.

#### 6.4.1. Variation of Echo Time

##### 6.4.1.1. Specimen

A specimen of porcine meat ( $m = 0.8\text{ kg}$ ) was placed on top of the double tuned ( $^1\text{H}$ ,  $^{31}\text{P}$ ) surface coil with approximately parallel orientation of fibres relative to  $\vec{B}_0$ . STEAM and localised DQF spectra were acquired.

##### 6.4.1.2. Results

The short echo time ( $T_E = 7.4\text{ ms}$ ) STEAM spectrum (Fig. 6.7) of a porcine meat specimen shows EMCL and IMCL at 1.5 and 1.3 ppm, but no lactate is visible, although it is abundantly present in meat specimens *ex vivo*. Lactate is masked by the strong lipid signals. The same applies to STEAM and PRESS spectra (not shown) with long  $T_E$  in muscle tissue. When lipids are suppressed by the double quantum filter, lactate finally becomes visible, see Fig. 6.8. Here, echo times are varied ( $T_E = 135, 44.6$  and  $36.6\text{ ms}$ ), and the signal increases manifold for shorter echo times. SNR increases from about 2.5 over 4.6 to 6.7, when shortening the echo time, as indicated.

##### 6.4.1.3. Discussion

The 2.7-fold gain in SNR when applying short echo times is an enormous improvement. It means that *in vivo* measurements, which suffer from low SNR, typically starting

## 6. Double Quantum Filter Sequence for Lactate Detection

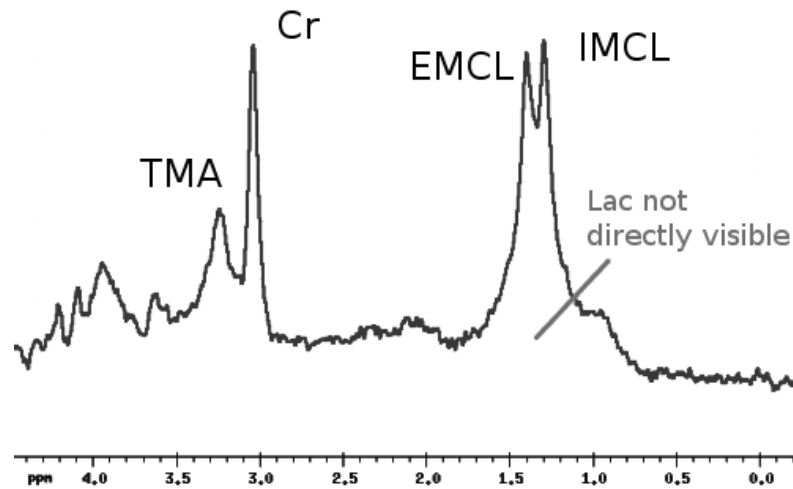


**Figure 6.7:** The STEAM ( $T_E = 7.4$  ms) spectrum of a porcine meat specimen shows EMCL and IMCL at 1.5 and 1.3 ppm, but no lactate is visible, although abundantly present in meat specimens *ex vivo*, due to the overlapping lipid signals. The resonances at 3.0 and 3.25 ppm are labeled “Cr” and “TMA”, as these metabolites have their respective peaks here, in *in vivo* NMR spectra.

below the threshold of detection may become possible. Indeed, as a fetch-ahead to chapter 7, DFQ spectroscopy experiments performed during this study using long  $T_E$  (135 ms) yielded disputable results in the best case, in most cases only noise. Employing short echo times only makes *in vivo* detection and quantification of lactate during and after ischaemic exercise possible.

### 6.4.2. Variation of Angle Between Fibre Orientation and Magnetic Field

#### 6.4.2.1. Specimen

Fresh porcine meat, similar in size and shape to the specimen of bovine meat shown in Fig. 6.9, approximately 1 kg, (readily available in Austria as “Schweinenuss”) was chosen, due to its relatively low fat content of 2% (which was found to be a realistic estimate, in  $^1\text{H}$  spectra without water suppression) and, mainly, because of its almost round shape and visible striation on the surface. Spherical objects are preferable for use in MRS because of better shimming behaviour and, therefore, narrower lines achievable, compared to more irregularly shaped objects. A meat specimen of  $m \approx 1$  kg fits well onto the surface coil and allows matching and tuning to optimal values, similar to the *in vivo* situation when measuring human calf muscle.

## 6. Double Quantum Filter Sequence for Lactate Detection

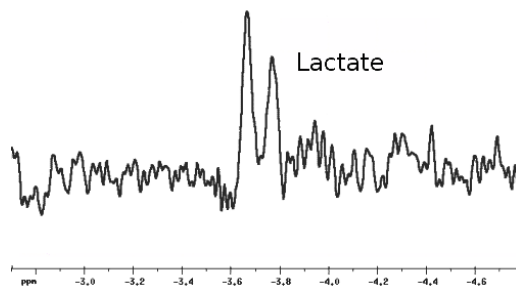
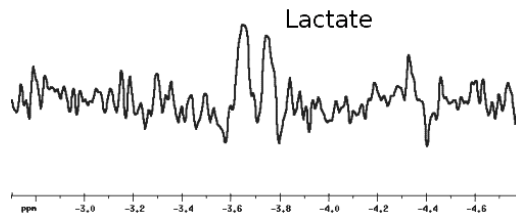
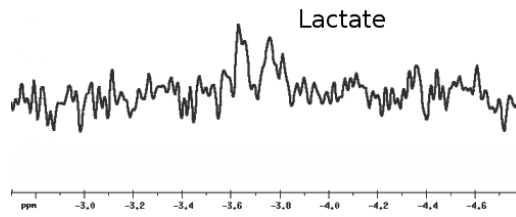


**Figure 6.8:** DQF spectra of porcine meat specimen, visible striation oriented parallel to  $\vec{B}_0$ , with varying echo times. Note the 2.7-fold increase of Signal (and SNR) for short  $T_E$ .

### 6.4.2.2. Results

Double quantum filtered spectra acquired from the meat specimen described are shown in Fig. 6.10. Measurements were done at two angles relative to the main magnetic field, an orientation- and echo time dependence is visible.

### 6.4.2.3. Discussion

The effect of changing orientation is not quite as clearly visible in Fig. 6.10, as one might expect from the numerical simulations described in section 2.3.3, Figs. 2.5, 2.6 and 2.7 or observed when varying echo time, as demonstrated in in Fig. 6.8. At least

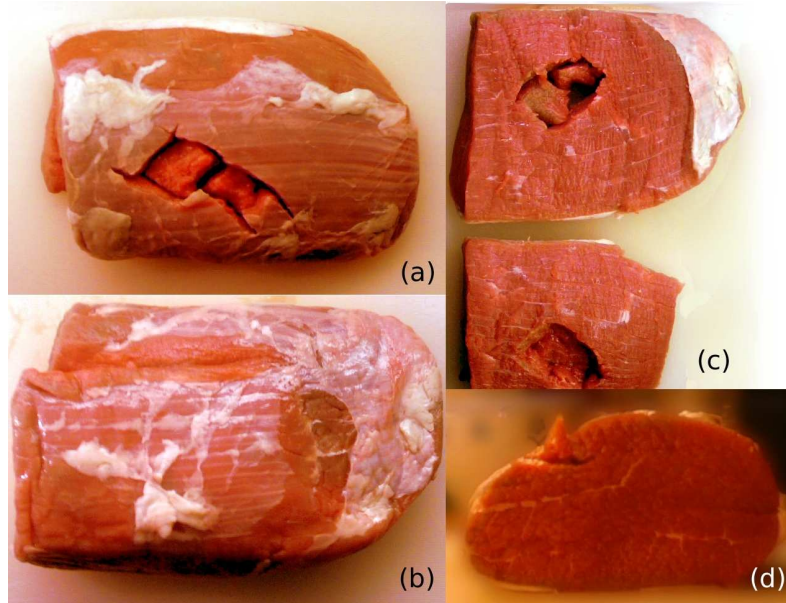


**Figure 6.9:** Bovine meat specimen. Note that superficial striation (a, b) is not necessarily parallel to gross fibre orientation at the centre (c) and may be further altered by positioning the pliable specimen in the shallow pit of the surface coil. The hole (a, c) was cut after NMR spectroscopy, although this particular specimen was not assayed biochemically. The low bulk fat content of the specimen can be seen in (c) and (d).

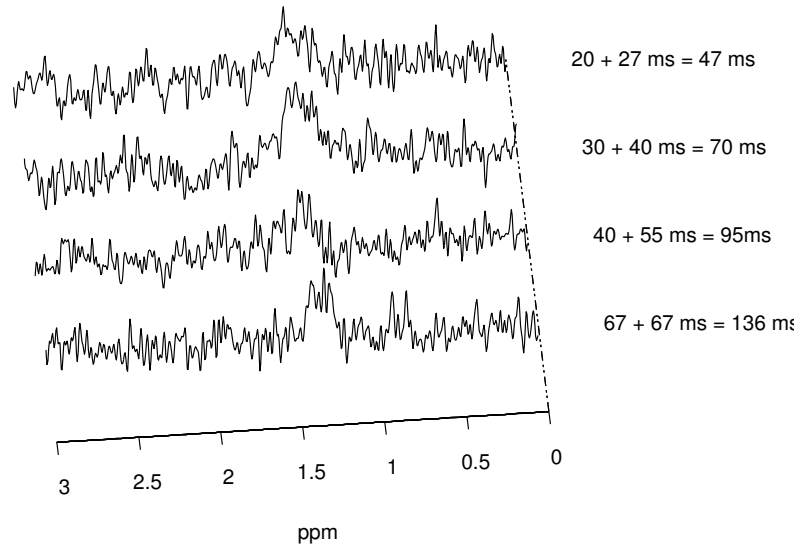
a pronounced maximum at short echo times is not visible in Fig. 6.10 (a), as observed experimentally in Fig. 6.8. This may be due to the unpredictable and heterogeneous fibre orientation in the meat. The porcine meat (no photograph available) had more heterogeneous fibre orientations than the beef shown in Fig. 6.9.

### 6.4.3. Conclusion

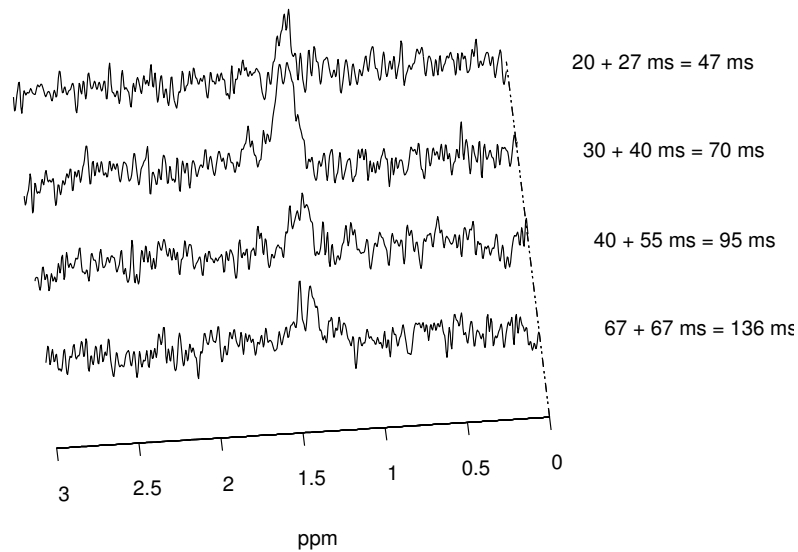
The measurements on phantom solutions and meat specimens showed that the DQF sequence is capable of suppressing unwanted lipid resonances while yielding lactate signal as expected from numerical simulations in section 2.3.3. Selecting and positioning a suitable meat specimen turned out to be more challenging than expected, most likely due to the uncertainty of fibre orientation inside a meat specimen.

The experiments confirm the reasoning in chapter 2.3.3, according to which a shorter echo time than  $T_E = 135$  ms, the optimum for lactate detection in isotropic media, is preferable. Care has to be taken, however, to choose the best compromise between maximising signal under optimum conditions by choosing extremely short echo times, e.g.  $(\tau_1, \tau_2) = (10 \text{ ms}, 20 \text{ ms})$ , and finding a robust set of parameters for realistic conditions, when fibre orientation can not be determined precisely but has to be assumed within a range of uncertainty. The compromise chosen for in vivo measurements in chapter 7 was  $(\tau_1, \tau_2) = (25 \text{ ms}, 32 \text{ ms})$ .

## 6. Double Quantum Filter Sequence for Lactate Detection

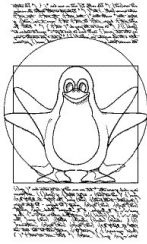


(a) The meat specimen is oriented as parallel to  $\vec{B}_0$  as possible by estimating fibre orientation without cutting into the meat before the NMR measurement. (Line width and SNR was not sufficient to measure the frequency splitting of the multiplets.)



(b) Orientation of the meat specimen has been altered by  $45^\circ$  relative to (a). The splitting of the lactate peak is  $\Delta f \approx 8 \pm 2$  Hz in accordance with the numerical simulation in Fig. 2.6.

**Figure 6.10:** DQF spectra of a meat specimen shown in Fig. 6.9 at two orientations, varying echo time  $T_E = \tau_1 + \tau_2$ . A clear maximum is visible in (b) at  $T_E = 70$  ms, which is expected for fibres oriented at  $\varphi \approx 40^\circ$  relative to  $\vec{B}_0$ , according to the numerical simulations shown in section 2.3.3, Fig. 2.6. Note also the lactate peak's splitting in (b).



*la quadrature  
del cerchio.*

very loosely based on  
Leonardo da Vinci

# Triple Interleaved $^1\text{H}$ DQF/ $^{31}\text{P}$ / $^1\text{H}$ MRS

This part comprises the cumulated efforts to solve several problems in one experiment: Specificity (via localisation and DQF) and temporal resolution, to follow dynamic changes of muscle metabolism and still keeping sensitivity acceptable for absolute quantification of muscle metabolites.

## 7.1. Introduction

Phosphorus magnetic resonance spectroscopy, as a non-invasive method, has long been used to study cellular energy metabolism *in vivo*, paradigmatically in skeletal muscle. In addition to exercise science and research of muscle diseases as such, muscle function is important in ageing and chronic diseases, and its exercise response has analogies to brain activation of interest in functional neuroimaging.

While the non-invasiveness of  $^{31}\text{P}$  MRS has great advantages for the recruitment of experimental subjects (particularly clinical patients and elite athletes) and can be repeated almost unrestrictedly, the major disadvantage of  $^{31}\text{P}$  MRS compared to needle biopsy has been the inability to quantify lactate directly. This has necessitated indirect approaches [96] which have become matter of some debate [97,98] in connexion with the control of glycolysis [99] and cellular acid handling [100,96].

Several technical obstacles for quantifying lactate in muscle tissue *in vivo* have to be overcome: Overlaying lipid resonances have to be suppressed adequately, and orientation dependent ordering effects, compartmentation and relaxation lead to limited lactate visibility of only a fractional amount of the true concentration if neglected.

Here an interleaved  $^{31}\text{P}$  and  $^1\text{H}$  MRS method for monitoring lactate accumulation and the accompanying changes in phosphorus metabolites during exercise and recovery is described. Good agreement has been found between directly measured lactate and

## 7. Triple Interleaved $^1\text{H}$ DQF/ $^{31}\text{P}$ / $^1\text{H}$ MRS

that measured biochemically and inferred indirectly from  $^{31}\text{P}$  MRS data. The results advance present knowledge of muscle cellular acid-base metabolism, and open the way for much more detailed studies of the latter and the control of glycolysis.

### 7.2. Methods

#### 7.2.1. Sequence Design

The dual interleaved multi-nuclear STEAM sequence described in 5 was further extended by including a double quantum filter (DQF) for localised acquisition of lactate spectra, as it is introduced in chapter 6.

In analogy to the reasoning about long  $^{31}\text{P}$  and short  $^1\text{H}$  relaxation times detailed in section 5.2.1.2, the triple interleaved sequence comprising a localising double quantum filter for lactate detection,  $^{31}\text{P}$  and  $^1\text{H}$  STEAM, was also implemented with the feature of “asymmetric” acquisition of spectra. In this case,  $n \geq 1$  DQF lactate spectra can be acquired per  $^{31}\text{P}$  /  $^1\text{H}$  STEAM acquisition, as shown in Fig. 7.1. The full sequence diagram is shown in Fig. 7.2. Again, the dual tuned surface coil ( $\varnothing = 10$  cm) was used in connection with the 3 T Bruker Medspec (both manufactured by Bruker Biospin, Ettlingen, Germany).

The DQF sequence was used with the adiabatic inversion pulse as described in section 2.3, to further suppress the abundant lipid resonances of skeletal muscle which have an identical chemical shift as lactate (i.e. 1.3 ppm).

According to the reasoning in section 2.3.3, confirmed by measurements on meat specimen shown in section 6.4, the echo time parameters  $\tau_1 = 25$  ms and  $\tau_2 = 32$  ms were chosen for measuring lactate spectra with the double quantum filter sequence.

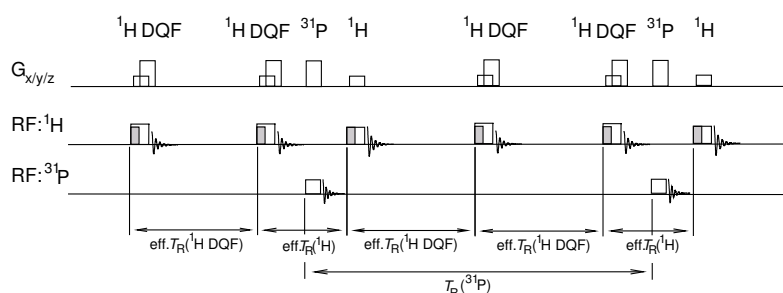


**Figure 7.1:** Schematic representation of the interleaved localised  $^1\text{H}$  DQF,  $^{31}\text{P}$  and  $^1\text{H}$  STEAM sequence. An arbitrary number of  $^1\text{H}$  DQF spectra (two in this example) can be acquired during each  $^{31}\text{P}$  /  $^1\text{H}$  STEAM acquisition  $T_R$  to optimise SNR of each nucleus’ spectra despite the large differences in  $T_1$ . Outlined rectangles schematically represent RF and  $B_0$  gradient pulses.



### 7.2.2. Subjects and Materials

Healthy subjects ( $n = 7$ ) executed ischaemic plantar-flexion on a pedal-ergometer [82]. Ischaemia was induced by a cuff placed on the thigh above the knee, which the subjects were instructed to inflate at a given time and were allowed to release air after a self-chosen ischaemic post-exercise period which lasted typically  $\sim 2$  min. The DQF VOI was chosen between  $3.9$  and  $5.4\text{cm}^3$ , the  $^1\text{H}$  STEAM voxel's volume was  $\sim 2.6\text{cm}^3$  and the  $^{31}\text{P}$  VOI was  $\sim 32\text{cm}^3$ , depending on the individual size of the gastrocnemius muscle, similar to the dual interleaved measurements (chapter 5). The  $^1\text{H}$  voxels were not chosen to be the same size as the  $^{31}\text{P}$  VOI to avoid broad  $^1\text{H}$  line widths and lipid contamination in the DQF spectra from subcutaneous fat, which would render spectra unusable. All VOIs were positioned in the same muscle, about concentrically (see Fig. 7.3) and avoiding subcutaneous fat, especially for the  $^1\text{H}$  voxels. A short echo time  $T_E = 7.5\text{ms}$  and  $T_M = 30\text{ms}$  was chosen for both STEAM experiments, receiver bandwidth was  $BW = 2500\text{Hz}$  and 1024 data points were acquired in all three interleaved experiments.

A phantom replacement technique employing test objects filled with lactate solutions (25 and 50 mmol/l) matching the coil load of an in vivo measurement and a small vial placed below the surface coil used as external reference to estimate the coil's sensitivity was used for absolute quantification. The knowledge about fibre orientation and the parameters of eq. 2.5 as given in [36], i.e. compartmentation ratios, and relaxation times (also of the test objects) together with back-calculation factors for varying voxel sizes, receiver gains and number of averages were taken into account when calculating lactate absolute concentrations. The voxel was positioned identically in calf muscles in vivo and in the phantom used as absolute concentration reference within an accuracy

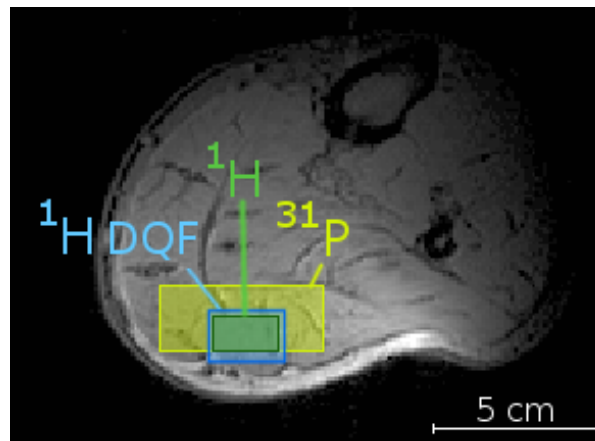


**Figure 7.3:** Typical position of the volumes of interest for interleaved localised DQF and multi-nuclear STEAM spectroscopy in human medial gastrocnemius muscle. Localised DQF for lactate detection: voxel size  $V = 4.0\text{cm}^3$ ,  $^1\text{H}$  STEAM:  $V = 2.6\text{cm}^3$ ,  $^{31}\text{P}$  STEAM:  $V = 31.3\text{cm}^3$ .

## 7. Triple Interleaved $^1\text{H}$ DQF/ $^{31}\text{P}$ / $^1\text{H}$ MRS

of  $\lesssim 1$  cm relative to the surface coil. For deviations from the the identical position in  $y$  (vertical, A-P) direction which were typically 6 mm, a further correction factor, interpolated from measurements on test objects with varying voxel position along  $y$  (see Tab 7.1) and constant RF amplitudes were applied.

**Table 7.1:** DQF lactate signal in a test object with varying voxel position along  $y$  (towards (+) and away from (-) the surface coil), relative to the standard measurement position at  $y = -6.3$  cm below the magnet's and gradient coils' iso-centre. The DQF signal was measured by peak integration.

shift along $y$ / cm	signal / %
-0.6	94
-0.3	97
0	100
+0.3	91
+0.6	81

For quantitative validation, lactate concentration in fresh porcine gastrocnemius was measured by standard biochemical methods several times immediately before and after MRS, and after further 4 and 48 hours of storage at  $4^\circ\text{C}$ . Muscle samples of  $\sim 50$  mg were weighed, filled into test tubes with 1 ml perchloric acid per sample and stored in a freezer ( $-80^\circ\text{C}$ ) for subsequent enzymatic assay, similar to the procedure described in [35].

Cytosolic concentrations of inorganic phosphate ( $\text{P}_i$ ) and phosphocreatine (PCr) were calculated from fully-relaxed  $^{31}\text{P}$  MRS measurements of PCr/ATP and  $\text{P}_i$ /ATP at rest (assuming ATP concentration of 8.2 mmol/l cell water), with exercise changes obtained by proportion, and cytosolic pH was obtained from the chemical shift of  $\text{P}_i$  [101]. Cytosolic lactate concentration was calculated from muscle lactate (mmol/l muscle) assuming muscle density of 1.04 kg/l and cytosolic water content of 0.66 l/kg [102]. Expected lactate concentration was calculated from pH,  $\text{P}_i$  and PCr changes by summing the protons consumed by net hydrolysis of PCr [14] and buffered by  $\text{P}_i$  and non- $\text{P}_i$  buffers [96], the latter assuming a non- $\text{P}_i$  buffer capacity of 20 slykes at rest, increasing 55 slykes/unit as pH falls, figures were derived indirectly from a  $^{31}\text{P}$  MRS analysis of ischaemic forearm exercise [96]. Results are given as mean  $\pm$  SEM.

### 7.3. Results

Lactate concentration measured with the double quantum filter sequence was 40 mmol/l muscle wet wt. (for an estimation of error, see discussion section) in porcine gastrocnemius, ex vivo, close to the biochemical measurement of  $39 \pm 5$  mmol/l (mean  $\pm$  SD).

Time resolved series of spectra acquired in human gastrocnemius muscle in vivo are shown in Fig. 7.4. Localised DQF lactate spectra,  $^{31}\text{P}$  STEAM and  $^1\text{H}$  STEAM spectra

## 7. Triple Interleaved $^1\text{H}$ DQF/ $^{31}\text{P}$ / $^1\text{H}$ MRS

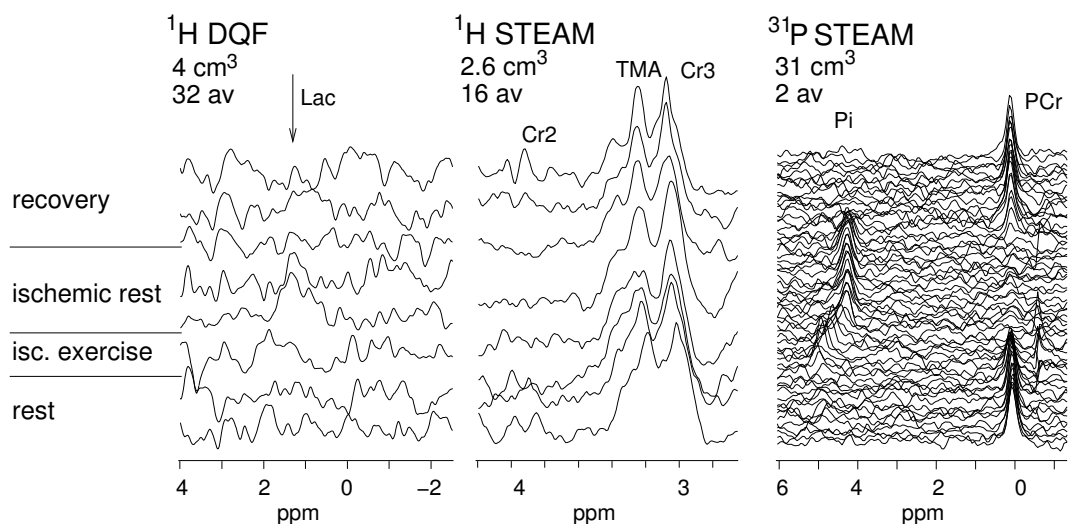


**Figure 7.4:** Localised DQF lactate spectra with short (57 ms) echo time (32 averages/spectrum),  $^1\text{H}$  STEAM (16 averages/spectrum) and  $^{31}\text{P}$  STEAM (2 averages/spectrum) all acquired in a single interleaved experiment on human gastrocnemius.

were acquired in a single interleaved experiment, during rest, ischaemic exercise (50 % MVC), a post-exercise ischaemic period and recovery.

DQF  $^1\text{H}$  spectra show a lactate resonance at 1.3 ppm after ischaemic exercise, which persists during post-exercise ischaemia and vanishes after release of the cuff. In  $^{31}\text{P}$  spectra, a PCr drop and increase of  $\text{P}_i$  is accompanied with the pH induced shift of the  $\text{P}_i$  peak towards the PCr resonance. In  $^1\text{H}$  spectra the  $\text{CH}_2$  resonance of creatine follows the PCr drop of PCr in  $^{31}\text{P}$  spectra while other metabolites remain unchanged, or show spurious variations according to motion in case of EMCL (lipids are not shown in Fig. 7.4.)

The absolute concentrations of lactate for all subjects are listed in Tab. 7.2. (DQF spectra of subject E were not quantifiable. Data related to this subject are given in the table but were excluded from the calculation of averages and standard deviations.) Here, the symbol BMI denotes the body mass index, VOI is the volume of interest. i.e. voxel size. The factor for taking into account the effect of varying coil load for an in vivo and a phantom measurement is denoted “ref” and is given in percent. The backcalculation factor “back-calc” relates the concentration of the phantom reference, the fitted peak amplitudes in phantom and in vivo measurements via the theoretically modelled DQF signal amplitude to the absolute concentration of lactate in vivo. A muscle fibre orientation of  $24^\circ$  was assumed in the numerical simulation of the DQF signal’s modulation. Note the large distribution of values for the back-calculation factor and the nonetheless small standard deviation for the calculated lactate concentrations.

In triple-interleaved MRS experiments, ischaemic exercise in healthy subjects re-

## 7. Triple Interleaved $^1\text{H}$ DQF/ $^{31}\text{P}$ / $^1\text{H}$ MRS

**Table 7.2:** Summarised results for lactate concentrations given in in mmol/l wet weight in exercising human gastrocnemius muscle. Results are given as mean  $\pm$  SD. For an explanation of symbols see text, page 64.

subject	age	$h$	$m$	BMI	VOI	ref	back-	[lactate]
	a	m	kg	kg/m <sup>2</sup>	ml	%	calc.	mmol/l w.wt.
A	26.6	1.78	65	20.5	3.9	94.3	530.9	10.6
B	37.1	1.82	88	26.6	4.0	n.m.	2216.8	21.2
C	25.5	1.75	73	23.8	4.4	91.0	1789.8	15.6
D	33.7	1.72	75	25.4	4.3	100.2	2786.7	16.5
(E)	(22.9)	(1.90)	(80)	(22.2)	(5.3)	(120.8)	–	–
F	27.2	1.73	77	25.7	5.0	110.5	2132.9	16.3
G	26.3	1.74	64	21.1	5.0	114.8	4321.3	16.5
				23.9 $\pm$ 2.5		102 $\pm$ 10		16.1 $\pm$ 3.4

sulted in a pH decrease of  $0.47 \pm 0.06$  below the resting value of  $7.06 \pm 0.03$ , and PCr decrease to  $24 \pm 2\%$  of resting calf muscle ( $n = 6$ ). This corresponds to an expected lactate concentration of  $24 \pm 2$  mmol/l cell water. In close agreement, the observed lactate concentration was  $24 \pm 2$  mmol/l, after converting the data in Tab. 7.2 from wet weight cellular water concentrations.

ATP before and after exercise was constant within 3.5%. After releasing the cuff, PCr recovered back to baseline with a halftime of  $66 \pm 9$  s.

### 7.4. Discussion

The method gives a remarkably good fit both to biochemically measured lactate concentration in porcine gastrocnemius and to the lactate concentration in human calf muscle expected on the basis of changes in pH, Pi and PCr. As the latter calculation uses cytosolic buffer capacity based on an indirect analysis of proton handling in ischaemically exercising forearm muscle, the agreement supports both the present method and the analysis of the forearm data [96].

**Estimation of propagated error:** For a single NMR measurement of lactate concentration, a rough estimation of total error can be given: The dominating factor

**Table 7.3:** Lactate concentration in a specimen of porcine gastrocnemius given in in mmol/l wet weight and data of phantom solution used as absolute concentration reference.

type	VOI	ref	back-	[lactate]
	ml	%	calc.	mmol/l wet wt.
porcine meat	4.0	95.6	11360	40.4
solution	4.3	100.0	474.7	25

## 7. Triple Interleaved $^1\text{H}$ DQF/ $^{31}\text{P}$ / $^1\text{H}$ MRS

is presumably the uncertainty in fibre orientation which may affect signal amplitude by up to 15%, but probably less, as discussed in section 6.4. The effect of the remaining factors contributing to the signal simulated analytically in eq. 2.5 (intra- and extracellular lactate pool fractions  $a, b$  and relaxation times  $T_{2s}, T_{2l}$  and  $T_1$ ) is approximately 5% each, or less. The propagated error of these multiplicative factors is 19%. This corresponds to an absolute concentration and error of  $40 \pm 7$  mmol/l for the lactate concentration of the porcine meat specimen, and  $16 \pm 3$  mmol/l wet wt. for a single measurement in human gastrocnemius. As these errors agree well with the standard deviation of averaged data, it may be concluded that the total error for single measurements represent the upper limits in the experimental setup.

Several studies have demonstrated the effect of increased pennation angle as response to resistance training and muscle hypertrophy [103, 104], while disuse muscle atrophy causes pennation angles to decrease [105]. Smaller pennation angles were observed in different leg muscles of sprinters compared to distance runners [106]. No direct relation was found between the architectural parameters and fibre composition [107, 108].

Our subjects were normal healthy volunteers, some doing physical exercise on a regular basis (distance running or cycling on several days per week).

**Consequences and Limitations:** Current data acquired in this work help to confirm assumptions about cellular proton buffering capacity which have, although widely accepted, become subject of dispute, recently [98, 97, 109].

Sensitivity and, hence, time resolution is a limiting factor. Although it has been possible to drastically increase sensitivity by the use of short  $T_E$ , (compared to the classically used 135 ms), the time resolution for which lactate quantification is approximately 96 s. Improving sensitivity by increasing voxel sizes is limited by the size of the muscle under investigation and lipid contamination increases beyond the capabilities of the suppression techniques applied, when subcutaneous fat or bone marrow is included in the VOI.

To address metabolic efflux, lactate, pH and PCr changes during recovery from ischaemic exercise need to be studied with better time resolution and to investigate control of glycogenolysis and coordination of oxidative versus glycolytic ATP production requires time-resolved studies in exercise, aerobic and ischaemic.

## **Part III.**

# **Conclusion and Perspective**

# 8

## Conclusion

In this work, NMR pulse sequences for time-resolved localised and double quantum filtered  $^1\text{H}$  and  $^{31}\text{P}$  spectroscopy in a single interleaved experiment have been developed and applied to human skeletal muscle while the subjects were exercising in the NMR scanner using a custom built non-magnetic exercise rig.

As a first step, a dual interleaved  $^1\text{H}$  and  $^{31}\text{P}$  stimulated echo acquisition mode (STEAM) sequence was implemented and used in measurements during dynamic aerobic calf muscle exercise. The benefits of the approach of interleaved multi-nuclear NMR spectroscopy experiments are reduced total measurement time and signal enhancement by the nuclear Overhauser effect of  $^{31}\text{P}$  spectra. Most significantly it opens the possibility of studying the dynamics of metabolism with multi nuclear MRS in a single run, e.g. examining PCr depletion and resynthesis with  $^{31}\text{P}$  MRS and the concomitant time course of the creatine  $\text{CH}_2$  resonance in  $^1\text{H}$  spectra.

After developing and testing a localised double quantum filter (DQF)  $^1\text{H}$  MRS pulse sequence for detection of the lactate  $\text{CH}_3$  resonance in the presence of strong overlaying lipid signals of human muscle, the method was extended to a triple interleaved experiment, comprising  $^1\text{H}$  DQF,  $^{31}\text{P}$  STEAM and  $^1\text{H}$  STEAM. The lactate  $\text{CH}_3$  doublet is subject to orientation dependent intensity modulations due to residual dipolar coupling in an anisotropic tissue, therefore, the echo time parameters of the DQF sequence hat to be tuned thoroughly to achieve near-optimum sensitivity while maintaining a robust signal with low intensity variation for an uncertain orientation of fibre angle relative to the magnetic field.

Time resolved spectra of human gastrocnemius were acquired using the triple interleaved  $^1\text{H}$  DQF,  $^{31}\text{P}$  and  $^1\text{H}$  STEAM pulse sequence during ischaemic calf muscle exercise. The acquired data help to confirm assumptions about cellular proton buffering capacity which have, although widely accepted, become subject to some controversy,

## 8. Conclusion

recently. Sensitivity and, hence, time resolution is a limiting factor, although it has been possible to drastically increase sensitivity by the use of short  $T_E$ , (compared to 135 ms, classically used in isotropic media, as e.g. brain). With improved time resolution, the developed method can be used to study metabolic efflux by quantifying lactate, pH and PCr changes during recovery from ischaemic exercise. Control of glycogenolysis and coordination of oxidative versus glycolytic ATP production can be investigated using this technique in time-resolved studies during aerobic and ischaemic muscle exercise.

# 9

## Perspective

So far, the methods developed in this work have been applied to muscle tissue at rest, under aerobic and ischaemic exercise and recovery with the aim of verifying and improving the quantitative understanding of muscle metabolism in normal healthy subjects. Interleaved acquisition of  $^1\text{H}$  and  $^{31}\text{P}$  STEAM spectra either with or without the localised double quantum filter, depending on the expected lactate production and accumulation under the given experimental conditions may also be used to study metabolic pathologies, e.g. diabetes or muscle dystrophies and may be applied to monitor the metabolism of professionally trained athletes. The latter may help to validate training schemes individually.

While the short-term effect of exercise on the PCr and  $\text{P}_i$  resonances in  $^{31}\text{P}$  muscle spectra is evident, as a PCr drop,  $\text{P}_i$  increase and a pH-induced shift of the  $\text{P}_i$  resonance frequency, and a lactate peak occurs in spectra acquired with dedicated  $^1\text{H}$  double quantum filtered (DQF) sequences after ischaemic exercise and during post-exercise ischaemia,  $^1\text{H}$  STEAM spectra show little variations within the time frame of several minutes, relevant for an interleaved MRS experiment. A drop and rise of the creatine  $\text{CH}_2$  signal at 4 ppm which follows the PCr time course, can be observed in healthy muscle tissue.

During strenuous exercise protocols, however – and also sporadically at lower exercise intensities in some subjects [94] – a resonance attributed to acetyl carnitine (AcCt) was described in  $^1\text{H}$  spectra of human muscle [94, 110]. Interleaved acquisition of  $^1\text{H}$  and  $^{31}\text{P}$  spectra can, in principle, be used to simultaneously acquire such time courses of AcCt and, additionally of high energy phosphates during high workload exercise protocols.

The combination of  $^1\text{H}$  and  $^{31}\text{P}$  STEAM and, eventually, interleaved DQF spectroscopy for lactate quantification may be combined with the acquisition of  $T_2$  pa-

## 9. Perspective

parameter NMR images in a follow-up project to the work described here, studying the effect of functional electrostimulation in denervated muscle. The recruitment of muscle can be mapped via  $T_2$  maps, and long term effects of electrostimulation of paraplegic patients can be monitored using proton and phosphorus NMR spectroscopy. The dual interleaved  $^1\text{H}/^{31}\text{P}$  STEAM protocol will be used to study the kinetics of absolute concentration of brain metabolites. For brain tissue, lactate editing by a DQF sequence is unnecessary, as here, no lipid signals are present which could overlap the lactate resonance (if present) at 1.3 ppm, and no orientation dependence is observed.

When the methodology of interleaving multi-nuclear NMR spectroscopy experiments is applied to protocols with intrinsically long acquisition times, such as spectroscopic imaging (CSI, chemical shift imaging) experiments with high spatial resolution, the gain in net measurement time of a factor of 2 for dual acquisition is particularly high. A single CSI measurement itself can easily take 30 – 45 min, while the overhead time for subject handling and for adjustments prior to the measurement (e.g. matching and tuning the coil, shimming and possibly also adjustment of transmitter and receiver gains, altogether typically 20 – 30 min) is equal for a single and for an interleaved experiment. It is therefore an interesting challenge to extend the method to  $^1\text{H}/^{31}\text{P}$  CSI for application to brain or muscle, considering that a  $^{31}\text{P}$  CSI data set comes “for free”, within the same measurement time as for a  $^1\text{H}$  CSI acquisition.

A spectroscopic imaging technique with higher temporal resolution than CSI, at the cost of sensitivity, spatial resolution and spectral width is echo-planar spectroscopic imaging (EPSI) [111, 112, 30]. This method may be implemented for application to human calf muscle [113] and an extension to a multi-nuclear version is conceivable in order to eventually combine metabolic and dynamic information and keeping sufficient spatial resolution and volume coverage.

In theory, a higher field strength increases the sensitivity of an NMR experiment by  $\text{SNR} \propto \omega_0^2 / (\omega_0^2 + \alpha \omega_0^{1/2})^{1/2}$  [114], with  $\omega_0 = \gamma B_0$ . This term approximates to a linear  $B_0$  dependence at high field strength, and to a factor of  $B_0^{7/4}$  for low fields. The actual gain depends on the nucleus chosen, lower sensitivity nuclei will gain more. When migrating an NMR spectroscopy experiment from 3 to 7 T, a theoretical gain by a factor of 2 in SNR may thus be expected, which could be transformed into a 4-fold time resolution, neglecting any  $B_0$  related increase of  $T_1$  and other influences. At higher field strength, the effect of susceptibility gradients is pronounced and the concomitant increase in line width needs to be compensated by the use of high order shim coils and automated localised non-linear shim procedures with the perspective that these more efficient and robust approaches will also help to improve measurement and processing techniques at 3 Tesla. This way, 3 T MRS applications may become more widely used in clinical research and diagnosis. Some technical aspects need to be considered for the perspective of interleaved multi-nuclear spectroscopy at higher fields. The method makes demands on the scanner’s hard- and software which are not commonly met by a system which has been designed with primarily MR imaging in clinical routine or neuroscience in mind, even if it is equipped with multiple RF amplifiers, at least one of them being a broadband amplifier for excitation of nuclei

## 9. Perspective

other than  $^1\text{H}$ . Some of these aspects appear trivial at first glance but can shape up as an insurmountable obstacle for interleaved NMR measurements, for example a dual tuned coil either needs to be equipped with two cables, one for each of the two RF channels (e.g. a  $^1\text{H}$  channel and a  $^{31}\text{P}$  channel), if two transmitters and/or receivers are available, or otherwise sufficiently rapid switching between the channels must be possible. Switching the receive and transmit channels needs to be executed under preservation of phase information of the currently inactive channel and switching back must be done phase coherently to ensure proper phase cycling and coherent accumulation of signal. When these prerequisites are met, the methods developed during this work can benefit from the higher sensitivity of NMR scanners with very high fields which become increasingly available to research facilities in the near future, and experiments studying time courses of lactate, PCr,  $\text{P}_i$  and pH with higher time resolution during recovery from ischaemia and during aerobic and ischaemic exercise will improve the quantitative understanding of human metabolism in vivo.

**Part IV.**  
**Appendices**

# Circuits, Diagrams and Detail Drawings

## A.1. Circuit Diagram of the Operation Amplifier IC for Force Sensors

Two force sensitive resistors (FSR, Model No. FSR-154-AS Conrad Electronic, Wels, Austria) each with an effective area of  $14.2\text{ cm}^2$  were attached to the pedal of the exercise rig. To compensate for the strongly non-linear characteristic curve  $R(F)$  of the FSR, an operation amplifier (LM348, Quad 741 Op Amp, National Semiconductor, Arlington, TX, USA) circuit was manufactured, as suggested in the FSR-154-AS's data sheet. The circuit diagram is in Fig. A.2 (a). The potentiometer for pedal angle measurement and FSRs are connected to the measuring card in a Linux-PC using coaxial cables via the magnet room's filter plate. For future reference, the BNC connections are also displayed, see Fig. A.2 (b).

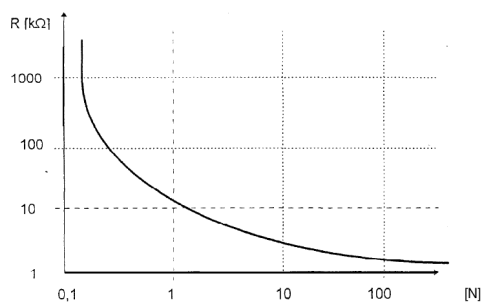
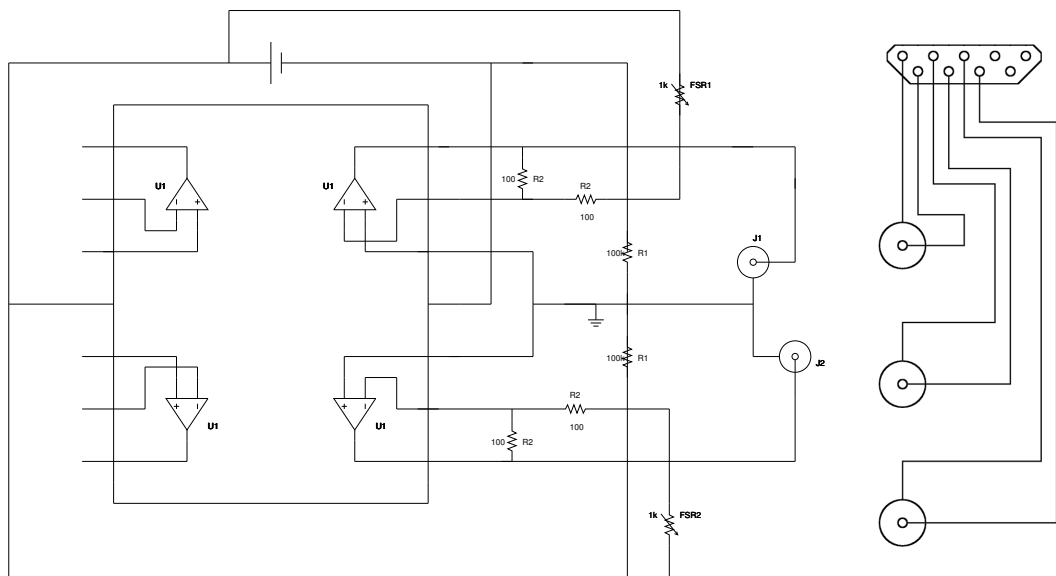


**Figure A.1:** Characteristic curve of a force sensitive resistor. (Specific to each FSR.)

A. Circuits, Diagrams and Detail Drawings



(a) Circuit Diagram of the Operation Amplifier IC for Force Sensors

(b) Connectors to the filter plate

**Figure A.2:** Circuit diagram of Op Amps for FSR (a), BNC Connectors at the filter plate (b).

## A.2. Block Diagram of the Dual Tuned Surface Coil

The coil used during all in vivo measurements is the standard “dual tuned surface coil  $\varnothing$  100 mm, 125/50 MHz”, commercially available from Bruker Biospin. The coil is actively decoupled (a feature which was not used). A block diagram of the coil circuitry is shown in Fig. A.3.

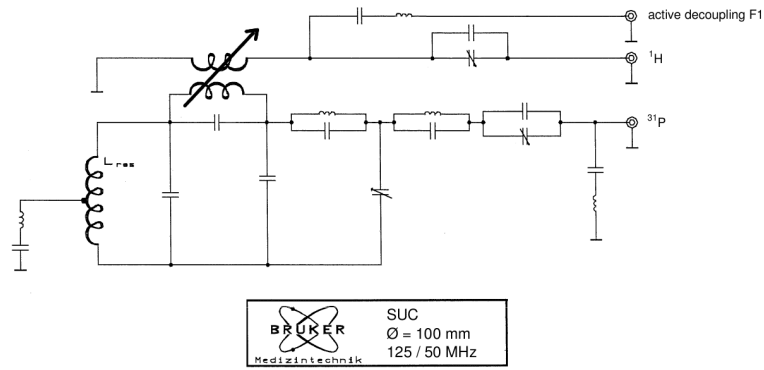


Figure A.3: Block diagram of the surface coil circuitry.



# Mathematical Appendix

## B.1. Product Operator Formalism

The concept of product operator formalism for the description of NMR experiments of weakly coupled spin systems can be looked up e.g. in the original reference [65] and is reproduced in textbooks on NMR [58, 57]. Here, only the most relevant formulae necessary for the understanding of the evolution of the  $IS_3$  (or  $AX_3$ ) spin system of lactate and the double quantum filter sequence are recapitulated in compact form.

### B.1.1. Nomenclature

$I_z$	...	Polarisation of spin I (longitudinal magnetisation)	
$I_x, I_y$	...	In phase x- and y- coherence of spin I (transverse magnetisation)	
$2I_xS_z, 2I_yS_z$	...	x- and y- coherence of I in anti-phase with respect to S	
$2I_xS_x, 2I_xS_y,$			
$2I_yS_x, 2I_yS_y$	...	Two-spin coherence of I and S	
$2I_zS_z$	...	longitudinal two-spin order of spins I and S.	(B.1)
			(B.2)

The cartesian product operators defined above, which always consist of a superposition of multiple quantum coherences can be rewritten to raising and lowering operators:

$$\begin{aligned} I^+ &= I_x + iI_y \\ I^- &= I_x - iI_y \\ I_0 &= I_z \end{aligned} \tag{B.3}$$

## B. Mathematical Appendix

which can be rearranged to linear combinations which reflect pure zero-, single- and double quantum coherences (ZQC, SQC, DQC).

$$\begin{aligned}
 I^+S^+, I^-S^- & \dots \text{ DQC} \\
 I^+S_0, I_0S^- & \dots \text{ SQC} \\
 I^+S^-, I^-S^+ & \dots \text{ ZQC}
 \end{aligned} \tag{B.4}$$

### B.1.2. Evolution of Product Operators

In this section, the evolution of product operators under the effect of RF pulses, chemical shift,  $B_0$  field gradients and spin-spin coupling is described.

All terms of the Hamiltonian

$$\mathcal{H} = \sum_k \Omega_k(I_{kz}) + \sum_l \sum_{k<l} \pi J_{kl}(2I_{kz}I_{lz}) \tag{B.5}$$

describing the evolution of the spin density operator under weak coupling commute, therefore the calculation can be computed in arbitrary order.

#### B.1.2.1. RF Pulses

The effect of a (strong non-selective) RF pulse with a flip angle  $\theta$  can be considered separately for each single-spin operator. For rotation about the  $x$ -axis the effect is

$$\begin{aligned}
 I_x & \xrightarrow{\theta I_x} I_x \\
 I_y & \xrightarrow{\theta I_x} I_y \cos + I_z \sin \\
 I_z & \xrightarrow{\theta I_x} I_z \cos - I_y \sin
 \end{aligned} \tag{B.6}$$

and about the  $y$ -axis

$$\begin{aligned}
 I_x & \xrightarrow{\theta I_y} I_x \cos - I_z \sin \\
 I_y & \xrightarrow{\theta I_y} I_y \\
 I_z & \xrightarrow{\theta I_y} I_z \cos + I_x \sin.
 \end{aligned} \tag{B.7}$$

#### B.1.2.2. Chemical Shift and $B_0$ Field Gradients

shift frequency  $\omega$

$$\begin{aligned}
 I_x & \xrightarrow{\omega\tau I_x} I_x \cos \omega\tau + I_y \sin \omega\tau \\
 I_y & \xrightarrow{\omega\tau I_x} I_y \cos \omega\tau - I_x \sin \omega\tau
 \end{aligned} \tag{B.8}$$

The modulation frequency  $\omega$  under the effect of chemical shifts and  $B_0$  field gradients is  $\omega = \omega_I + \omega_S$  for double quantum coherences, i.e. the sensitivity of DQCs to  $B_0$  gradients

## B. Mathematical Appendix

is twice the sensitivity of SQCs, while ZQCs are not influenced by  $B_0$  gradients. As a consequence,  $B_0$  gradients may be used to filter out coherence pathways by applying a gradient  $G_1$  during a time interval when the magnetisation of the spin system of interest has been brought to double quantum state and refocussing with a gradient  $|G_2| = 2 \cdot |G_1|$ .

### B.1.2.3. Spin-Spin Coupling

$$\begin{aligned} I_x &\xrightarrow{\pi J \tau 2 I_z S_z} I_x \cos(\pi J \tau) + 2 I_y S_z \sin(\pi J \tau) \\ I_y &\xrightarrow{\pi J \tau 2 I_z S_z} I_y \cos(\pi J \tau) - 2 I_x S_z \sin(\pi J \tau) \end{aligned} \quad (\text{B.9})$$

### B.1.3. Effect of a 90°-180°-90° Pulse Train on an $IS$ Spin System

$$I_z + S_z \quad (\text{B.10})$$

$$\xrightarrow{90_x} -I_y - S_y \quad (\text{B.11})$$

after effect of  $J$  evolution (eq. B.9) during  $\tau$

$$\begin{aligned} \xrightarrow{\tau} \sigma(\tau-) &= -I_y \cos(\pi J \tau) + 2 I_x S_z \sin(\pi J \tau) - S_y \cos(\pi J \tau) + 2 I_z S_x \sin(\pi J \tau) = \\ &= -(I_y + S_z) \cos(\pi J \tau) + (2 I_x S_z + 2 I_x S_z) \sin(\pi J \tau) \end{aligned} \quad (\text{B.12})$$

The chemical shift evolution during  $\tau$  has been refocused by the 180° pulse at  $t = \tau/2$ .

$$\xrightarrow{90_x} \sigma(\tau+) = -(I_z + S_z) \cos(\pi J \tau) - \underbrace{(2 I_x S_y + 2 I_y S_z)}_{\text{DQC}_y} \sin(\pi J \tau) \quad (\text{B.13})$$

Only magnetisation which is in double quantum state at this point in time can pass the filter consisting of  $|G_2| = 2 \cdot |G_1|$ , as detailed e.g. in [57].

## B.2. $J$ Evolution of an $IS_3$ System

The previous rules were valid for an  $IS$  (or  $AX$ ) system of spins  $I = 1/2$ . The evolution of an  $IS_3$  (or  $AX_3$ ) system during the pulse sequence 90°-180°-90° can be deduced straightly from eq. B.9. The magnetisation has evolved under the influence of  $J$  coupling, just before the second 90° pulse, to

$$I_y \xrightarrow{\pi J \tau 2 I_z S_{1z}} I_y \cos(\pi J \tau) - 2 I_x S_{1z} \sin(\pi J \tau) \quad (\text{B.14})$$

$$\begin{aligned} &\xrightarrow{\pi J \tau 2 I_z S_{2z}} (I_y \cos(\pi J \tau) - 2 I_x S_{2z} \sin(\pi J \tau)) \cos(\pi J \tau) - \\ &\quad - 2 (I_x \cos(\pi J \tau) + 2 I_y S_{2z} \sin(\pi J \tau)) S_{1z} \sin(\pi J \tau) = \\ &= I_y \cos^2(\pi J \tau) - 2 I_x (S_{1z} + S_{2z}) \cos(\pi J \tau) \sin(\pi J \tau) - 4 I_y S_{1z} S_{2z} \sin^2(\pi J \tau) \end{aligned} \quad (\text{B.15})$$

## B. Mathematical Appendix

$$\begin{aligned} \frac{\pi J \tau 2 I_z S_{3z}}{\rightarrow} & I_y \cos^3(\pi J \tau) - 2 I_x (S_{1z} + S_{2z} + S_{3z}) \cos^2(\pi J \tau) \sin(\pi J \tau) \\ & - 4 I_y (S_{1z} S_{2z} + S_{1z} S_{3z} + S_{2z} S_{3z}) \cos(\pi J \tau) \sin^2(\pi J \tau) \\ & + 8 I_x S_{1z} S_{2z} S_{3z} \sin^3(\pi J \tau) \end{aligned} \quad (\text{B.16})$$

# Bibliography

1. S Silbernagl and A Despopoulos, editors. *Taschenatlas der Physiologie*. Georg Thieme Verlag, Stuttgart, 6<sup>th</sup> edition, 2003.
2. W F Ganong. *Review of Medical Physiology*. McGraw-Hill, New York, 21<sup>st</sup> edition, 2003.
3. T B Price, G Kamen, B M Damon, C A Knight, B Applegate, J C Gore, K Eward, and J F Signorile. Comparison of MRI with EMG to study muscle activity associated with dynamic plantar flexion. *Magn Reson Imaging*, 21(8):853–61, 2003.
4. K Vandendorpe, G Walter, L Ploutz-Snyder, G Dudley, M A Elliott, and K De Meirleir. Relationship between muscle T2\* relaxation properties and metabolic state: a combined localized <sup>31</sup>P-spectroscopy and <sup>1</sup>H-imaging study. *Eur J Appl Physiol*, 82(1-2):76–82, 2000.
5. W Platzer. Bewegungsapparat. In W K Kahle, H Leonhardt, and W Platzer, editors, *Taschenatlas der Anatomie*, volume 1, pages 252f., 259, Stuttgart, 1991. Georg Thieme Verlag.
6. Z Trajanoski, G A Brunner, L Schaupp, M Ellmerer, P Wach, T R Pieber, P Kotanko, and F Skrabal. Open-flow microperfusion of subcutaneous adipose tissue for on-line continuous ex vivo measurement of glucose concentration. *Diabetes Care*, 20(7):1114–1121, 1997.
7. J J Ackerman, T H Grove, G G Wong, D G Gadian, and G K Radda. Mapping of metabolites in whole animals by <sup>31</sup>P NMR using surface coils. *Nature*, 283(5743):167–170, 1980.
8. B Barbiroli, R Funicello, S Iotti, P Montagna, A Ferlini, and P Zaniol. <sup>31</sup>P-NMR spectroscopy of skeletal muscle in Becker dystrophy and DMD/BMD carriers. Altered rate of phosphate transport. *J Neurol Sci*, 109(2):188–195, 1992.
9. G J Kemp. Studying metabolic regulation in human muscle. *Biochem Soc Trans*, 28(2):100–103, 2000. Review.
10. G J Kemp. Non-invasive methods for studying brain energy metabolism: what they show and what it means. *Dev Neurosci*, 22(5-6):418–428, 2000. Review.
11. R J Connett. Analysis of metabolic control: new insights using a scaled creatine model. *Am J Physiol*, 254:R949–R959, 1988.

## Bibliography

12. G J Kemp, D N Manners, J F Clark, M E Bastin, and G K Radda. Theoretical modelling of some spatial and temporal aspects of the mitochondrion/creatine kinase/myofibril system in muscle. *Mol Cell Biochem*, 184(1-2):249–89, 1998.
13. S J Harkema and R A Meyer. Effect of acidosis on control of respiration in skeletal muscle. *Am J Physiol*, 272(2 Pt 1):C491–500, 1997.
14. M J Kushmerick. Multiple equilibria of cations with metabolites in muscle bioenergetics. *Am J Physiol*, 272(5 Pt 1):C1739–C1747, 1997.
15. G J Kemp and G K Radda. Quantitative interpretation of bioenergetic data from  $^{31}\text{P}$  and  $^1\text{H}$  magnetic resonance spectroscopic studies of skeletal muscle: an analytical review. *Magn Reson Q*, 10(1):43–63, 1994.
16. K Vandeborne, G Walter, J S Leigh, and G Goelman. pH heterogeneity during exercise in localized spectra from single human muscles. *Am J Physiol*, 265(5 Pt 1):C1332–13329, 1993.
17. K E Conley, M L Blei, T L Richards, M J Kushmerick, and S A Jubrias. Activation of glycolysis in human muscle in vivo. *Am J Physiol*, 273(1 Pt 1):C306–C315, 1997.
18. G Walter, K Vandeborne, M Elliott, and J S Leigh. In vivo ATP synthesis rates in single human muscles during high intensity exercise. *J Physiol*, 519(15):901–910, 1999.
19. A C Hsu and M J Dawson. Muscle glycogenolysis is not activated by changes in cytosolic P-metabolites: a  $^{31}\text{P}$  and  $^1\text{H}$  MRS demonstration. *Magn Reson Med*, 49(4):626–631, 2003.
20. D W Russ, K Vandeborne, G A Walter, M Elliott, and S A Binder-Macleod. Effects of muscle activation on fatigue and metabolism in human skeletal muscle. *J Appl Physiol*, 92(5):1978–1986, 2002.
21. G J Kemp, L J Hands, G Ramaswami, D J Taylor, A Nicolaidis, A Amato, and G K Radda. Calf muscle mitochondrial and glycogenolytic ATP synthesis in patients with claudication due to peripheral vascular disease analysed using  $^{31}\text{P}$  magnetic resonance spectroscopy. *Clin Sci (Lond)*, 89(Lond):581–90, 1995.
22. G J Kemp, N Roberts, W E Bimson, A Bakran, and S P Frostick. Muscle oxygenation and ATP turnover when blood flow is impaired by vascular disease. *Mol Biol Rep*, 29(1-2):187–191, 2002.
23. R Kreis, M Kamber, M Koster, J Felblinger, J Slotboom, H Hoppeler, and C Boesch. Creatine supplementation—part II: in vivo magnetic resonance spectroscopy. *Med Sci Sports Exerc*, 31(12):1770–7, 1999.

## Bibliography

24. R Kreis, B Jung, J Slotboom, J Felblinger, and C Boesch. Effect of exercise on the creatine resonances in  $^1\text{H}$  MR spectra of human skeletal muscle. *J Magn Reson*, 137(2):350–357, 1999.
25. C Boesch, J Slotboom, H Hoppeler, and R Kreis. In vivo determination of intramyocellular lipids in human muscle by means of localized  $^1\text{H}$ -MR-spectroscopy. *Magn Reson Med*, 37(4):484–493, 1997.
26. C Boesch and R Kreis. Observation of intramyocellular lipids by  $^1\text{H}$ -magnetic resonance spectroscopy. *Ann N Y Acad Sci*, 904:25-31(Ann N Y Acad Sci. 2000 May;904:25-31):25–31, 2000. Review.
27. M Krššák, K F Petersen, R Bergeron, T Price, D Laurent, D L Rothman, M Roden, and G I Shulman. Intramuscular glycogen and intramyocellular lipid utilization during prolonged exercise and recovery in man: a  $^{13}\text{C}$  and  $^1\text{H}$  nuclear magnetic resonance spectroscopy study. *J Clin Endocrinol Metab*, 85(2):748–754, 2000.
28. K Brechtel, A M Niess, J Machann, K Rett, F Schick, C D Claussen, H H Dickhuth, H U Haering, and S Jacob. Utilisation of intramyocellular lipids (IM-CLs) during exercise as assessed by proton magnetic resonance spectroscopy ( $^1\text{H}$ -MRS). *Horm Metab Res*, 33(2):63–66, 2001.
29. P Vermathen, R Kreis, and C Boesch. Distribution of intramyocellular lipids in human calf muscles as determined by MR spectroscopic imaging. *Magn Reson Med*, 51(2):253–262, 2004.
30. J Weis, F Courivaud, M S Hansen, L Johansson, L R Ribe, and H Ahlstrom. Lipid content in the musculature of the lower leg: evaluation with high-resolution spectroscopic imaging. *Magn Reson Med*, 54(1):152–158, 2005.
31. A.C. Hsu and M.J. Dawson. Accuracy of  $^1\text{H}$  and  $^{31}\text{P}$  MRS analyses of lactate in skeletal muscle. *Magn Reson Med*, 44(3):418–26, 2000.
32. R Kreis and C Boesch. Liquid-crystal-like structures of human muscle demonstrated by in vivo observation of direct dipolar coupling in localized proton magnetic resonance spectroscopy. *J Magn Reson B*, 104(2):189–192, 1994.
33. C Boesch and R Kreis. Dipolar coupling and ordering effects observed in magnetic resonance spectra of skeletal muscle. *NMR Biomed*, 14(2):140–148, 2001.
34. L Schröder and P Bachert. Evidence for a dipolar-coupled AM system in carnosine in human calf muscle from in vivo  $^1\text{H}$  NMR spectroscopy. *J Magn Reson*, 164(2):256–269, 2003.
35. I Asllani, E Shankland, T Pratum, and M Kushmerick. Anisotropic orientation of lactate in skeletal muscle observed by dipolar coupling in  $^1\text{H}$  NMR spectroscopy. *J Magn Reson*, 139(2):213–224, 1999.

## Bibliography

36. I Asllani, E Shankland, T Pratum, and M Kushmerick. Double quantum filtered  $^1\text{H}$  NMR spectroscopy enables quantification of lactate in muscle. *J Magn Reson*, 152(2):195–202, 2001.
37. P A Bottomley, Y H Lee, and R G Weiss. Total creatine in muscle: imaging and quantification with proton MR spectroscopy. *Radiology*, 204:403–410, 1997.
38. H A Cheng, R A Robergs, J P Letellier, A Caprihan, M V Icenogle, and L J Haseler. Changes in muscle proton transverse relaxation times and acidosis during exercise and recovery. *J Appl Physiol*, 79(4):1370–1378, 1995.
39. C C Hanstock, R B Thompson, M E Trump, D Gheorghiu, P W Hochachka, and P S Allen. Residual dipolar coupling of the Cr/PCr methyl resonance in resting human medial gastrocnemius muscle. *Magn Reson Med*, 42(3):421–424, 1999.
40. L Jouvencal, P G Carlier, and G Bloch. Evidence for bi-exponential transverse relaxation of lactate in excised rat muscle. *Magn Reson Med*, 41(3):624–626, 1999.
41. R Kreis, B Jung, J Slotboom, J Felblinger, and C Boesch. Effect of exercise on the creatine resonances in  $^1\text{H}$  MR spectra of human skeletal muscle. *J Magn Reson*, 137(2):350–357, 1999.
42. B R Newcomer and M D Boska.  $T_1$  measurements of  $^{31}\text{P}$  metabolites in resting and exercising human gastrocnemius/soleus muscle at 1.5 Tesla. *Magn. Res. Med.*, 41(3):486–494, 1999.
43. V Ntziachristos, R Kreis, C Boesch, and B Quistorff. Dipolar resonance frequency shifts in  $^1\text{H}$  MR spectra of skeletal muscle: confirmation in rats at 4.7 T in vivo and observation of changes postmortem. *Magn Reson Med*, 38(1):33–39, 1997.
44. T B Price and J C Gore. Effect of muscle glycogen content on exercise-induced changes in muscle  $T_2$  times. *J Appl Physiol*, 84(4):1178–1184, 1998.
45. S M Eleff, M D Schnall, L Ligetti, M Osbakken, V H Subramanian, B Chance, and J S Leigh. Concurrent measurements of cerebral blood flow, sodium, lactate, and high-energy phosphate metabolism using  $^{19}\text{F}$ ,  $^{23}\text{Na}$ ,  $^1\text{H}$ , and  $^{31}\text{P}$  nuclear magnetic resonance spectroscopy. *Magn Reson Med*, 7(4):412–424, 1988.
46. M D Schnall, L Bolinger, P F Renshaw, J C Haselgrove, V H Subramanian, S M Eleff, C Barlow, J S Leigh, and B Chance. Multinuclear MR imaging: a technique for combined anatomic and physiologic studies. *Radiology*, 162(3):863–866, 1987.
47. R Gruetter, S A Weisdorf, V Rajanayagan, M Terpstra, H Merkle, C L Truwit, M Garwood, S L Nyberg, and K Ugurbil. Resolution improvements in in vivo  $^1\text{H}$  NMR spectra with increased magnetic field strength. *J Magn Reson*, 135(1):260–264, 1998.

## Bibliography

48. M D .Boska, J A Nelson, N Sripathi, I I Pipinos, A D Shepard, and K M Welch.  $^{31}\text{P}$  MRS studies of exercising human muscle at high temporal resolution. *Magn Reson Med*, 41(6):1145–1151, 1999.
49. O Gonen, S Gruber, B S Li, V Mlynárik, and E Moser. Multivoxel 3D proton spectroscopy in the brain at 1.5 versus 3.0 T: signal-to-noise ratio and resolution comparison. *AJNR Am J Neuroradiol*, 22(9):1727–1731, 2001.
50. L Gyulai, M Schnall, A C McLaughlin, J S Leigh, and B Chance. Simultaneous  $^{31}\text{P}$ - and  $^1\text{H}$ -nuclear magnetic resonance studies of hypoxia and ischemia in the cat brain. *J Cereb Blood Flow Metab*, 7(5):543–51, 1987.
51. F Mitsumori and N Takaya. Interleave measurements of multinuclear spectra from the same localized area at 4.7 Tesla wholebody MRI system. In *Proc Intl Soc Mag Reson Med (ISMRM), 11<sup>th</sup> Annual Meeting*, page 1138, Toronto, Canada, 10-26 July 2003.
52. F Mitsumori, N Takaya, and H Watanabe. A method for interleave measurements of  $^1\text{H}$ ,  $^1\text{H}\{-^{13}\text{C}\}$ , and  $^{31}\text{P}$  spectra from the same localized area at 4.7 T wholebody system. In *Proc Intl Soc Mag Reson Med (ISMRM), 12<sup>th</sup> Annual Meeting*, page 2461, Kyoto, Japan, 15-21 May 2004.
53. C Brillault-Salvat, E Giacomini, C Wary, J Peynsaert, L Jouvensal, G Bloch, and P G Carlier. An interleaved heteronuclear NMRI-NMRS approach to non-invasive investigation of exercising human skeletal muscle. *Cell Mol Biol (Noisy-le-grand)*, 43(5):751–762, 1997.
54. C Brillault-Salvat, E Giacomini, L Jouvensal, C Wary, G Bloch, and P G Carlier. Simultaneous determination of muscle perfusion and oxygenation by interleaved NMR plethysmography and deoxymyoglobin spectroscopy. *NMR Biomed*, 10(7):315–323, 1997.
55. L Jouvensal, P G Carlier, and G Bloch. Low visibility of lactate in excised rat muscle using double quantum proton spectroscopy. *Magn Reson Med*, 38(5):706–711, 1997.
56. M Vanderthommen, S Duteil, C Wary, J S Raynaud, A Leroy-Willig, J M Crielaard, and P G Carlier. A comparison of voluntary and electrically induced contractions by interleaved  $^1\text{H}$ - and  $^{31}\text{P}$ -NMRS in humans. *J Appl Physiol*, 94(3):1012–1024, 2003.
57. R A de Graaf. *In vivo NMR Spectroscopy*. Wiley & Sons Ltd, West Sussex, 1998.
58. R R Ernst, G Bodenhausen, and A Wokaun. *Principles of Nuclear Magnetic Resonance in One and Two Dimensions*. Oxford University Press, New York, 1987.

## Bibliography

59. G Badurek. *Lecture notes: Biological and Medical Applications of Nuclear Physics, Part II*. Atominstitut, Wien, 1998.
60. J Frahm, K D Merboldt, and W Hänicke. Localized proton NMR spectroscopy using stimulated echoes. *J. Magn. Res.*, 72:502–508, 1987.
61. J Granot. Selected volume excitation using stimulated echoes (VEST). Application to spacially localized spectroscopy and imaging. *J. Magn. Res.*, 70:488–492, 1986.
62. R Kimmich and D Hoepfel. Volume-selective multipulse spin-echo spectroscopy. *J. Magn. Res.*, 72:379–384, 1987.
63. E L Hahn. Spin echoes. *Phys. Rev.*, 80(4):580–594, 1950.
64. R A de Graaf and D L Rothman. In vivo detection and quantification. *Concepts in Magn Reson*, 13(1):32–76, 2001.
65. O W Sørensen, G W Eich, M H Levitt, G Bodenhausen, and R R Ernst. Product operator formalism for the description of NMR pulse experiments. *Prog NMR Spect*, pages 163–192, 1983.
66. R Freeman. A physical picture of multiple-quantum coherence. *Concepts in Magnetic Resonance*, 10(2):63–84, 1998.
67. L Jouvensal, P G Carlier, and G Bloch. Practical implementation of single-voxel double-quantum editing on a whole-body NMR spectrometer: localized monitoring of lactate in the human leg during and after exercise. *Magn Reson Med*, 36(3):487–490, 1996.
68. N Tjandra and A Bax. Direct measurement of distances and angles in biomolecules by NMR in a dilute liquid crystalline medium. *Science*, 278(5340):1111–1114, 1997.
69. P Vermathen, C Boesch, and R Kreis. Mapping fiber orientation in human muscle by proton MR spectroscopic imaging. *Magn Reson Med*, 49(3):424–432, 2003.
70. B Quistorff, S Nielsen, C Thomsen, K E Jensen, and O Hendriksen. A simple calf muscle ergometer for use in a standard whole-body MR scanner. *Magn. Res. Med.*, 13(3):444–449, 1990.
71. J M Gonzalez de Suso, G Bernus, J Alonso, A Alay, A Capdevila, J Gili, J A Prat, and C Arus. Development and characterization of an ergometer to study the bioenergetics of the human quadriceps muscle by  $^{31}\text{P}$  NMR spectroscopy inside a standard MR scanner. *Magn. Res. Med.*, 29(4):575–581, 1993.
72. S Gruber, V Mlynarik, and E Moser. High-resolution 3D proton spectroscopic imaging of the human brain at 3 T: SNR issues and application for anatomy-matched voxel sizes. *Magn Reson Med*, 49(2):299–306, 2003.

## Bibliography

73. M Meyerspeer, M Krššák, and E Moser. Relaxation Times of  $^{31}\text{P}$ -Metabolites in Human Calf Muscle at 3 Tesla. *Magn. Res. Med.*, 49(4):620–625, 2003.
74. L Vanhamme, A van den Boogaart, and S van Huffel. Improved method for accurate and efficient quantification of MRS data with use of prior knowledge. *J. Magn. Res.*, 129:35–43, 1997.
75. A Naressi, C Couturier, J M Devos, M Janssen, C Mangeat, R de Beer, and D Graveron-Demilly. Java-based graphical user interface for the MRUI quantitation package. *MAGMA*, 12(2-3):141–152, 2001.
76. D G Gadian, G K Radda, T R Brown, E M Chance, M J Dawson, and D R Wilkie. The activity of creatine kinase in frog skeletal muscle studied by saturation-transfer nuclear magnetic resonance. *Biochem J*, 194(1):215–228, 1981.
77. A Horská, J Horský, and R G Spencer. Measurement of spin-lattice relaxation times in systems undergoing chemical exchange. *J. Magn. Res.*, 110:82–89, 1994.
78. A Horská and R G Spencer. Measurement of spin-lattice relaxation times and kinetic rate constants in rat muscle using progressive partial saturation and steady-state saturation transfer. *Magn. Res. Med.*, 36(2):232–240, 1996.
79. R Ouwerkerk and P A Bottomley. On neglecting chemical exchange effects when correcting in vivo  $^{31}\text{P}$  MRS data for partial saturation. *J. Magn. Res.*, 148(2):425–435, 2001.
80. R S Richardson, E A Noyszewski, K F Kendrick, J S Leigh, and P D Wagner. Myoglobin  $\text{O}_2$  desaturation during exercise. Evidence of limited  $\text{O}_2$  transport. *J Clin Invest*, 96(4):1916–1926, 1995.
81. J Zhang, Y Murakami, Y Zhang, Y K Cho, Y Ye, G Gong, R J Bache, K Uğurbil, and A H L From. Oxygen delivery does not limit cardiac performance during high work states. *Am J Physiol Heart Circ Physiol*, 277(1):50–57, 1999.
82. M Meyerspeer, M Krššák, G J Kemp, M Roden, and E Moser. Dynamic interleaved  $^1\text{H}/^{31}\text{P}$  STEAM MRS at 3 Tesla using a pneumatic force-controlled plantar flexion exercise rig. *MAGMA*, 2005. in press.
83. R R Ernst and W A Anderson. Fourier transform NMR spectroscopy. *Rev. Sci. Instrum.*, 37:93, 1966.
84. R R Ernst, G Bodenhausen, and A Wokaun. *Principles of Nuclear Magnetic Resonance in One and Two Dimensions*, chapter 4, page 155. Oxford University Press, New York, 1987.
85. M. Krššák, V. Mlynárik, M. Meyerspeer, E. Moser, and M. Roden.  $^1\text{H}$  NMR relaxation times of skeletal muscle metabolites at 3 T. *MAGMA*, 16:155–159, 2004.

## Bibliography

86. A Haase, J Frahm, W Hanicke, and D Matthaei.  $^1\text{H}$  NMR chemical shift selective (CHESS) imaging. *Phys Med Biol*, 30(4):341–344, 1985.
87. R Gruetter. Automatic, localized in vivo adjustment of all first- and second-order shim coils. *Magn. Res. Med.*, 29:804–811, 1993.
88. M Meyerspeer. Localized  $^{31}\text{P}$ -NMR Spectroscopy in vivo at 3 Tesla. Diploma thesis, Technische Universität Wien, Atominstitut der Österreichischen Universitäten, Wien, 2001.
89. J Machann, G Steidle, G Helms, and F Schick. Orientation dependent effects in spectra of human skeletal muscle recorded at 1.5 and 3 T. In *Proc Intl Soc Mag Reson Med (ISMRM), 12<sup>th</sup> Annual Meeting*, page 789, Kyoto, Japan, 2004.
90. F Hug, D Bendahan, Y Le Fur, P J Cozzone, and L Grelot. Heterogeneity of muscle recruitment pattern during pedaling in professional road cyclists: a magnetic resonance imaging and electromyography study. *Eur J Appl Physiol*, 92(3):334–42, 2004.
91. T R Brown, R Stoyanova, T Greenberg, R Srinivasan, and J Murphy-Boesch. NOE enhancements and  $T_1$  relaxation times of phosphorylated metabolites in human calf muscle at 1.5 Tesla. *Magn. Res. Med.*, 33(3):417–421, 1995.
92. H Lei, X H Zhu, X L Zhang, K Ugurbil, and W Chen. In vivo  $^{31}\text{P}$  magnetic resonance spectroscopy of human brain at 7 T: an initial experience. *Magn Reson Med*, 49(2):199–205, 2003.
93. J Murphy-Boesch, R Stoyanova, R Srinivasan, T Willard, D Vigneron, S Nelson, J S Taylor, and T R Brown. Proton-decoupled  $^{31}\text{P}$  chemical shift imaging of the human brain in normal volunteers. *NMR Biomed*, 6(3):173–80, 1993.
94. R Kreis, B Jung, S Rotman, J Slotboom, and C Boesch. Non-invasive observation of acetyl-group buffering by  $^1\text{H}$ -MR spectroscopy in exercising human muscle. *NMR Biomed*, 12(7):471–476, 1999.
95. T Williams, C Kelley, R Lang, and D Kotz. Gnuplot – An Interactive Plotting Program. The Free Software Foundation, Boston, MA, USA. Version 4.0. Available from GNU depositories.
96. G J Kemp, M Roussel, D Bendahan, Y Le Fur, and P J Cozzone. Interrelations of ATP synthesis and proton handling in ischaemically exercising human forearm muscle studied by  $^{31}\text{P}$  magnetic resonance spectroscopy. *J Physiol*, 535(Pt 3):901–928, 2001.
97. G Kemp. Lactate accumulation, proton buffering, and pH change in ischemically exercising muscle. *Am J Physiol Regul Integr Comp Physiol*, 289(3):R895–901, 2005.

## Bibliography

98. R A Robergs, F Ghiasvand, and D Parker. Biochemistry of exercise-induced metabolic acidosis. *Am J Physiol Regul Integr Comp Physiol*, 287(3):R502–516, 2004.
99. G J Crowther, M F Carey, W F Kemper, and K E Conley. Control of glycolysis in contracting skeletal muscle. I. Turning it on. *Am J Physiol Endocrinol Metab*, 282(1):E67–73, 2002.
100. D Bendahan, G J Kemp, M Roussel, Y L Fur, and P J Cozzone. ATP synthesis and proton handling in muscle during short periods of exercise and subsequent recovery. *J Appl Physiol*, 94(6):2391–2397, 2003.
101. D L Arnold, P M Matthews, and G K Radda. Metabolic recovery after exercise and the assessment of mitochondrial function in vivo in human skeletal muscle by means of  $^{31}\text{P}$  NMR. *Magn Reson Med*, 1(3):307–315, 1984.
102. K Sahlin. Intracellular pH and energy metabolism in skeletal muscle of man. With special reference to exercise. *Acta Physiol Scand Suppl*, 455:1–56, 1978.
103. P Aagaard, J L Andersen, P Dyhre-Poulsen, A M Leffers, A Wagner, S P Magnusson, J Halkjaer-Kristensen, and E B Simonsen. A mechanism for increased contractile strength of human pennate muscle in response to strength training: changes in muscle architecture. *J Physiol*, 534(Pt. 2):613–623, 2001.
104. Y Kawakami, T Abe, and T Fukunaga. Muscle-fiber pennation angles are greater in hypertrophied than in normal muscles. *J Appl Physiol*, 74(6):2740–2744, 1993.
105. M Narici and P Cerretelli. Changes in human muscle architecture in disuse-atrophy evaluated by ultrasound imaging. *J Gravit Physiol*, 5(1):73–74, 1998.
106. T Abe, K Kumagai, and W F Brechue. Fascicle length of leg muscles is greater in sprinters than distance runners. *Med Sci Sports Exerc*, 32(6):1125–1129, 2000.
107. T J Burkholder, B Fingado, S Baron, and R L Lieber. Relationship between muscle fiber types and sizes and muscle architectural properties in the mouse hindlimb. *J Morphol*, 221(2):177–190, 1994.
108. P L Powell, R R Roy, P Kanim, M A Bello, and V R Edgerton. Predictability of skeletal muscle tension from architectural determinations in guinea pig hindlimbs. *J Appl Physiol*, 57(6):1715–1721, 1984.
109. R A Robergs, F Ghiasvand, and D Parker. Lingering construct of lactic acidosis. *Am J Physiol Regul Integr Comp Physiol*, 289(3):R904–910, 2005.
110. J Slotboom1, K M Rösler, C Kiefer, and A Nirkko. A novel method for clinical functional  $^1\text{H}$  muscle spectroscopy using muscle contraction induced by Tetanic Repetitive Electrical Nerve Stimulation . In *Electronic supplement to MAGMA*, volume 16 Suppl 1, page 18, Copenhagen, DK, 2004. 12<sup>th</sup> meeting of the ESM-RMB. #42.

## Bibliography

111. S Posse, G Tedeschi, R Risinger, R Ogg, and D le Bihan. High speed  $^1\text{H}$  spectroscopic imaging in human brain by echo planar spatial-spectral encoding. *Magn Reson Med*, 33(1):34–40, 1995.
112. A Ebel, A A Maudsley, M W Weiner, and N Schuff. Achieving sufficient spectral bandwidth for volumetric  $^1\text{H}$  echo-planar spectroscopic imaging at 4 Tesla. *Magn Reson Med*, 54(3):697–701, 2005.
113. T Wilhelm and P Bachert. In vivo  $^{31}\text{P}$  echo-planar spectroscopic imaging of human calf muscle. *J. Magn. Res.*, 149(1):126–130, 2001.
114. D I Hoult. Rotating frame zeugmatography. *J. Magn. Res.*, 33:183–197, 1979.
115. R R Ernst. NMR, MRI und MRS – Wie haben die revolutionren Entwicklungen begonnen? In *2. Workshop Experimentelle in vivo NMR*, AKH Wien, Austria, July 1999.

# Nomenclature

ADP	adenosine di-phosphate (p. 3)
ATP	adenosine tri-phosphate (p. 3)
BMI	body mass index. $BMI = m/h^2$ (p. 45)
CK	creatine kinase (p. 3)
Cr	creatine (p. 3)
CSI	chemical shift imaging (p. 78)
DQC	double quantum coherence (p. 14)
EPSI	echo-planar spectroscopic imaging (p. 78)
FID	free induction decay (p. 11)
FWHM	full width at half maximum (p. 46)
G6P	glucose-6-phosphate (p. 4)
MRI	magnetic resonance imaging (p. 4)
MR	magnetic resonance, “When I dictate ‘nuclear magnetic resonance’ to my secretary, she writes ‘unclear magnetic resonance’, quote by R.R. Ernst [115] (p. 4)
MRS	magnetic resonance spectroscopy (p. 4)
MSC	MultiScanControl-Tool or Multiple Scan Control Tool, software by Bruker Biospin (p. 42)
n. m.	not measured (in tables) (p. 57)
NMR	nuclear magnetic resonance (p. 4)
NTP	nucleoside tri-phosphates (p. 39)
PCr	phosphocreatine, also called creatine phosphate (CrP) in the literature (p. 3)
P <sub>i</sub>	inorganic phosphate (p. 5)
SNR	signal to noise ratio (p. 35)
SNR/ <i>t</i>	signal to noise ratio per unit time (p. 38)
SQC	single quantum coherence (p. 14)
STEAM	stimulated echo acquisition mode (p. 11)
T <sub>E</sub>	echo time (p. 35)
T <sub>IR</sub>	inversion recovery time (p. 15)
T <sub>M</sub>	middle period, between the second and third 90° pulse in the STEAM sequence (p. 12)
T <sub>R</sub>	repetition time (p. 35)
VOI	volume of interest (p. 11)
ZQC	zero quantum coherence (p. 14)

# List of Figures

1.1.	Muscles of the human lower leg . . . . .	4
1.2.	Muscle energy metabolism as viewed by $^{31}\text{P}$ and $^1\text{H}$ MRS . . . . .	6
2.1.	Echoes occurring during a sequence with three RF pulses . . . . .	10
2.2.	Schematic of the STEAM sequence . . . . .	11
2.3.	Diagram of the DQF sequence . . . . .	13
2.4.	Lactate signal in solution and in muscle . . . . .	15
2.5.	Simulation of the lactate signal 2D . . . . .	16
2.6.	Simulation of the lactate signal, 3D . . . . .	17
2.7.	Simulation of the lactate signal, varying orientation, fixed $\tau_{1,2}$ . . . . .	18
3.1.	The 3T Bruker Medspec S 300 DBX whole-body scanner . . . . .	22
3.2.	Geometry of the ergometer's pedal . . . . .	22
3.3.	Parts of the ergometer . . . . .	23
3.4.	Ergometer in the magnet . . . . .	24
3.5.	Ergometer, full view . . . . .	24
3.6.	Position of force sensors on the pedal, geometry for $\vec{F}/\vec{M}$ conversion . . . . .	25
3.7.	Calibration of the pedal's angle sensor . . . . .	26
3.8.	Calibration of the pedal's force sensors . . . . .	27
3.9.	Spectra of human m. gastrocnemius at rest and after plantar flexion . . . . .	28
3.10.	Creatine $\text{CH}_3$ signal and the sum of PCr and $\text{P}_i$ during rest, exercise and recovery . . . . .	29
4.1.	$^1\text{H}$ pulse-acquire spectrum of human forearm . . . . .	31
4.2.	$^1\text{H}$ STEAM spectra of human gastrocnemius muscle . . . . .	32
4.3.	$^{31}\text{P}$ STEAM spectrum of human calf muscle . . . . .	33
4.4.	Effect of $T_R$ on spectral appearance, in vivo, pulse-acquire scheme . . . . .	34
4.5.	Relative peak areas of $\text{P}_i$ and NTP, scaled to their values at $T_R = 8\text{ s}$ . . . . .	35
5.1.	MSC-Tool base window for dual interleaved STEAM . . . . .	37
5.2.	interleaved $^1\text{H}$ and $^{31}\text{P}$ STEAM sequence, schematically . . . . .	39
5.3.	Typical position of the VOIs for interleaved spectroscopy in human calf . . . . .	39
5.4.	Comparison of single and dual acquisition in vivo . . . . .	42
5.5.	$^1\text{H}$ and $^{31}\text{P}$ STEAM spectra from human gastrocnemius muscle acquired in interleaved mode during rest, exercise and recovery . . . . .	43
5.6.	Pedal angle and force recorded during interleaved $^1\text{H}/^{31}\text{P}$ MRS . . . . .	43
6.1.	DQF pulse sequence . . . . .	49

*List of Figures*

6.2.	DQF Lactate signal intensity and phase, as function of $\tau'$ . . . . .	51
6.3.	DQF signal as function of lactate concentration in solution . . . . .	52
6.4.	$T_2$ fit curve for lactate in solution ( $C = 50$ mmol/l) . . . . .	52
6.5.	PRESS and localised DQF spectrum of a test object . . . . .	53
6.6.	STEAM and DQF Spectra from lipid, lactate and phosphate solution .	54
6.7.	STEAM spectrum of porcine meat specimen . . . . .	55
6.8.	DQF spectra of porcine meat specimen . . . . .	56
6.9.	Photograph of meat specimen . . . . .	57
6.10.	DQF spectra of meat at two orientations, varying echo time . . . . .	58
7.1.	Interleaved $^1\text{H}$ DQF, $^{31}\text{P}$ and $^1\text{H}$ STEAM sequence, schematically . .	60
7.2.	Pulse sequence of the interleaved $^1\text{H}$ DQF, $^{31}\text{P}$ and $^1\text{H}$ STEAM sequence	61
7.3.	Typical position of the VOIs for interleaved spectroscopy in human calf	62
7.4.	Localised DQF lactate spectra $^1\text{H}$ STEAM and $^{31}\text{P}$ STEAM acquired in a single interleaved experiment on human gastrocnemius . . . . .	64
A.1.	Characteristic curve of a force sensitive resistor . . . . .	74
A.2.	Circuit diagram of FSR Op Amps, BNC Connectors at filter plate . .	75
A.3.	Block diagram of the surface coil circuitry . . . . .	76
A.4.	Engineering detail drawing of the pneumatic system and pedal. . . . .	77

## List of Tables

6.1. Relaxation times of lactate solutions . . . . .	51
7.1. DQF lactate signal in a test object with varying voxel position along $y$	63
7.2. Summarised results for lactate concentrations in exercising human gastrocnemius muscle . . . . .	65
7.3. Lactate concentration in a specimen of porcine gastrocnemius and data of phantom solution used as absolute concentration reference . . . . .	65

# Danksagung

Vielen Dank Herrn Prof. Moser für die – exzellente – laufende Betreuung am Hochfeld-Magnetresonanz-Zentrum und, von Seiten der TU, Herrn Prof. Badurek.

Wesentlichen Anteil an der Einreichung und Durchführung des dieser Dissertation zugrundeliegenden Projekts haben Prof. Graham Kemp, Vlado Mlynárik, Arno Nauerth von Bruker Biospin und das Team der Universitätsklinik für Innere Medizin III, Martin Krššák, Julia Szendrödi, Georg Pfeiler, Ing. Peter Nowotny und Prof. Michael Roden, sowie, von der Universitätsklinik für Physikalische Medizin und Rehabilitation, Carina Zoech und Richard Crevenna.

Die Arbeitsgruppe trägt durch ein gutes Klima nicht nur in den Cafépausen ganz wesentlich dazu bei wie's läuft. Danke an Alex, Andreas, Attiq, Christian, Elmar, Ingo, Marek, Markus, Michael, Michal, Pavol, Sherin, den „speaker of native languages“ Simon, Stefan, Stephan und Yu.

Schließlich, aber nicht zuletzt möchte ich mich für ihre Unterstützung ganz vielfältiger Art bei meinen Eltern bedanken.

# Curriculum Vitae

## Martin Meyerspeer

*Work address:*

MR High Field Centre of Excellence  
Center for Biomedical Engineering and Physics  
Vienna Medical University  
Lazarettgasse 14  
1090 Wien  
Austria

*Private address:*

Edelhofgasse 36 / 21  
1180 Wien  
Austria

*Phone:* +43-699-81 988 273

*Phone:* +43-1-40400 1795

*Fax:* +43-1-40400 7631

*E-mail:* martin.meyerspeer@meduniwien.ac.at

## Personal Data

*Date of birth:* December 1<sup>st</sup>, 1974

*Place:* Stuttgart (Germany)

*Nationality:* German

*Marital status:* unmarried, 1 child

## Education

July 2001      Diplomingenieur (Master of Science) in Physics, University of  
Technology, Vienna.  
Diploma Thesis: “Localized <sup>31</sup>P-NMR Spectroscopy *in vivo* at 3  
Tesla” (Quality control on phantoms, relaxation time measurement  
and absolute quantification of metabolites in human calf muscle)

Jan. – Aug. 99      Projects in NMR at the Institute for Medical Physics,  
University of Vienna (NMR relaxometry / high field imaging)

Dec. 1995      Intermediate diploma for Technical Physics

Oct. 1993      Enrolment at University of Technology, Vienna

June 1993      A-level (Bundesrealgymnasium Zell am See, Austria)

## Curriculum Vitae

### Experience

- April 2002      *MRI/MRS Advanced Customer Training Course*, Bruker Biospin, Ettlingen (D)
- Sep. 2001      Summer school, *One- and Multidimensional NMR Spectroscopy in liquid Phase*, Niederöblarn (A)
- June 2000      Summer school, *Physical Basis of Magnetic Resonance Imaging*, Aberdeen (UK)
- Oct. 1999      International EMBO Course, *In vivo Magnetic Resonance Imaging and Spectroscopy in Basic Research*, Basel (CH)
- Jul./Aug. 97 & 98      Internship at Siemens AG, power systems control

### Languages

- German    native
- English    fluent / near native
- French    basic knowledge

September 12<sup>th</sup> 2005

## Publications

### Full Papers

1. **M. Meyerspeer**, M. Krššák, G. J. Kemp, M. Roden and E. Moser. Dynamic interleaved  $^1\text{H}/^{31}\text{P}$  STEAM MRS at 3 Tesla using a pneumatic force-controlled plantar flexion exercise rig. *MAGMA* (2005). In press.
2. **M. Meyerspeer**, M. Krššák and E. Moser. Relaxation Times of  $^{31}\text{P}$ -Metabolites in Human Calf Muscle at 3 Tesla. *Magn. Res. Med.* 49, 620–625 (2003).
3. M. Krššák, V. Mlynárik, **M. Meyerspeer**, E. Moser and M. Roden.  $^1\text{H}$  NMR relaxation times of skeletal muscle metabolites at 3 T. *MAGMA* 16, 155–159 (2004).
4. M. Krebs, M. Krššák, E. Bernroider, C. Anderwald, A. Brehm, **M. Meyerspeer**, P. Nowotny, E. Roth, W. Waldhausl and M. Roden. Mechanism of amino acid-induced skeletal muscle insulin resistance in humans. *Diabetes* 51, 599–605 (2002).

### Abstracts

1. **M. Meyerspeer**, V. Mlynarik, M. Krssak, J. Szendroedi, M. Roden, G. J. Kemp and E. Moser. Short  $T_E$  localised DQF spectroscopy for lactate detection in exercising muscle interleaved with  $^1\text{H}$ - and  $^{31}\text{P}$  STEAM . In: *Electronic supplement to MAGMA*, vol. 17 Suppl 1. 13<sup>th</sup> meeting of the ESMRMB, Basel, CH (2005).
2. **M. Meyerspeer**, V. Mlynárik, M. Krššák, M. Roden, G. J. Kemp and E. Moser. Triple interleaved acquisition of  $^1\text{H}$  STEAM,  $^{31}\text{P}$  STEAM and localised DQF lactate edited spectra for MRS of skeletal muscle on a 3 T whole body system. In: *Electronic supplement to MAGMA*, vol. 16 Suppl 1, 18. 12<sup>th</sup> meeting of the ESMRMB, Copenhagen, DK (2004). #39.
3. **M. Meyerspeer**, M. Krššák, G. J. Kemp and E. Moser. Interleaved  $^1\text{H}/^{31}\text{P}$  STEAM Spectroscopy of Exercising Human Gastrocnemius Muscle at 3 Tesla. In: *Proc Intl Soc Mag Reson Med (ISMRM)*, 12<sup>th</sup> Annual Meeting, 2306. Kyoto, Japan (2004).
4. **M. Meyerspeer**, M. Krššák and E. Moser. Interleaved acquisition of  $^1\text{H}/^{31}\text{P}$  spectra from the human calf muscle with STEAM localisation at 3 Tesla. In: *Book of Abstracts*, vol. 16, 212. ESMRMB (2003).
5. M. Krššák, V. Mlynárik, **M. Meyerspeer**, E. Moser and M. Roden. Metabolite  $T_1$  and  $T_2$  relaxation times in human skeletal muscle at 3 Tesla. In: *Book of Abstracts*, vol. 16, 526. ESMRMB (2003).

6. M. Krššák, H. Hofer, **M. Meyerspeer**, E. Moser, A. Lohninger, P. Ferenci and M. Roden.  $^1\text{H}$  MRS assessment of hepatic steatosis in the patients with chronic hepatitis C. In: *Book of Abstracts*, vol. 16. ESMRMB (2003).
7. M. Krššák, H. Hofer, **M. Meyerspeer**, E. Moser, P. Ferenci and M. Roden. Measurement of hepatocellular lipid content and relaxation times of water and lipids in patients with chronic hepatitis C using  $^1\text{H}$  NMR Spectroscopy at 3 T. In: *Proc Intl Soc Mag Reson Med (ISMRM), 11<sup>th</sup> Annual Meeting*, 1480. Toronto, Canada (2003).
8. M. Krššák, H. Hofer, **M. Meyerspeer**, A. Lohninger, P. Ferenci and M. Roden. Validation of  $^1\text{H}$  MRS measurement of hepatic steatosis in the patients with chronic hepatitis C at 3 T. 89<sup>th</sup> Scientific Assembly & Annual Meeting of RSNA, Chicago, IL, USA (2003). Accepted for alternate presentation.
9. M. Krššák, M. Krebs, E. Bernroider, C. Anderwald, A. Brehm, **M. Meyerspeer**, P. Nowotny, E. Roth, W. Waldhäusl and M. Roden. Multinuclear  $^1\text{H}$ ,  $^{13}\text{C}$  and  $^{31}\text{P}$  NMRS study on mechanism of amino acid-induced skeletal muscle insulin resistance in humans. In: *Proc Intl Soc Mag Reson Med (ISMRM), 10<sup>th</sup> Annual Meeting*, vol. 10, 170 (2002).
10. M. Krebs, M. Krššák, E. Bernroider, C. Anderwald, A. Brehm, **M. Meyerspeer**, P. Nowotny, E. Roth, W. Waldhäusl and M. Roden. Mechanismus der aminosäuren-induzierten insulinresistenz im menschen. 29. Jahrestagung der ÖDG, Baden (2001).
11. **M. Meyerspeer**, M. Krššák, M. Roden and E. Moser.  $^{31}\text{P}$ -relaxation times in human calf muscle: influence of field strength. In: *Book of Abstracts*, 99. International Workshop on Non Investigation of Muscle Function, Marseille, France (2001).
12. **M. Meyerspeer**, M. Krššák, V. Mlynárik, S. Gruber and E. Moser.  $^{31}\text{P}$ -relaxation times of metabolites in human calf muscle at 3 T. In: *MAGMA*, vol. 11, suppl 1, 275. 17<sup>th</sup> Annual Meeting of ESMRMB, Paris, France (2000).